DEWETTING POLYMER BILAYERS BY SOLVENT VAPOUR ANNEALING: A PATHWAY TO MANUFACTURING BIOMIMETIC WATER HARVESTING SURFACE COATINGS

Omar Al-Khayat

School of Chemical and Biomolecular Engineering

and

School of Chemistry

The University of Sydney

2016

Declaration

This Thesis is presented at the School of Chemical and Biomolecular Engineering, University of Sydney, as part of the requirements for the degree of Doctor of Philosophy in Engineering. All of the experimental work reported within this Thesis has been carried out by the author in the Schools of Chemical and Biomolecular Engineering and Chemistry, University of Sydney, Sydney NSW, during August 2012 to March 2016. No part of this Thesis has been submitted for any other degree to this, or any other institution. When collaboration has been necessary, the collaborators have been named and the extent of the collaboration made clear. Results from other authors are referenced in the usual manner throughout the text.

_____   _____

Omar Al-Khayat   Date

Abstract

Producing patterned polymeric surfaces by a simple and controlled process has important implications for an increasing number of technological and bio-medical applications. The dewetting of thin polymer films is a robust and efficient route towards the fabrication of surfaces with topographical and chemical patterns from the nano- to the macro-scale. In this Thesis, a solvent vapour annealing technique is presented which provides control over the dynamics of the dewetting process, as well as the dewetted morphology.

Firstly, polystyrene (PS) films, which are only slightly metastable on a silicon substrate with a native oxide layer (SiO/Si), were annealed in the saturated vapour of a toluene-ethanol mixture, resulting in the fast dewetting of the PS film from the substrate. The dewetting rate was shown to depend on the ratio of the two solvents: the poor solvent ethanol acted to increase the dewetting driving force, while the good solvent, toluene, acted to plasticise the PS. The morphology of the rims surrounding the holes and the PS droplets were also affected by the concentration of ethanol in the solvent mixture.

Utilising the principle of good-poor solvent mixture annealing to promote the dewetting of polymer films, a bilayer of poly (4-vinylpyridine) (P4VP) / PS films was dewetted to produce a topographically and chemically patterned polymeric surface coating. Ethanol, a good solvent for P4VP, and acetone and water, poor solvents for P4VP, were combined in binary mixtures and the individual effect of each solvent on dewetting rate, rim and droplet morphology was investigated.

Finally, an application for the surface coatings patterned by dewetting of bilayers of polymer films was investigated, for atmospheric water harvesting. Using the solvent vapour annealing technique, nano- to macro-scale P4VP droplets on PS coated copper substrates were prepared and their water harvesting capability was analysed in a custom-built condensation chamber. The effect of pattern size and density was compared with the condensation performance of an unpatterned hydrophobic coating, under different relative humidity and sub-cooling temperature conditions.

Acknowledgments

<div dir="rtl">بسم الله الرحمن الرحيم</div>

The submission of this Thesis marks the conclusion of a long chapter in my life as a university student. While the road has been difficult but fulfilling, sometimes enjoyable and sometimes maddening, it has never been lonely. For that, I am grateful to all the people who have joined me on this journey, even if fleetingly, as the memories of this adventure will remain long after I forget what it was that I studied for three years in a chemistry lab in Sydney.

This is where I get the opportunity to thank you all:

~ Mum, Dad and, Mo ~

Thank you for all of your love and support. To you I dedicate this PhD for all the doors that you have opened for me in life and hope that I can always make you proud.

~ A/Prof Chiara Neto ~

The road to a PhD would not have been as smooth as it has been if it wasn't for your guidance and mentorship, nor would it have been as pleasant without your friendship, I'd like to thank you for all of the opportunities that you have provided.

~ Friends and Colleagues ~

I have had the pleasure of working alongside some of the brightest minds belonging to the kindest and most generous people that I have ever met, during my time with the KCPC and SusTech groups. I am grateful to all of you.

Thank you to Andrew McVicar, a friend and mentor who has always made himself free to help.

Away from "work" – I want to thank all of my old friends from home, and new friends from Sydney and beyond, and to all of the house mates who have been like family to me.

Publications arising from this work

1. Al-Khayat, Omar, et al. "Chain Collapse and Interfacial Slip of Polystyrene Films in Good/Nonsolvent Vapor Mixtures." *Macromolecules* (2016).

2. Rowe, Molly, et al. "High Glass Transition Temperature Fluoropolymers for Hydrophobic Surface Coatings via RAFT Copolymerization." *Australian Journal of Chemistry* (2016).

3. Al-Khayat, Omar, et al. "The Good, the Bad and the Slippery: A Tale of Three Solvents in Polymer Film Dewetting" [submitted] (2016)

Presentations arising from this work

1. **2015**: "Harvesting Water from Air: Micro-Patterned Polymer Surfaces for Water Capture and Heat Transfer" (oral), <u>Omar Al-Khayat</u>, Andrew Harris, Chiara Neto. *Australian Colloids and Interfaces Symposium*, Hobart TAS (Australia)

2. **2015**: "Dewetting of Stable Polymer Thin Films" (poster), <u>Omar Al-Khayat</u>, Keyun Shou, Kieran Geraghty, Andrew Minett, Andrew Harris, Chiara Neto. *Australian Colloids and Interfaces Symposium*, Hobart TAS (Australia)

3. **2015**: "Dewetting polymer films: A path to biomimetic water harvesting surface coatings" (oral), <u>Omar Al-Khayat</u>, Kieran Geraghty, Keyun Shou, Andrew Minett, Andrew Harris, Chiara Neto. *Sydney Surfaces and Soft Stuff Meeting,* Sydney NSW (Australia)

4. **2016**: "Polymer Film Dewetting: Our Route Towards Water Harvesting Surface Coatings." (oral) <u>Omar Al-Khayat</u>, Kieran Geraghty, Keyun Shou, David Beck, Chiara Neto. *Australian Colloids and Interfaces Student Symposium,* Kioloa NSW (Australia)

Table of Contents

CHAPTER 1

Introduction

1.1   Preamble

The fundamental understanding of the chemical interactions of molecular and macromolecular species at a solid interface is important for tailor making surfaces with desirable functionality. Chemically and physically patterning a surface to alter the interactions between the surface and the surrounding fluid environment on the nano and micro-scales has been achieved by a large variety of methods that include combinations of lithography and stamping,[1-2] polymer dewetting,[3-5] and multiscale texturing.[6-8] Such patterned surfaces have been proposed for numerous applications[9] in the areas of micro-fluidics,[10-13] microbiology and biomedicines[4, 14-22] as well as water harvesting.[3, 13, 21] A simple and cost effective fabricating technique is required for applications that require simultaneous control over the surface chemistry and physical topography over large surface areas.

Polymer coatings provide a simple route towards modifying the surface properties of a material while leaving the bulk properties of the material unchanged and have found use in a diverse array of fields, including microelectronics,[23-24] optics[25-26] and biomedicines.[27-28] It is possible to modify a surface at the nano, micro and the macro scales to produce unique physical characteristics and chemical functionality by utilising the dewetting phenomenon of polymer melts, which is the spontaneous withdrawal of the liquid polymer film from an underlying surface. This behaviour has been studied for decades with research on the contributions of slip behaviour at the liquid-solid interface,[12, 29-36] elastic macromolecular forces in the cast films,[36-46] and the presence of interfacial stabilising and destabilising forces,[47-52] to the dewetting of the polymer films. Controlled dewetting of polymer coatings can provide a route to cost effective, continuous and large-scale production of functionalised materials.

The process of dewetting a liquid polymer film is complex and dependent on many interrelated variables. For example, increasing the molecular weight of polymer chains in a film increases the number of entanglements,[53] raising both the viscosity of the bulk film and the friction force of the flowing film along the substrate.[29-30, 35] The wettability of the substrate by the polymer affects whether dewetting will occur rapidly and can be modified by changes in the surrounding fluid composition,[48-49, 54-57] the substrate chemistry[47, 58] or the choice of polymer. Finally,

the casting method and ageing history of the polymer films determine whether the polymer chains within the film are in equilibrium conformations,[39] as non-equilibrium chain conformations manifests as internal stresses which affect the dewetting rate and hole nucleation density. In order to control the dewetting process and produce replicable chemically and topographically patterned polymer coatings, it is important to understand and be able to predict the dewetting behaviour of a polymer film.

One of the applications of micro patterned surfaces is the harvesting of water from humid ambient environments.[2-3, 59-61] This particular application has been of interest since the observation of the unique behavioural and structural adaptation of the Namib Desert *Physosterna cribripes* beetle (Figure 1.1).[62-63] The bumps on the wing casing of the beetle were observed to be hydrophilic, in contrast to the remainder of the casing which was hydrophobic. This adaptation allows the beetle to nucleate and capture water droplets on a foggy morning on the bumps and drink the water droplets that roll down the hydrophobic troughs and channels towards its mouth. The water collection efficiency of surfaces patterned in this manner has been shown to be high compared to alternative materials.[3, 64]

Figure 1.1: Illustration of a Namib Desert beetle harvesting water from fog. Adapted from Asknature.org.[65]

Utilising the controlled dewetting of polymer coatings, it is possible to create structured materials with hydrophilic/hydrophobic contrast to have a high affinity for water harvesting. The successful implementation of these patterned surfaces opens up a diverse range of applications from surface coatings that increase the efficiency

condensation heat transfer to specialised materials for the passive and selective retrieval of condensable solvent vapours.

1.2   Wetting and Dewetting of Surfaces

The behaviour of a liquid drop on a solid substrate, as described by the surface energy of the substrate and the surface tension of the liquid in the presence of air or a vacuum has been extensively studied.[66-73] The liquid may spread, or wet, a substrate when the interactive forces between the substrate and the liquid are strong. The liquid will retract or dewet from the surface, as in the beading of water droplets on a dirty window or on a Teflon pan, when the forces are weak. Similarly, the wetting properties determine the energy barrier to adsorption of vapour molecules and the onset of heterogeneous condensation.

1.2.1   Thermodynamics at the substrate-liquid interface

The surface tension of a liquid arises due to the influence of the surrounding molecules on the energetic state of the liquid molecules at the interface. This results in a difference between the energy states of the molecules within the bulk from those at the surface, so liquids tend to minimise the number of molecules at the interface to decrease surface energy. Therefore, the surface free energy may be defined as the work required in bringing molecules from within the bulk to the interface in order to create a new surface having a unit area. The same definition can be used for the free surface energy of solids; however, unlike liquids, the surface tension of a solid may not be in equilibrium with the surface free energy. This is due to the low mobility of the molecules restricting molecular rearrangement and thus the surface tension of a solid is defined as the work spent in stretching the solid surface in a two dimensional plane.[74] de Gennes defines high free surface energy solids as those that are composed of strong chemical bonds, such as ionic, metallic or covalent, whereas low surface energy solids are based on relatively weak van der Waals chemical bonds, as is the case with polymers.[75]

It is possible to determine the shape a liquid will attain on a solid substrate by an energy balance at the solid-liquid-vapour contact line. This relationship is

described by Young's equation (Equation 1.1), whereby a balance between the solid-vapour, γ^{SV}, the solid-liquid, γ^{SL}, and the liquid-vapour, γ^{LV}, surface energies leads to an equilibrium contact angle, θ_e, of the liquid droplet on the substrate (Figure 1.2):

$$\gamma^{SV} = \gamma^{SL} + \gamma^{LV} \cos\theta_e \qquad (1.1)$$

From Young's relationship a spreading coefficient can be deduced (Equation 1.2); where a droplet will completely wet a surface if the coefficient is zero, otherwise only partial wetting is possible (Figure 1.2).

$$S = \gamma^{LV}(\cos\theta_e - 1) \qquad (1.2)$$

For the specific case of a water droplet on a substrate, when the droplet contact angle θ_e is less than 90°, the surface is considered *hydrophilic*, or "water loving", and when greater than this value, *hydrophobic*, which translates to "water fearing".
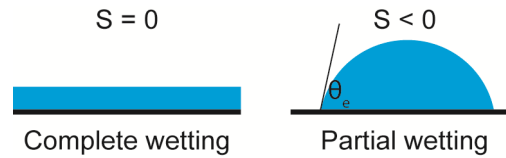
Figure 1.2: Illustration of the wetting regimes of a liquid on a substrate. In complete wetting, the liquid has a contact angle $\theta_e = 0$ and spreads on the substrate. For a partially wetting substrate, the liquid obtains a finite equilibrium contact angle.

Young's equation assumes ideally smooth and uniform surfaces, where the equilibrium at the three phase contact line is readily achieved. In reality, surfaces are rough and present defects that delay or prevent the three phase contact line from reaching equilibrium. On a tilted surface this causes droplets that are large enough to be affected by gravity to obtain a contact angle at the front that is greater than the equilibrium angle and a contact angle at the rear that is smaller than equilibrium. This behaviour is due to the energy requirements to wet the substrate in front of the droplet and dewet from the substrate at the rear in order for the droplet to slide.
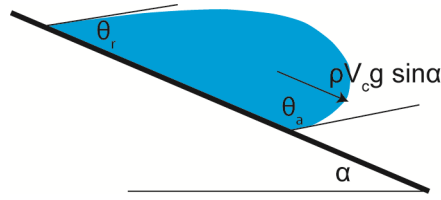
Figure 1.3: Illustration of a droplet on an inclined plane at a critical volume to begin sliding due to the effect of gravity.

The difference between these two contact angles is termed the contact angle hysteresis and can be considered as a measure of the reluctance of a droplet to slide down a surface (Figure 1.3). Furmidge deduced a relationship between the advancing, θ_a, and receding, θ_r, contact angles, and the surface tension of a droplet with the tilt angle α of the substrate and the critical mass and width of the droplet at the onset of sliding:[71]

$$\frac{mg\sin\alpha}{w} = \gamma^{LV}(\cos\theta_r - \cos\theta_a) \tag{1.3}$$

1.2.2   Heterogeneous condensation

The heterogeneous condensation behaviour of vapour molecules is widely observed both in nature and in a variety of technologies. Dew formation, observed naturally on a cool morning, is an interesting case study of this behaviour and of direct relevance to the subject of this Thesis. Beysens, in 1995, produced a study on the formation on dew on a substrate.[67] He highlighted the effect of the wetting properties of the surface on the nucleation of the liquid phase and the effect of dimensional constraints on the growth of a liquid droplet.

For a liquid droplet to nucleate from the vapour phase, the temperature at the substrate surface must be lower than that of the surrounding environment. There is a gain in volume energy, ΔE, associated with the phase change as well as an energy barrier associated with the formation of a liquid-vapour interface, the interfacial tension γ. The total energy of a liquid droplet is the sum of the volume energy and the interfacial energy. When this energy equation is minimised, a critical droplet radius, R_c, emerges as the minimum radius of a stable liquid droplet to nucleate on a substrate with droplet energy:[67]

$$F(R_c) = \frac{16\pi}{3}\frac{\gamma^3}{\Delta E^2} \tag{1.4}$$

Heterogeneous nucleation of a liquid phase on a solid is a function of the wettability of the surface to water, which is characterised by the contact angle of a water droplet on this surface. The surface wettability affects the magnitude of the energy barrier to the nucleation of stable liquid droplets and modifies the relationship between the droplet nucleation rate, dn/dt, and the droplet energy, $F(R_c)$ by:[76]

$$\frac{dn}{dt} \sim \exp\left[F(R_c)\left(2\frac{3-\cos\theta+\cos^3\theta}{3\sin^3\theta}\right)\right] \tag{1.5}$$

Once established, a nucleated liquid droplet grows by the diffusion of water molecules across a concentration gradient in the boundary layer surrounding the substrate. The release of the heat of condensation from the droplet to the substrate limits the growth rate and size of the water droplet, and multiple theories for the mechanism of droplet growth have been proposed.[77-79]

Droplet growth has been observed to occur in three stages, characterised by the surface coverage, s, which is a ratio of the wetted surface area to the total substrate area and the size of a growing droplet may be modelled as a function of time by the power law relationship, $\langle R\rangle \sim t^{\mu_s}$. When $s < 0.3$, very few coalescence events between adjacent droplets are observed to occur, and the growth exponent $\mu_s = 1/3$. For, $0.3 < s < 0.55$, rapid droplet growth is observed due to coalescence between neighbouring droplets. During this regime the growth law exponent is related to the dimensionality of the droplet and of the substrate, D_d and D_s respectively, by Equation 1.6. For the usual situation where a substrate is a two dimensional surface and the droplet three dimensional, $\mu_a = 1$. Where $\mu_s = 1/D_d$ for ideal thermal conditions.

$$\mu_a = \mu_s \frac{D_d}{D_d - D_s} \tag{1.6}$$

Finally for, $s > 0.55$, a stabilisation of the value of the surface coverage occurs due to competition between coalescence, (i) increasing droplet size as well as (ii) increasing the area of free substrate. The scaling law becomes useful when analysing

the condensation behaviour on fibres or on chemically heterogeneous surfaces where water droplets may preferentially nucleate and grow in only one dimension.

1.3   Dewetting Polymer Films

Polymer melts which are able to flow have been observed to spontaneously rearrange their geometry to minimise the total energy of the vapour-polymer-substrate system. This interesting behaviour has been extensively studied[36, 47, 52, 80] and many applications have been proposed for materials created by this simple and inexpensive process.[81] Some elements of the dewetting process, including the interfacial stability of films,[47, 48, 49, 50, 51] interfacial slip behaviour[12, 29, 30, 31, 32, 33, 34, 35, 36] and more recently, the role of elastic forces[36-46] have been a significant focus of research. However, interesting questions remain unanswered and there remains speculation as to the nature of the relationship between these mechanisms, their origins and their relative impact on the dewetting process. The techniques to achieve polymer film dewetting have developed from heating polymer films into a melt state and observing them dewet from solid substrates with different interfacial compositions,[34, 52] to changing the fluid environment surrounding a cast film,[55, 57] as well as dewetting multilayer systems[3, 82-83] and other approaches to stimulate film dewetting.[84-85]

One of the main causes of dewetting is the unfavorable interactions of the liquid film at the solid interface. For example, one proposed form of the interfacial potential $\psi(h)$ (Equation 1.7) includes the effects of short-range forces (first term) and long-range van der Waals forces (two following terms) for polystyrene films of thickness h on top of silicon substrates coated with silicon oxide of thickness d, with Hamaker constants A_{Si} (negative) and A_{SiO} (positive). In the case of a thick oxide layer (thickness d of 200 nm), this expression correctly predicts a van der Waals attraction that promotes film dewetting.[47]

$$\varphi(h) = \frac{c}{h^8} - \frac{A_{SiO}}{12\pi h^2} + \frac{A_{SiO} - A_{Si}}{12\pi(h+d)^2} \qquad (1.7)$$

The macroscopic behavior of a thin liquid film can be predicted by the effective interfacial potential. From this relation a film can be described as stable, metastable or unstable as a function of initial film thickness (Figure 1.4). The effective interface potential of unstable and metastable films obtains a global minimum at $h = h_{eq}$, where films thicker than h_{eq} spontaneously dewet from the substrate in order to reach the equilibrium film thickness, typically in the Angstrom range.[47] For metastable films a potential energy barrier must be overcome, for dewetting to occur.
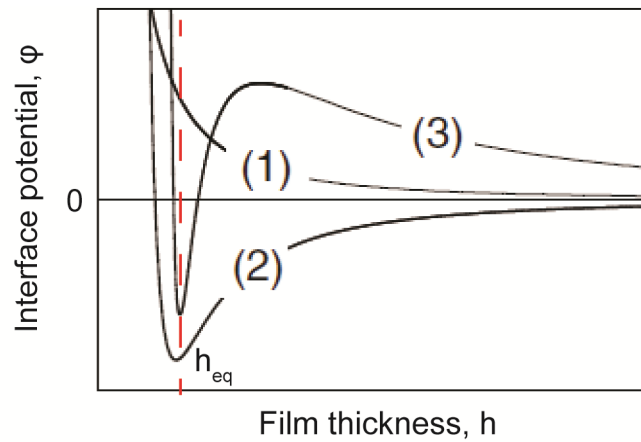
Figure 1.4: Illustration of the effective interface potential ψ, as a function of film thickness h, for (1) stable, (2) unstable and (3) metastable films. The equilibrium film thickness, h_{eq} on the substrate is found at the global minimum of the interfacial potential. Modified from Seemann *et al.*[47]

When polar interactions are important, i.e. when either the film or the fluid environment in which it is immersed are polar, polar attractions also contribute to increasing the driving force for film dewetting. The polar contribution often takes the form $S_p \, exp\left(-\frac{h}{l}\right)$, where S_p is the polar component of spreading coefficient, and l is a correlation length.[48-49, 54]

1.3.1   Evolution of dewetting

Liquid polymer films may either spinodally or heterogeneously dewet from a substrate as shown in Figure 1.5. Spinodal dewetting was first predicted by Vrij in 1966 and occurs in unstable films, where the film instability drives the formation of capillary waves with an amplitude that grows exponentially with time, $e^{t/\tau}$, with τ as

the characteristic growth time.[86] The film breaks down into spatially correlated micro and nano structures with a characteristic wavelength λ_s. The growth time τ varies as a fifth power of the film thickness and therefore spinodal dewetting can only be observed for ultrathin films, typically below 10 nm. The growth time of the instabilities is too long for thicker films and heterogeneous nucleation becomes the dominant mechanism.[80, 87]
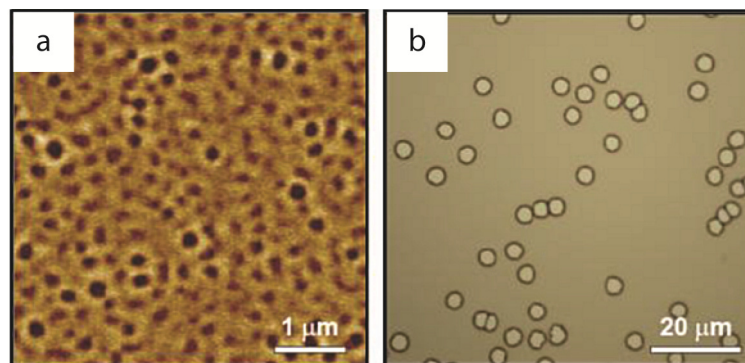
Figure 1.5: Mechanisms leading to the onset of dewetting in polymer films: (a) spinodal dewetting in a 4 nm thick polystyrene film on silicon imaged by atomic force microscopy (AFM) and (b) heterogeneous nucleation in a 33 nm thick polystyrene film on silicon imaged by optical microscopy. Adapted from work by Ghezzi[88].

Heterogeneous nucleation is characteristic of most unstable and metastable films, with defects of the substrate (e.g. dust or scratches)[58] and high residual film stresses from the polymer casting process leading to film rupture and film dewetting.[38-39, 42]
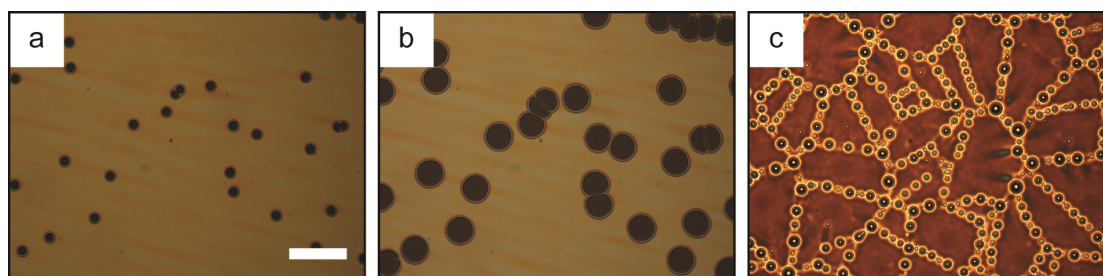
Figure 1.6: Optical micrographs illustrating the three main stages of dewetting a poly (4vinylpyridine) film on polystyrene substrate. (a) Hole nucleation followed by (b) hole growth and coalescence culminating in the formation of (c) isolated droplets on the substrate.

The heterogeneous nucleation mechanism of holes can be divided into the three stages shown in Figure 1.6: (a) film rupture, (b) hole growth and (c) the formation of isolated droplets.[89] The rupture of an initially homogeneous film leading to hole nucleation at sites of localised heterogeneity represents the onset of dewetting (Figure 1.6(a)).
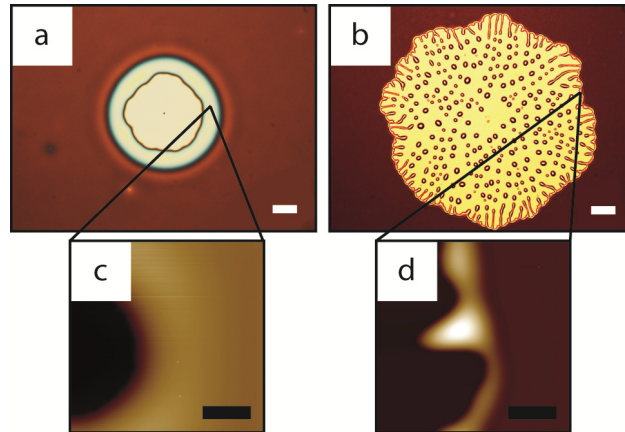
Figure 1.7: Two types of rim surround dewetting hole in polystyrene film. (a) Optical microscopy image showing the morphology of a stable rim around a dewetted hole and (c) an artificially rendered AFM micrograph of a stable, shallow, cylindrical rim with no undulations and fingering. Height scale = 400 nm. (b) Optical microscopy image showing the morphology of a hole with unstable rim morphology and an (d) AFM artificially rendered micrograph illustrating the undulations in the rim. Height scale = 1.5 μm. (a-b) Scale bars = 200 μm and (c-d) scale bars = 20 μm.

Following film rupture, nucleated holes grow in size radially, minimising the area of contact between the dewetting liquid and the substrate (Figure 1.6(b)). Hole growth occurs by the displacement of liquid material from substrate into a rim surrounding the hole (Figure 1.7(a,c)). During the early stages of dewetting, energy is dissipated due to slip of the dewetting liquid along the substrate interface, characterised by the radial growth proportional to $t^{2/3}$. As the rim width grows, the dewetting rate is retarded over time and viscous dissipation within the liquid film dominates the hole growth. Here slip ceases to be important and the hole grows linearly with time. In the cases where interfacial slip is strong, undulations of the rim shape lead to fingering and radial droplet shedding within the hole (Figure 1.7(b,d)). In these cases, the hole grows linearly with time at a rapid velocity, which is the subject of discussion in Chapter 4.[56] Slip behaviour at the liquid-substrate interface is discussed further in Section 1.3.3 below. The hole growth rate is inversely

proportional to the viscosity of the liquid film in both regimes, therefore the dewetting rate is found to increase with increasing annealing temperature above T_g and decreasing polymer molecular weight.[30, 34, 53, 90]

Hole coalescence is the final stage of film dewetting, whereby the rims of adjacent holes overlap to form liquid cylinders on the substrate. These cylinders eventually decay over time, due to Rayleigh-Plateau instability, into single isolated droplets that obtain a spherical-cap shape with an equilibrium Young's contact angle (Figure 1.6(c)). Where films have dewetted with radial droplet shedding, more numerous and finer droplets are deposited on the substrate (Figure 1.7(b)).

1.3.2   Annealing methods

For a non-wetting polymer film to dewet from a substrate, it must be in a melt or liquid state where the polymer chains are able to flow relative to each other and the substrate. This may be achieved by heating the polymer film above its glass transition temperature, T_g or by suppressing the T_g of the film below the ambient temperature in the presence of a good solvent, which preferentially binds to the polymer chains. Thermally annealing a polymer film on a hot plate or in an oven is a simple procedure; however dewetting will depend on the nature of the interactions between the polymer film and the substrate; where different hole, rim and droplet morphologies can be achieved by the choice of polymer, initial film thickness and substrate material.[47, 52, 80, 89, 91]

Solvent annealing of polymer films, discussed in Chapters 4 and 5, has been more recently explored and provides a more complex pathway to the dewetting of polymer films, but also greater flexibility in preparing desired surface architectures through modifying the choice of solvent(s) in the liquid or vapour phases. Solvent annealing can therefore be used to dewet films that are otherwise stable on the substrate.[54-57, 92-93] For example, changing pH during solvent annealing has been shown to produce reversible dewetting behaviour of a polyvinylpyridine film on a silicon oxide surface. [94]

Alternative annealing techniques include the initiation of dewetting by laser light of both metal [95-96] and polymer films.[97] Electrical fields have also been used to create ordered dewetted polymer structures[84] as well as combinations of electrical and thermal stimulation.[85] On non-wetting substrates it may be possible to observe

dewetting of volatile liquids which evaporate until a critical film thickness is reached, at which point the film will spontaneously dewet from the substrate.[98] It has also been shown that casting a dilute polymer solution from a volatile solvent onto a non-wetting substrate will also lead to dewetting patterns of the polymer at the evaporating solvent front.[99]

1.3.3   Slip behaviour at the solid-polymer interface

Slip of a flowing liquid on a solid substrate can be described by the velocity profile along the height of the liquid film. In a no-slip regime, there is significant adsorption of the liquid to the substrate and no flow is experienced at the interface (Figure 1.8(a)). In a partial slip regime, adsorption at the solid-liquid interface is overcome and partial flow may occur, where the velocity of the interface is a fraction of the velocity at the free surface (Figure 1.8(b)). Complete slip, otherwise known as plug flow, occurs in highly viscous or solid systems where the velocity at the interface is the same as at the free surface without relative motion in the material within the film layer (Figure 1.8(c)). Apparent slip is expected for low viscosity liquid films with strong adsorption and no flow at the solid interface (Figure 1.8(d)).[12, 29, 100]
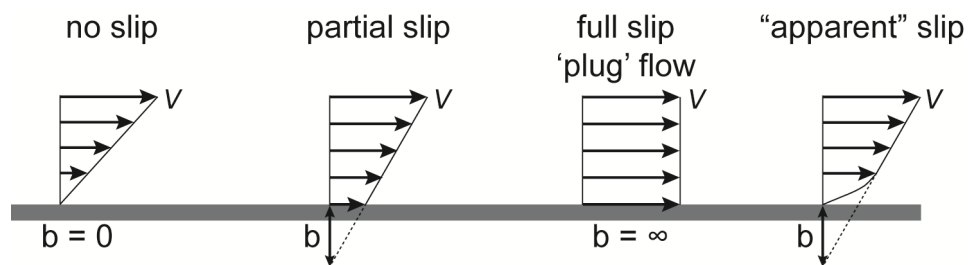
Figure 1.8: Illustration of velocity profiles in the vicinity of the solid/liquid interface. (a) No slip, (b) partial slip, (c) full slip "plug flow" (d) apparent slip.

For a flowing polymer melt, de Gennes expected long-chained polymers on an ideal, non-adsorbing substrate to exhibit an exceptional amount of slippage with the slip length b, defined as the distance at which the velocity of the flowing liquid extrapolates to zero, increasing as a function of the chain length, N of the polymer:[30, 101]

$$b = a \frac{N^3}{N_e^2} \qquad (1.8)$$

where a is the size of the monomer and N_e the entanglement length. This was based on the assumption that the polymer-solid friction coefficient should be identical to that of a simple liquid of monomers which is in contact with the solid substrate. Therefore a no-slip boundary condition would exist with a slip length comparable to the size of the monomers.[35] In practice, slip lengths that are lower than expected have been found at small flow velocities. [29] This has been explained by the adsorbed polymer chains on the substrate extending outwards and entangling with the bulk polymer leading to strong friction. As these adsorbed chains are not rigid they may deform and disentangle leading to a coil to stretch transition, where the friction coefficient is seen to decrease rapidly at larger shear strains. [30, 32, 35]

According to accepted models, in the initial dewetting period when the rim width is still growing and the dewetting velocity is dominated by interfacial slip, hole growth is described by the power law $D \propto t^{2/3}$.[29-30] In this regime the velocity is determined by:[34]

$$V_{slip} = \frac{1}{6} \frac{\gamma}{\eta} \theta^2 \frac{b}{w} \qquad (1.9)$$

with γ and η the surface tension and viscosity of the liquid respectively, θ the contact angle of the liquid on the substrate, and w the width of the rim. The velocity has been experimentally observed to decrease proportionally to the increasing rim width and a cross over to a no-slip, constant velocity regime occurs at a critical rim width.[34]

1.3.4   Role of elastic forces within the film

In the past 10 years there has been increased understanding of the chain equilibration process as an important driving force, in addition to interfacial interactions, for dewetting of thin films. [37-38, 40, 52, 102-105] The techniques used to cast polymers in solution onto a substrate, such as spin and dip coating, induce strongly out-of-equilibrium conformations of the chains and low entanglement density due to the fast evaporation of the solvent.[41-42] This leads to residual elastic stresses that

relax upon annealing, drastically affecting the dewetting rate,[37-38, 40] entanglement density,[42] viscosity and thermal expansion.[39, 43, 106-107]

Annealing the PS films above T_g drives the polymer chains away from their out-of-equilibrium 'frozen' conformation obtained through casting, towards more energetically favoured quasi-equilibrium conformations.[40] This elastic rearrangement has been described particularly in ultra-thin films where elastic forces due to extreme confinement are strong.[108] Ageing a cast film below T_g for a period of time has been shown to increase the stability of polymer films to dewetting during annealing. Reiter *et al.* found that the probability of film rupture, defined as the maximum number of circular holes per unit area, exponentially decayed as a function of increasing ageing time for a given film thickness. This trend was attributed to the reorientation of the polymer chains into conformations closer to their equilibrium.[38]

Damman *et al.* observed distinct transition times related to changes in dewetting velocity and rim shape and compared these values with the reptation time of the known chain lengths. They concluded that there is evidence for the relaxation of residual stresses within the rim region as the transition in the rim shape occurs at times well below the reptation time, for large molecular weight films. The transition in the velocity profile was observed to occur at times comparable to the reptation time of the polymer, taken by the author as validity of the hypothesis that chain re-entanglement occurs due to chain inter-diffusion.[37]

Yang *et al.* calculated, from the variation in surface contour at the edge of a dewetting hole, the molecular recoiling force due to residual stresses in polymer thin films as a function of molecular weight and film thickness. They concluded that the magnitude of this force was at least equal to, if not greater than, the dispersive forces present in flowing thin polymer films.[40]

1.3.5   Applications of dewetting induced micro-patterned polymer surfaces

The dewetting of thin polymer films from a solid substrate has been studied extensively over the past three decades,[29, 52, 80, 89, 109-111] and the surface patterns produced have interesting applications.[81, 112] Gentili *et al.* reviewed the application of the dewetting process for different functional materials and technologies.[81] The works reviewed explored a variety of processes that take advantage of the dewetting phenomenon. These included the use of dewetting as a vehicle for the distribution of

nanoparticles and the confinement and spatial control over dewetting films. They concluded that dewetting as a basis for fabrication processes is advantageous due to its applicability to any class of materials, mild conditions and additivity and allows the organization of materials across multiple length scales.[81]

Xue and Han include a short discussion on applications in their review of the strategies available for the formation of ordered patterns by utilizing polymer thin film dewetting.[112] They review the use of dewetted films as moulds for the transfer of patterns that are unable to be made by other methods as well as the possible combinations of dewetted patterns and functional materials to produce functional structures and devices. The size of patterns produced by dewetting are usually in the order of microns, which is an appropriate length scale for application in bio-sensing, cellular biology and as scaffolds for cell support. [4-5, 16, 112-113]

The application of thin film polymer dewetting to produce biomimetic patterned surface coatings for atmospheric water capture has also been shown to be promising by Thickett, Neto and Harris in 2011.[3]

1.3.6   Dewetting polymer bilayers

Multilayer polymer systems are particularly susceptible to the effects of layer inversion as well as the sequential co-dewetting of multiple layers, which are further discussed in Chapter 5. Both of these phenomena are related to the mobility of the underlying polymer and may be suppressed by preserving the substrate in a solid state.

A bilayer system composed of poly4vinylpyridine (P4VP) on polystyrene (PS) on a silicon wafer has previously been shown to readily dewet when thermally annealed above the T_g of P4VP, resulting in the formation of hydrophilic P4VP droplets on top of a hydrophobic PS background.[3] Due to the T_g of both polymers, 100 °C for PS and 137 °C for P4VP, being similar and below the annealing temperature, thermal annealing of this system was found to lead to layer inversion due to the relative viscosities of the two layers and the surface energy minimisation driving force for intermixing and inversion (Figure 1.9(a)). Certain solvent annealing conditions for the same bilayer system can also lead to sequential dewetting in both layers resulting in steps of different topography and chemistry (Figure 1.9(b)).
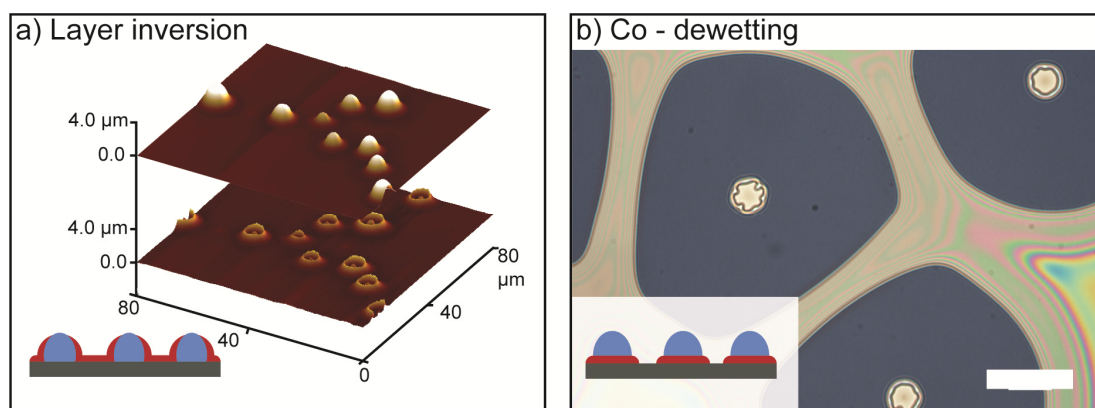
Figure 1.9: (a) Atomic force microscopy (AFM) image of layer inversion in a P4VP/PS bilayer after thermal annealing at 180°C. The top micrograph shows P4VP droplets on the PS background; the bottom micrograph shows the pronounced PS rims remaining when the P4VP droplets are selectively dissolved. Inset: schematic of P4VP dewetted droplets (in blue) becoming partly coated in PS (in red). (b) Optical micrograph of a co-dewetted P4VP/PS bilayer annealed in toluene – ethanol (31: 69) vapour mixture. Scale bar = 100 μm. Inset: schematic of co-dewetting of P4VP (blue) and PS (red).

The density of nucleated holes and isolated droplets as well as the contact angle of the droplets on the solid substrate can all be tuned by adjusting the annealing conditions. The stability of the rim surrounding the hole can dramatically alter the isolated polymer droplet density on the substrate and the size of the isolated droplets. Film thickness is the primary method by which these parameters may be tuned. Increasing film thickness leads to decreasing hole density and larger isolated droplets.[3, 52] Furthermore, increasing film thickness can also lead to a transition from a system with holes that are surrounded by unstable rims, towards a more stable rim structure.[56] It is also possible to alter the receding contact angle of the hole rims during hole growth as well as the equilibrium contact angle of the isolated droplets on the substrate, by altering substrate material[114] or the solvent annealing conditions.[94]

1.4 Atmospheric Water Harvesting: An Application of Micro-Patterned Surfaces

The World Economic Forum, in its latest annual risk report, has listed water crises as the leading global potential risk in terms of impact and eighth in terms of likelihood.[115] In a recent study on monthly global water scarcity, Mekonnen and

Hoekstra concluded that two thirds of the global population (4 billion people) live under severe water scarcity for at least one month of the year.[116] Furthermore, half a billion people face year-round severe water scarcity. The authors propose that regulatory oversight and improvements in agricultural efficiency will be necessary to meet the future demand for freshwater. Increasing and diversifying the supply of freshwater by technological innovation will assist in averting the predicted water crises. Harvesting fresh water from atmospheric humidity and fog is a method that has been previously proposed[117] and could be utilised as a source of freshwater for regions around the world without ready access to surface and groundwater resources.

There are many prototype systems currently distributed worldwide and are used to study the viability and optimise the efficiency of different water collection processes.[117-122] The concept of passive water collection, where no external source of energy is required to condense water vapour from the ambient environment, has been investigated for many years. A pioneering study was undertaken by Friedrich Zibold, in the early 20th century, to recreate what was believed to be ancient Greek stone dew condensers above an extensive pipe system.[123-124] It was believed that these porous stone structures relied on night time irradiation to obtain a lower temperature than the temperature of the surrounding humid environment during the early morning hours. Zibold's work increased interest in the field, leading to other studies on the use "aerial wells" for water collection (Figure 1.10). Later excavations of the mounds showed that they were ancient burial sites, which were unrelated to the underlying water channels and pipe systems. Furthermore, the water collection results from experiments with aerial well systems were poorer than expected.[124] Numerical simulations by Nikolayev *et al.* and condensation studies by Beysens have suggested that "grass like" condensers, thin sheets which are thermally isolated from the ground and of a wetting material, achieve better water collection efficiencies than the Zibold-type condensers.[124-126] Other scientific explorations on the subject matter of atmospheric water are provided in an interesting and extensive historical review by Moller.[127]

Figure 1.10: Knapen water condenser (1932) in Trans-en-Provence (France)[128]

Prototype projects on the use of reflective hydrophilic polyethylene sheets for the purpose of water collection, in accordance with the principles outlined in Nikolayev's work, were conducted in the semi-arid Kutch region of India.[126] In this study, a large trapezoidal shaped trough inset into the earth was lined with the reflective sheets which were insulated from the ground by polystyrene foam. Numerical simulations were initially used to design the most efficient geometry of the condenser system, taking into consideration the historical data on the speed and direction of prevailing winds as well as ambient temperatures. The large system was found to collect 6545 L for 2007, corresponding to 251.4 L per night. These reflective hydrophilic sheets are produced by the International Organisation for Dew Utilisation (OPUR) who promote and support the endeavours of research groups and institutions in pursuing the goal of the viable collection of atmospheric water.

Maestre-Valero *et al.* compared the use of a black polyethylene material[129] to the reflective hydrophilic material used in the previous study.[126] They observed that although the hydrophilicity of the reflective material resulted in more dew events, overall the water collection was found to be greater with the black foil and concluded that the improved performance was due to the higher emissivity of the material over a greater range of the IR spectrum.[129]

Alternatively to the condensation dew from humid air, commercial ventures use water harvesting from fog by collecting the airborne water droplets in areas of recurring fog events using structures erected incident to the prevailing wind direction (Figure 1.11).[118, 120] Research in this field is exploring the type of mesh material and the dimensions and geometry of the mesh to optimise water collection. In the field of

fog collection, Fogquest is an organisation that supports projects to supply arid under-developed regions with water and who host an annual conference into fog, fog collection and dew. The occurrence of fog collection in nature has also been studied as a source of bio-inspiration towards the development of efficient collection surfaces and materials.[62, 130-133] Other studies into alternative water collection methods include the experimental application of humidification/dehumidification cycling of desiccant solutions[119, 122] and a theoretical study of a solar cyclone concept.[134]

Figure 1.11: Mesh structure used for fog water collection in Bellavista, Peru.[135]

The application of chemically and topographically micro-patterned surfaces to the collection of atmospheric water has been the subject of study since the initial observation and experimental simulation by Parker and Lawrence of the fog harvesting adaptations of the Namib Desert *Physosterna cribripes* beetle.[62-63] In this pioneering study, a surface of glass beads embedded within wax was used to mimic the concept of atmospheric water condensation on hydrophilic nodes, and the collection of droplets that reach a critical volume and roll off along a hydrophobic background. The results indicated that a surface, patterned in this manner was the most effective for water harvesting. Since 2001 the concept has been developed by utilising different materials, including the introduction of surface roughening to promote superhydrophobicity,[33] alternative surface geometries and various material fabrication processes.[64, 136-137 2, 60-61, 138]

1.4.1   The design of a surface for water collection

The collection of water can be dissected into three continuous phases beginning with the heterogeneous nucleation of water on the surface, followed by the growth and coalescence of the water droplets, until a large droplet of critical mass is able to finally slide, or roll, off the surface. The theory of droplet behaviour during each of these stages has been discussed in Section 1.2. The experimental works related to the behaviour of condensing water vapour on micro-patterned surfaces and collection of the condensate will be discussed here (Figure 1.12).

Condensation of water on a chemically heterogeneous surface with a wettability gradient will preferentially occur on the more hydrophilic regions, illustrated in Figure 1.12(a) by the nucleation of water droplets on a hydrophilic polymer network on top of a hydrophobic polymer film.[3, 67, 139-142] In order to maximise the contrast in wettability on the micro-patterned surface, a superhydrophobic background, achieved by roughening the hydrophobic regions on the nano length scale, has been used (Figure 1.12(c)). On these regions the water droplet obtains an almost spherical shape with a contact angle approaching 180°.[64, 136, 139, 143-147] Typically superhydrophobic surfaces have very low contact angle hysteresis, $\theta_a - \theta_r < 10°,$ resulting in droplet roll-off at very small critical volumes as predicted by Equation 1.3. However, two problems exist when using superhydrophobic surfaces as the background material to a micro-patterned water collection surface.

Firstly, superhydrophobicity is achieved by the support of a water droplet on an air cushion provided by trapped air within the textured surface.[33, 68] The condensation of water onto such a surface leads to random nucleation above and within the texture. Growth and coalescence of these droplets can lead to the displacement of the air cushion and subsequent pinning of the droplets in, what is referred to as, the Wenzel state, which reduces the contact angle of the droplets and increases the contact angle hysteresis.[145, 148-149] The second issue, lies with the energy barrier to droplet roll off at the contact line between hydrophilic and hydrophobic regions. Where this wettability contrast is high, a strong hysteretic force against droplet roll-off has been simulated and observed.[138, 150-151] It becomes an optimisation question to balance the wettability contrast against the increase in hysteresis at the hydrophilic/hydrophobic contact line and the roll off volume of the water droplet in order to maximise the water collection

rate.[142] Finally, as shown by Miljkovic *et al.*, the air cushion within the nano-texture on a superhydrophobic surface has a high resistance to heat transfer, leading to water droplet growth rates that are significantly lower than for droplets under the same conditions condensing and growing on a non-textured hydrophobic surface.[145]

Alternative micro-patterned structures that have been proposed for water condensation and collection include one dimensional fibres such as artificial spider silk (Figure 1.12(b)) and cacti needle mimics[152-153] as well as materials that respond to external stimuli, such as temperature to alter their chemical composition and physical structural.[154] Other surfaces have been designed to trap hydrophobic liquids as the background medium to facilitate the removal of nucleated water droplets.[155-157]
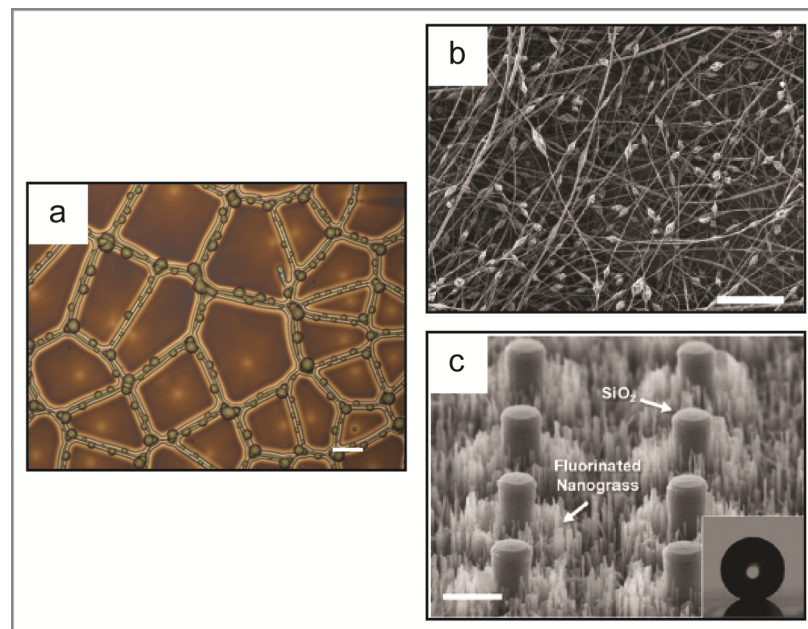
Figure 1.12: Micro-patterned structures for atmospheric water collection. (a) P4VP/PS dewetted bilayer developed in this Thesis displaying preferential water nucleation on the P4VP network. Scale bar = 20 μm (b) Spider silk mimic with chemical and geometrical contrast between the knots and the fibre.[152] Scale bar = 100 μm (c) Etched hydrophilic micro pillars and super hydrophobic 'nanograss' background resulting in an extreme wettability contrast.[137] Scale bar = 10 μm

1.4.2   Characterisation of water collection surfaces

The most common experimental method to determine the water collection efficiency of purpose-designed materials is to mount modified or coated two dimensional substrates on a cooling module within a humid environment at a desired angle from the vertical. A collection tray situated below the sample collects the water

droplets that roll off the surface and after a period of time the mass of the collected water is noted. Typically the results are reported as the volume of water normalised against the projected surface area of the surface and the time frame of the experiment and in some cases a camera is used to image the formation and roll-off of droplets from the substrate. [60-61, 64, 158] An alternative setup, used by Wang and co-workers, utilised a tube with a modified outer surface and cooled by an internal coolant flow, where the tube was placed within a sealed humid environment. With this system the authors could image the water droplet geometry as well as calculate the heat transfer coefficient of their material.[157, 159]

Qualitative experiments into the observed growth behaviour of water droplets on a modified or coated surface are conducted by microscopic techniques, as demonstrated in Figure 1.12, which are summarised in Section 2.6.[3, 59-60, 137] High resolution studies into the nucleation of water droplets are often conducted within an environmental scanning electron microscope (ESEM), where a humid environment can be produced by altering the pressure within a sealed chamber with liquid water present.[137, 159-161]

1.5   Thesis Outline

This Thesis describes the design, fabrication and testing of polymer coatings, featuring chemical and topographical nano, micro and macro scale patterning, for the purpose of atmospheric water collection. Surface micro-patterning was achieved by exploiting the dewetting phenomenon of single and bilayer polymer films. The common materials and methodologies to all experimental work presented in this Thesis are summarised in Chapter 2, including the preparation and surface characterisation methods.

The design of the apparatus for water collection performance characterisation of the surface coatings is presented in Chapter 3. This Chapter includes the process and instrumentation diagram for the setup as well as the start-up and testing protocols and the instructions for safe operation. Opportunities for further refinements to the apparatus, experimental restrictions and the difficulties experienced during the design and development are also discussed here.

The roles of good and poor solvents in a vapour mixture in initiating and driving dewetting of polystyrene films on a silicon wafer are discussed in Chapter 4. The combination of toluene and ethanol is believed to increase the elastic stresses within the polymer film leading to rapid dewetting and an unstable rim structure with extensive droplet shedding. The morphology of dewetting polystyrene holes and dewetting rate are shown to rely on the relative concentration of each solvent. Furthermore, polystyrene films up to 500 nm in thickness are shown to dewet in the saturated vapour environment of this solvent mixture as are films that have been thermally aged for extensive periods of time.

Chapter 5 outlines the use of three solvents; ethanol, acetone and water in binary and ternary mixtures, to vapour anneal P4VP/PS bilayers leading to the P4VP film dewetting from the underlying PS film. The dewetting rates and hole growth profiles, as well as the morphologies of the rims surrounding the holes, and the geometries of P4VP droplets at the conclusion of dewetting, were systematically analysed for each solvent vapour environment. The role of each solvent in initiating and facilitating the dewetting of P4VP is discussed in terms of its quality as a solvent for both PS and P4VP. As bilayer polymer systems are susceptible to layer inversion or co- dewetting of both layers during annealing, the solvents were also chosen to suppress these phenomena.

The water condensation behaviour and water collection efficiency of patterned polymer coatings which are prepared by the dewetting of bilayer films using the acetone-water vapour mixture solvent annealing technique developed in Chapter 5, are presented in Chapter 6. Patterns at nano, micro and macroscopic length scales were prepared by dewetting P4VP films up to 900 nm in thickness from a PS substrate using this method. The water condensation behaviour of these surface coatings was observed and analysed using optical microscopy and the wettability characterised by contact angle goniometry. The water collection efficiency of the coatings was compared against a hydrophobic polystyrene coating in the purpose-built apparatus presented in Chapter 3.

Finally, the findings are summarised and the overall conclusions are presented in Chapter 7.

1.6   References

1.   Rogers, J. A.; Nuzzo, R. G. Recent progress in soft lithography. *Mater. Today* **2005,** *8* (2), 50-56.

2.   Lee, S.; Lee, J.; Park, C.; Lee, C.; Kim, K.; Tahk, D.; Kwak, M. Continuous fabrication of bio-inspired water collecting surface via roll-type photolithography. *Int. J. Precis. Eng. Man.* **2014,** *1* (2), 119-124.

3.   Thickett, S. C.; Neto, C.; Harris, A. T. Biomimetic surface coatings for atmospheric water capture prepared by dewetting of polymer films. *Adv. Mater.* **2011,** *23* (32), 3718-3722.

4.   Telford, A.; Meagher, L.; Glattauer, V.; Gengenbach, T.; Easton, C.; Neto, C. Micropatterning of polymer brushes: grafting from dewetting polymer films for biological applications. *Biomacromolecules* **2012,** *13* (9), 2989-2996.

5.   Ghezzi, M.; Wang, P. Y.; Kingshott, P.; Neto, C. Guiding the Dewetting of Thin Polymer Films by Colloidal Imprinting. *Adv. Mater. Interfaces* **2015,** *2* (11).

6.   Simpson, J. T.; Hunter, S. R.; Aytug, T. Superhydrophobic materials and coatings: a review. *Rep. Prog. Phys.* **2015,** *78* (8), 086501.

7.   Zhang, P.; Lv, F. A review of the recent advances in superhydrophobic surfaces and the emerging energy-related applications. *Energy* **2015,** *82*, 1068-1087.

8.   Rodríguez-Hernández, J. Wrinkled interfaces: Taking advantage of surface instabilities to pattern polymer surfaces. *Prog. Polym. Sci.* **2015,** *42*, 1-41.

9.   Yao, X.; Song, Y.; Jiang, L. Applications of Bio-Inspired Special Wettable Surfaces. *Adv. Mater.* **2011,** *23* (6), 719-734.

10.   Whitesides, G. M. The origins and the future of microfluidics. *Nature* **2006,** *442* (7101), 368-373.

11.   McDonald, J. C.; Duffy, D. C.; Anderson, J. R.; Chiu, D. T.; Wu, H.; Schueller, O. J. A.; Whitesides, G. M. Fabrication of microfluidic systems in poly (dimethylsiloxane). *Electrophoresis* **2000,** *21* (1), 27-40.

12.   Lee, T.; Charrault, E.; Neto, C. Interfacial slip on rough, patterned and soft surfaces: A review of experiments and simulations. *Adv. Colloid Interface Sci.* **2014,** *210*, 21-38.

13.   Park, K. C. Energy-Efficient Applications using Surfaces with Special Wettabilities. *J Nanotech. Smart. Mater.* **2014,** *1*, 1-9.

14.   Alves, N. M.; Pashkuleva, I.; Reis, R. L.; Mano, J. F. Controlling cell behavior through the design of polymer surfaces. *Small* **2010,** *6* (20), 2208-2220.

15.   Franke, K.; Kurth, I.; Bornhäuser, M.; Werner, C.; Pompe, T. Biomimetic microcavities based on poly (dimethylsiloxane) elastomers. *Soft Matter* **2009,** *5* (18), 3505-3510.

16.   Ghezzi, M.; Thickett, S. C.; Telford, A. M.; Easton, C. D.; Meagher, L.; Neto, C. Protein Micropatterns by PEG Grafting on Dewetted PLGA Films. *Langmuir* **2014,** *30* (39), 11714-11722.

17.   Kurth, I.; Franke, K.; Pompe, T.; Bornhäuser, M.; Werner, C. Extracellular matrix functionalized microcavities to control hematopoietic stem and progenitor cell fate. *Macromol. Biosci.* **2011,** *11* (6), 739-747.

18.   Telford, A. M.; James, M.; Meagher, L.; Neto, C. Thermally cross-linked PNVP films as antifouling coatings for biomedical applications. *ACS Appl. Mater. Interfaces* **2010,** *2* (8), 2399-2408.

19.   Théry, M. Micropatterning as a tool to decipher cell morphogenesis and functions. *J. Cell Sci.* **2010,** *123* (24), 4201-4213.

20.   Théry, M.; Racine, V.; Piel, M.; Pépin, A.; Dimitrov, A.; Chen, Y.; Sibarita, J. B.; Bornens, M. Anisotropy of cell adhesive microenvironment governs cell internal organization and orientation of polarity. *Proc. Natl. Acad. Sci. USA* **2006,** *103* (52), 19771-19776.

21.   Ju, J.; Zheng, Y.; Jiang, L. Bioinspired One-Dimensional Materials for Directional Liquid Transport. *Acc. Chem. Res.* **2014**.

22.   Tsai, I. Y.; Crosby, A. J.; Russell, T. P. Surface patterning. *Methods Cell Biol.* **2007,** *83*, 67-87.

23.   Singh, T. B.; Sariciftci, N. S. Progress in plastic electronics devices. *Annu. Rev. Mater. Res.* **2006,** *36*, 199-230.

24.   Black, C. T.; Ruiz, R.; Breyta, G.; Cheng, J. Y.; Colburn, M. E.; Guarini, K. W.; Kim, H. C.; Zhang, Y. Polymer self assembly in semiconductor microelectronics. *IBM J. Res. Dev.* **2007,** *51* (5), 605-633.

25.   Valkama, S.; Kosonen, H.; Ruokolainen, J.; Haatainen, T.; Torkkeli, M.; Serimaa, R.; ten Brinke, G.; Ikkala, O. Self-assembled polymeric solid films with temperature-induced large and reversible photonic-bandgap switching. *Nat, Mater.* **2004,** *3* (12), 872-876.

26.   Campbell, M.; Sharp, D.; Harrison, M.; Denning, R.; Turberfield, A. Fabrication of photonic crystals for the visible spectrum by holographic lithography. *Nature* **2000,** *404* (6773), 53-56.

27.   Ferreira, P.; Alves, P.; Coimbra, P.; Gil, M. Improving polymeric surfaces for biomedical applications: a review. *J. Coating. Tech. Res.* **2015,** *12* (3), 463-475.

28.   Brisbois, E. J.; Handa, H.; Meyerhoff, M. E. Recent Advances in Hemocompatible Polymers for Biomedical Applications. In *Advanced Polymers in Medicine*; Springer, 2015, pp 481-511.

29.   Bäumchen, O.; Jacobs, K. Slip effects in polymer thin films. *J. Phys.: Condens. Matter* **2010,** *22* (3), 033102.

30.   Brochard-Wyart, F.; de Gennes, P. G.; Hervert, H.; Redon, C. Wetting and slippage of polymer melts on semi-ideal surfaces. *Langmuir* **1994,** *10* (5), 1566-1572.

31.   Fetzer, R.; Jacobs, K.; Münch, A.; Wagner, B.; Witelski, T. New slip regimes and the shape of dewetting thin liquid films. *Phys. Rev. Lett.* **2005,** *95* (12), 127801.

32.   Münch, A.; Wagner, B. Impact of slippage on the morphology and stability of a dewetting rim. *J. Phys.: Condens. Matter* **2011,** *23* (18), 184101.

33.   Quéré, D. Wetting and Roughness. *Annu. Rev. Mater. Res.* **2008,** *38* (1), 71-99.

34.   Reiter, G.; Sharma, A. Auto-optimization of dewetting rates by rim instabilities in slipping polymer films. *Phys. Rev. Lett.* **2001,** *87* (16), 166103.

35.   Léger, L.; Hervet, H.; Massey, G.; Durliat, E. Wall slip in polymer melts. *J. Phys.: Condens. Matter* **1997,** *9* (37), 7719.

36.   Vilmin, T.; Raphaël, E. Dewetting of thin polymer films. *Eur. Phys. J. E* **2006,** *21* (2), 161-174.

37.   Damman, P.; Gabriele, S.; Coppée, S.; Desprez, S.; Villers, D.; Vilmin, T.; Raphaël, E.; Hamieh, M.; Al Akhrass, S.; Reiter, G. Relaxation of residual stress and reentanglement of polymers in spin-coated films. *Phys. Rev. Lett.* **2007,** *99* (3), 036101.

38.   Reiter, G.; Hamieh, M.; Damman, P.; Sclavons, S.; Gabriele, S.; Vilmin, T.; Raphaël, E. Residual stresses in thin polymer films cause rupture and dominate early stages of dewetting. *Nat, Mater.* **2005,** *4* (10), 754-758.

39.   Raegen, A.; Chowdhury, M.; Calers, C.; Schmatulla, A.; Steiner, U.; Reiter, G. Aging of thin polymer films cast from a near-theta solvent. *Phys. Rev. Lett.* **2010,** *105* (22), 227801.

40.   Yang, M.; Hou, S.; Chang, Y.; Yang, A. M. Molecular recoiling in polymer thin film dewetting. *Phys. Rev. Lett.* **2006,** *96* (6), 066105.

41.   Thomas, K. R.; Steiner, U. Direct stress measurements in thin polymer films. *Soft Matter* **2011,** *7* (17), 7839-7842.

42.   Barbero, D. R.; Steiner, U. Nonequilibrium polymer rheology in spin-cast films. *Phys. Rev. Lett.* **2009,** *102* (24), 248303.

43.   Clough, A.; Chowdhury, M.; Jahanshahi, K.; Reiter, G.; Tsui, O. K. Swelling with a Near-Θ Solvent as a Means to Modify the Properties of Polymer Thin Films. *Macromolecules* **2012,** *45* (15), 6196-6200.

44.   Grosberg, A. Y.; Khokhlov, A. Statistical Physics of Macromolecules; American Institute of Physics: New York, 1994. 1-144.

45.   Gabriele, S.; Sclavons, S.; Reiter, G.; Damman, P. Disentanglement time of polymers determines the onset of rim instabilities in dewetting. *Phys. Rev. Lett.* **2006,** *96* (15), 156105.

46.   Brochard-Wyart, F.; Debregeas, G.; Fondecave, R.; Martin, P. Dewetting of supported viscoelastic polymer films: Birth of rims. *Macromolecules* **1997,** *30* (4), 1211-1213.

47.   Seemann, R.; Herminghaus, S.; Jacobs, K. Dewetting Patterns and Molecular Forces: A Reconciliation. *Phys. Rev. Lett.* **2001,** *86* (24), 5534-5537.

48.   Sharma, A. Relationship of thin film stability and morphology to macroscopic parameters of wetting in the apolar and polar systems. *Langmuir* **1993,** *9* (3), 861-869.

49.   Sharma, A.; Khanna, R. Pattern formation in unstable thin liquid films. *Phys. Rev. Lett.* **1998,** *81* (16), 3463.

50.   Sferrazza, M.; Heppenstall-Butler, M.; Cubitt, R.; Bucknall, D.; Webster, J.; Jones, R. A. L. Interfacial instability driven by dispersive forces: The early stages of spinodal dewetting of a thin polymer film on a polymer substrate. *Phys. Rev. Lett.* **1998,** *81* (23), 5173.

51.   Sharma, A. Many paths to dewetting of thin films: anatomy and physiology of surface instability. *Eur. Phys. J. E* **2003,** *12* (3), 397-408.

52.   Reiter, G. Dewetting of thin polymer films. *Phys. Rev. Lett.* **1992,** *68* (1), 75.

53.   de Gennes, P. G. *Scaling concepts in polymer physics*; Cornell University Press, 1979.

54.   Xu, L.; Sharma, A.; Joo, S. W. Dewetting of stable thin polymer films induced by a poor solvent: role of polar interactions. *Macromolecules* **2012,** *45* (16), 6628-6633.

55.   Lee, S. H.; Yoo, P. J.; Kwon, S. J.; Lee, H. H. Solvent-driven dewetting and rim instability. *J. Chem. Phys.* **2004,** *121* (9), 4346-4351.

56.   Xu, L.; Shi, T.; An, L. The dewetting dynamics of the polymer thin film by solvent annealing. *J. Chem. Phys.* **2008,** *129* (4), 044904.

57.   Xue, L.; Han, Y. Autophobic Dewetting of a Poly(methyl methacrylate) Thin Film on a Silicon Wafer Treated in Good Solvent Vapor. *Langmuir* **2009,** *25* (9), 5135-5140.

58.   Müller-Buschbaum, P. Influence of surface cleaning on dewetting of thin polystyrene films. *Eur. Phys. J. E* **2003,** *12* (3), 443-448.

59.   Yu, T. S.; Park, J.; Lim, H.; Breuer, K. S. Fog Deposition and Accumulation on Smooth and Textured Hydrophobic Surfaces. *Langmuir* **2012,** *28* (35), 12771-12778.

60.   Zhang, L.; Wu, J.; Hedhili, M. N.; Yang, X.; Wang, P. Inkjet printing for direct micropatterning of a superhydrophobic surface: toward biomimetic fog harvesting surfaces. *J. Mater. Chem. A* **2015,** *3* (6), 2844-2852.

61.   Lee, A.; Moon, M. W.; Lim, H.; Kim, W. D.; Kim, H. Y. Water harvest via dewing. *Langmuir* **2012,** *28* (27), 10183-10191.

62.   Malik, F. T.; Clement, R. M.; Gethin, D. T.; Krawszik, W.; Parker, A. R. Nature's moisture harvesters: a comparative review. *Bioinspir. Biomim.* **2014,** *9* (3), 031002.

63.   Parker, A. R.; Lawrence, C. R. Water capture by a desert beetle. *Nature* **2001,** *414* (6859), 33-34.

64.   Garrod, R.; Harris, L.; Schofield, W.; McGettrick, J.; Ward, L.; Teare, D.; Badyal, J. Mimicking a stenocara beetle's back for microcondensation using plasmachemical patterned superhydrophobic-superhydrophilic surfaces. *Langmuir* **2007,** *23* (2), 689-693.

65.   Osti, R. 2008. Illustration of Namib Beetle harvesting water vapor; Ask Nature: asknature.org.

66.   Hamaker, H. C. The London—van der Waals attraction between spherical particles. *Physica* **1937,** *4* (10), 1058-1072.

67.   Beysens, D. The formation of dew. *Atmos. Res.* **1995,** *39* (1), 215-237.

68.   Bico, J.; Thiele, U.; Quéré, D. Wetting of textured surfaces. *Colloids Surf., A* **2002,** *206* (1), 41-46.

69.   Bonn, D.; Eggers, J.; Indekeu, J.; Meunier, J.; Rolley, E. Wetting and spreading. *Rev. Mod. Phys.* **2009,** *81* (2), 739-805.

70.   Cassie, A. B. D.; Baxter, S. Wettability of porous surfaces. *J. Chem. Soc., Faraday Trans.* **1944,** *40* (0), 546-551.

71.   Furmidge, C. Studies at phase interfaces. I. The sliding of liquid drops on solid surfaces and a theory for spray retention. *J. Colloid Sci.* **1962,** *17* (4), 309-324.

72.   Gao, L.; McCarthy, T. J. How Wenzel and Cassie Were Wrong. *Langmuir* **2007,** *23* (7), 3762-3765.

73.   McHale, G. Cassie and Wenzel: Were They Really So Wrong? *Langmuir* **2007,** *23* (15), 8200-8205.

74.   Bormashenko, E. Y. *Wetting of real surfaces*; De Gruyter: New York;Berlin;, 2013; Vol. 19.

75.   de Gennes, P. G.; Brochard-Wyart, F.; Quéré, D. *Capillarity and wetting phenomena: drops, bubbles, pearls, waves*; Springer Science & Business Media, 2013.

76.   Sigsbee, R. Vapor to condensed-phase heterogeneous nucleation. *Nucleation. Zettlemoyer AC. New York, Marcel Dekker* **1969**, 151-224.

77.   Meakin, P. Droplet deposition growth and coalescence. *Rep. Prog. Phys.* **1992,** *55* (2), 157.

78.   Platten, J.; Legros, J. Convection in fluids. *Berlin etc.: Springer-Verlag* **1984**.

79.   Rogers, T.; Elder, K.; Desai, R. C. Droplet growth and coarsening during heterogeneous vapor condensation. *Physical Review A* **1988,** *38* (10), 5303.

80.   Xie, R.; Karim, A.; Douglas, J.; Han, C.; Weiss, R. Spinodal dewetting of thin polymer films. *Phys. Rev. Lett.* **1998,** *81* (6), 1251.

81.   Gentili, D.; Foschi, G.; Valle, F.; Cavallini, M.; Biscarini, F. Applications of dewetting in micro and nanotechnology. *Chem. Soc. Rev.* **2012,** *41* (12), 4430-4443.

82.   Telford, A. M.; Thickett, S. C.; James, M.; Neto, C. Competition between Dewetting and Cross-Linking in Poly(N-vinylpyrrolidone)/Polystyrene Bilayer Films. *Langmuir* **2011,** *27* (23), 14207-14217.

83.   Thickett, S. C.; Harris, A.; Neto, C. Interplay between Dewetting and Layer Inversion in Poly (4-vinylpyridine)/Polystyrene Bilayers. *Langmuir* **2010,** *26* (20), 15989-15999.

84.   Schäffer, E.; Thurn-Albrecht, T.; Russell, T. P.; Steiner, U. Electrically induced structure formation and pattern transfer. *Nature* **2000,** *403* (6772), 874-877.

85.   Schäffer, E.; Harkema, S.; Roerdink, M.; Blossey, R.; Steiner, U. Thermomechanical lithography: pattern replication using a temperature gradient driven instability. *Adv. Mater.* **2003,** *15* (6), 514-517.

86.   Vrij, A. Possible mechanism for the spontaneous rupture of thin, free liquid films. *Discuss. Faraday Soc.* **1966,** *42*, 23-33.

87.   Konnur, R.; Kargupta, K.; Sharma, A. Instability and morphology of thin liquid films on chemically heterogeneous substrates. *Phys. Rev. Lett.* **2000,** *84* (5), 931.

88.   Ghezzi, M. Functional Surface Micropatterns by Dewetting of Thin Polymer Films. Doctor of Philosophy, University of Sydney 2015.

89.   Seemann, R.; Herminghaus, S.; Neto, C.; Schlagowski, S.; Podzimek, D.; Konrad, R.; Mantz, H.; Jacobs, K. Dynamics and structure formation in thin polymer melt films. *J. Phys.: Condens. Matter* **2005,** *17* (9), S267.

90.   Williams, M. L.; Landel, R. F.; Ferry, J. D. The temperature dependence of relaxation mechanisms in amorphous polymers and other glass-forming liquids. *J. Am. Chem. Soc.* **1955,** *77* (14), 3701-3707.

91.   Zhang, F.; Baralia, G.; Boborodea, A.; Bailly, C.; Nysten, B.; Jonas, A. M. Partial Dewetting of Polyethylene Thin Films on Rough Silicon Dioxide Surfaces. *Langmuir* **2005,** *21* (16), 7427-7432.

92.   Orlov, M.; Tokarev, I.; Scholl, A.; Doran, A.; Minko, S. pH-responsive thin film membranes from poly(2-vinylpyridine): Water vapor-induced formation of a microporous structure. *Macromolecules* **2007,** *40* (6), 2086-2091.

93.   Xu, L.; Shi, T.; An, L. Nonsolvent-Induced Dewetting of Thin Polymer Films. *Langmuir* **2007,** *23* (18), 9282-9286.

94.   Burtovyy, R.; Luzinov, I. Reversibility of pH-Induced Dewetting of Poly(vinyl pyridine) Thin Films on Silicon Oxide Substrate. *Langmuir* **2008,** *24* (11), 5903-5910.

95.   Favazza, C.; Kalyanaraman, R.; Sureshkumar, R. Robust nanopatterning by laser-induced dewetting of metal nanofilms. *Nanotechnology* **2006,** *17* (16), 4229.

96.   Bischof, J.; Scherer, D.; Herminghaus, S.; Leiderer, P. Dewetting modes of thin metallic films: nucleation of holes and spinodal dewetting. *Phys. Rev. Lett.* **1996,** *77* (8), 1536.

97.   Singer, J. P.; Lin, P. T.; Kooi, S. E.; Kimerling, L. C.; Michel, J.; Thomas, E. L. Direct - Write Thermocapillary Dewetting of Polymer Thin Films by a Laser - Induced Thermal Gradient. *Adv. Mater.* **2013,** *25* (42), 6100-6105.

98.   Yamamoto, D.; Nakajima, C.; Shioi, A.; Krafft, M. P.; Yoshikawa, K. The evolution of spatial ordering of oil drops fast spreading on a water surface. *Nat. Commun.* **2015,** *6*.

99.   Karthaus, O.; Gråsjö, L.; Maruyama, N.; Shimomura, M. Formation of ordered mesoscopic polymer arrays by dewetting. *Chaos* **1999,** *9* (2), 308-314.

100.   Neto, C.; Evans, D. R.; Bonaccurso, E.; Butt, H. J.; Craig, V. S. Boundary slip in Newtonian liquids: a review of experimental studies. *Rep. Prog. Phys.* **2005,** *68* (12), 2859.

101.   de Gennes, P. G. Ecoulements viscometriques de polymers enchevetres. *C.R. Acad. Sci. Paris Ser. B* **1979,** *288*, 219-220.

102.   Reiter, G. Dewetting of highly elastic thin polymer films. *Phys. Rev. Lett.* **2001,** *87* (18), 186101.

103.   Bollinne, C.; Cuenot, S.; Nysten, B.; Jonas, A. M. Spinodal-like dewetting of thermodynamically-stable thin polymer films. *Eur. Phys. J. E* **2003,** *12* (3), 389-396.

104.   Ediger, M.; Forrest, J. Dynamics near free surfaces and the glass transition in thin polymer films: a view to the future. *Macromolecules* **2013,** *47* (2), 471-478.

105.   Richardson, H.; Carelli, C.; Keddie, J.; Sferrazza, M. Structural relaxation of spin-cast glassy polymer thin films as a possible factor in dewetting. *Eur. Phys. J. E* **2003,** *12* (3), 437-441.

106.   Thomas, K. R.; Chenneviere, A.; Reiter, G.; Steiner, U. Nonequilibrium behavior of thin polymer films. *Phys. Rev. E* **2011,** *83* (2), 021804.

107.   Reiter, G.; de Gennes, P. G. Spin-cast, thin, glassy polymer films: Highly metastable forms of matter. *Eur. Phys. J. E* **2001,** *6* (1), 25-28.

108.   Zhao, W.; Rafailovich, M.; Sokolov, J.; Fetters, L.; Plano, R.; Sanyal, M.; Sinha, S.; Sauer, B. Wetting properties of thin liquid polyethylene propylene films. *Phys. Rev. Lett.* **1993,** *70* (10), 1453.

109.   de Gennes, P. G. Wetting: statics and dynamics. *Rev. Mod. Phys.* **1985,** *57* (3), 827.

110.   Srolovitz, D.; Safran, S. Capillary instabilities in thin films. I. Energetics. *J. Appl. Phys.* **1986,** *60* (1), 247-254.

111.   Saulnier, F.; Raphaël, E.; de Gennes, P. G. Dewetting of thin-film polymers. *Phys. Rev. E* **2002,** *66* (6), 061607.

112.   Xue, L.; Han, Y. Pattern formation by dewetting of polymer thin film. *Prog. Polym. Sci.* **2011,** *36* (2), 269-293.

113.   Thickett, S. C.; Moses, J.; Gamble, J. R.; Neto, C. Micropatterned substrates made by polymer bilayer dewetting and collagen nanoscale assembly support endothelial cell adhesion. *Soft Matter* **2012,** *8* (39), 9996-10007.

114.   Seemann, R.; Herminghaus, S.; Jacobs, K. Gaining control of pattern formation of dewetting liquid films. *J. Phys.: Condens. Matter* **2001,** *13* (21), 4925.

115.   World Economic Forum. *Global Risks 2015*: Geneva, Switzerland2015.

116.   Mekonnen, M. M.; Hoekstra, A. Y. Four billion people facing severe water scarcity. *Sci. Adv.* **2016,** *2* (2), e1500323.

117.   Beysens, D.; Milimouk, I. The case for alternative fresh water sources. *Pour les resources alternatives en eau, Secheresse* **2000,** *11* (4), 1-16.

118.   Fessehaye, M.; Abdul-Wahab, S. A.; Savage, M. J.; Kohler, T.; Gherezghiher, T.; Hurni, H. Fog-water collection for community use. *Renew. Sust. Energ. Rev.* **2014,** *29* (0), 52-62.

119.   Gandhidasan, P.; Abualhamayel, H. Investigation of humidity harvest as an alternative water source in the Kingdom of Saudi Arabia. *Water Environ. J.* **2010,** *24* (4), 282-292.

120.   Klemm, O.; Schemenauer, R. S.; Lummerich, A.; Cereceda, P.; Marzol, V.; Corell, D.; van Heerden, J.; Reinhard, D.; Gherezghiher, T.; Olivier, J. Fog as a Fresh-Water Resource: Overview and Perspectives. *Ambio* **2012,** *41* (3), 221-234.

121.   Tiedemann, K.; Lummerich, A. In *Fog harvesting on the verge of economic competitiveness*, 5th International Conference on Fog, Fog Collection and Dew Münster, Germany, 25/07/2010; 2010; Erdkunde: http://www.fogconference.org, pp 305-306.

122.   Wahlgren, R. V. Atmospheric water vapour processor designs for potable water production: a review. *Water Res.* **2001,** *35* (1), 1-22.

123.   Zibold, F. The role of underground dew in water supply of Feodosia. *Trudy opytnyh lesnitchestv* **1905,** (III).

124.   Nikolayev, V. S.; Beysens, D.; Gioda, A.; Milimouka, I.; Katiushin, E.; Morel, J. P. Water recovery from dew. *J. Hydrol.* **1996,** *182* (1–4), 19-35.

125.   Beysens, D.; Milimouk, I.; Nikolayev, V.; Muselli, M.; Marcillat, J. Using radiative cooling to condense atmospheric vapor: a study to improve water yield. *J. Hydrol.* **2003,** *276* (1), 1-11.

126.   Sharan, G.; Clus, O.; Singh, S.; Muselli, M.; Beysens, D. A very large dew and rain ridge collector in the Kutch area (Gujarat, India). *J. Hydrol.* **2011,** *405* (1), 171-181.

127.   Möller, D. On the history of the scientific exploration of fog, dew, rain and other atmospheric water. *Die Erde* **2008,** *139* (1-2), 11-44.

128.   Royon, M. Dew tower of Belgian engineer Achile Knappen in Trans-en-Provence Var. Wikimedia: commons.wikimedia.org, 2008.

129.   Maestre-Valero, J.; Martínez-Alvarez, V.; Baille, A.; Martín-Górriz, B.; Gallego-Elvira, B. Comparative analysis of two polyethylene foil materials for dew harvesting in a semi-arid climate. *J. Hydrol.* **2011,** *410* (1), 84-91.

130.   Ju, J.; Bai, H.; Zheng, Y.; Zhao, T.; Fang, R.; Jiang, L. A multi-structural and multi-functional integrated fog collection system in cactus. *Nat. Commun.* **2012,** *3,* 1247.

131.   Nørgaard, T.; Dacke, M. Fog-basking behaviour and water collection efficiency in Namib Desert Darkling beetles. *Front. Zool.* **2010,** *7* (1), 1-8.

132.   Roth-Nebelsick, A.; Ebner, M.; Miranda, T.; Gottschalk, V.; Voigt, D.; Gorb, S.; Stegmaier, T.; Sarsour, J.; Linke, M.; Konrad, W. Leaf surface structures enable the endemic Namib desert grass Stipagrostis sabulicola to irrigate itself with fog water. *J. R. Soc. Interface* **2012,** *9* (73), 1965-1974.

133.   Andrews, H.; Eccles, E.; Schofield, W.; Badyal, J. Three-Dimensional Hierarchical Structures for Fog Harvesting. *Langmuir* **2011,** *27* (7), 3798-3802.

134.   Kashiwa, B.; Kashiwa, C. B. The solar cyclone: A solar chimney for harvesting atmospheric water. *Energy* **2008,** *33* (2), 331-339.

135.   Lummerich, A. Fog Catchers Harvest Air's Water in Arid Places. National Geographic: news.nationalgeographic.com, 2007.

136.   Zhai, L.; Berg, M. C.; Cebeci, F. C.; Kim, Y.; Milwid, J. M.; Rubner, M. F.; Cohen, R. E. Patterned superhydrophobic surfaces: toward a synthetic mimic of the Namib Desert beetle. *Nano Lett.* **2006,** *6* (6), 1213-1217.

137.   Hou, Y.; Yu, M.; Chen, X.; Wang, Z.; Yao, S. Recurrent Filmwise and Dropwise Condensation on a Beetle Mimetic Surface. *ACS nano* **2014,** *9* (1), 71-81.

138.   Dorrer, C.; Rühe, J. Mimicking the Stenocara Beetle - Dewetting of Drops from a Patterned Superhydrophobic Surface. *Langmuir* **2008,** *24* (12), 6154-6158.

139.   Narhe, R.; Beysens, D. Nucleation and growth on a superhydrophobic grooved surface. *Phys. Rev. Lett.* **2004,** *93* (7), 076103.

140.   Varanasi, K. K.; Hsu, M.; Bhate, N.; Yang, W.; Deng, T. Spatial control in the heterogeneous nucleation of water. *Appl. Phys. Lett.* **2009,** *95* (9), 094101-3.

141.   Zhao, H.; Beysens, D. From droplet growth to film growth on a heterogeneous surface: condensation associated with a wettability gradient. *Langmuir* **1995,** *11* (2), 627-634.

142.   Ghosh, A.; Beaini, S.; Zhang, B. J.; Ganguly, R.; Megaridis, C. M. Enhancing Dropwise Condensation through Bioinspired Wettability Patterning. *Langmuir* **2014**.

143.   Dorrer, C.; Rühe, J. Some thoughts on superhydrophobic wetting. *Soft Matter* **2009,** *5* (1), 51-61.

144.   Enright, R.; Miljkovic, N.; Al-Obeidi, A.; Thompson, C. V.; Wang, E. N. Condensation on Superhydrophobic Surfaces: The Role of Local Energy Barriers and Structure Length Scale. *Langmuir* **2012,** *28* (40), 14424-14432.

145.   Miljkovic, N.; Enright, R.; Wang, E. N. Effect of Droplet Morphology on Growth Dynamics and Heat Transfer during Condensation on Superhydrophobic Nanostructured Surfaces. *ACS Nano* **2012,** *6* (2), 1776-1785.

146.   Nosonovsky, M.; Bhushan, B. Patterned nonadhesive surfaces: superhydrophobicity and wetting regime transitions. *Langmuir* **2008,** *24* (4), 1525-1533.

147.   Chen, C. H.; Cai, Q.; Tsai, C.; Chen, C. L.; Xiong, G.; Yu, Y.; Ren, Z. Dropwise condensation on superhydrophobic surfaces with two-tier roughness. *Appl. Phys. Lett.* **2007,** *90* (17), 173108-173108-3.

148.   Liu, Y.; Choi, C. H. Condensation-induced wetting state and contact angle hysteresis on superhydrophobic lotus leaves. *Colloid. Polym. Sci.* **2013,** *291* (2), 437-445.

149.   Rykaczewski, K.; Osborn, W. A.; Chinn, J.; Walker, M. L.; Scott, J. H. J.; Jones, W.; Hao, C.; Yao, S.; Wang, Z. How nanorough is rough enough to make a surface superhydrophobic during water condensation? *Soft Matter* **2012,** *8* (33), 8786-8794.

150.   Furuta, T.; Sakai, M.; Isobe, T.; Matsushita, S.; Nakajima, A. Sliding of Water Droplets on Hydrophobic Surfaces with Various Hydrophilic Region Sizes. *Langmuir* **2011,** *27* (11), 7307-7313.

151.   Nakajima, A.; Nakagawa, Y.; Furuta, T.; Sakai, M.; Isobe, T.; Matsushita, S. Sliding of Water Droplets on Smooth Hydrophobic Silane Coatings with Regular Triangle Hydrophilic Regions. *Langmuir* **2013,** *29* (29), 9269-9275.

152.   Dong, H.; Wang, N.; Wang, L.; Bai, H.; Wu, J.; Zheng, Y.; Zhao, Y.; Jiang, L. Bioinspired Electrospun Knotted Microfibers for Fog Harvesting. *Chemphyschem* **2012,** *13* (5), 1153-1156.

153.   Bai, H.; Tian, X.; Zheng, Y.; Ju, J.; Zhao, Y.; Jiang, L. Direction controlled driving of tiny water drops on bioinspired artificial spider silks. *Adv. Mater.* **2010,** *22* (48), 5521-5525.

154.   Yang, H.; Zhu, H.; Hendrix, M. M.; Lousberg, N. J.; Esteves, A.; Xin, J. H. Temperature - Triggered Collection and Release of Water from Fogs by a Sponge - Like Cotton Fabric. *Adv. Mater.* **2013,** *25* (8), 1150-1154.

155.   Smith, J. D.; Dhiman, R.; Anand, S.; Reza-Garduno, E.; Cohen, R. E.; McKinley, G. H.; Varanasi, K. K. Droplet mobility on lubricant-impregnated surfaces. *Soft Matter* **2013,** *9* (6), 1772-1780.

156.   Lalia, B. S.; Anand, S.; Varanasi, K. K.; Hashaikeh, R. Fog harvesting potential of Lubricant-Impregnated Electrospun Nanomats. *Langmuir* **2013**.

157.   Xiao, R.; Miljkovic, N.; Enright, R.; Wang, E. N. Immersion Condensation on Oil-Infused Heterogeneous Surfaces for Enhanced Heat Transfer. *Sci. Rep.* **2013,** *3*.

158.   White, B.; Sarkar, A.; Kietzig, A. M. Fog-harvesting inspired by the Stenocara beetle–an analysis of drop collection and removal from biomimetic samples with wetting contrast. *Appl. Surf. Sci.* (0).

159.   Miljkovic, N.; Enright, R.; Nam, Y.; Lopez, K.; Dou, N.; Sack, J.; Wang, E. N. Jumping-Droplet-Enhanced Condensation on Scalable Superhydrophobic Nanostructured Surfaces. *Nano Lett.* **2012,** *13* (1), 179-187.

160.   Chen, X.; Wu, J.; Ma, R.; Hua, M.; Koratkar, N.; Yao, S.; Wang, Z. Nanograssed micropyramidal architectures for continuous dropwise condensation. *Adv. Funct. Mater.* **2011,** *21* (24), 4617-4623.

161.   Nosonovsky, M.; Bhushan, B. Biomimetic superhydrophobic surfaces: multiscale approach. *Nano Lett.* **2007,** *7* (9), 2633-2637.

CHAPTER 2

Materials and Methods

2.1 Preparation of Polymer Coatings

Prior to coating, silicon substrates with a 1.8 nm native oxide layer (MMRC Pty Ltd, Malvern VIC, Australia) were thoroughly cleaned, to eliminate monolayer levels of adventitious contamination, by sequential sonication in ethanol and acetone, blow drying with pure nitrogen followed by exposure to a high pressure CO_2 "snow jet" (Applied Surface Technologies, NJ, USA) to remove particulate contaminants. The substrates were then annealed at 150°C to remove any condensed water and treated under air plasma for 1 min (Harrick Plasma, Ithaca NY, USA, model PDC-002) immediately prior to coating. Preparation of samples for the solvent annealing work presented in Chapters 4 and 5 was carried out in a class-100 laminar flow cabinet unless otherwise stated.

Polymer films were prepared by spin coating (Laurell Technologies, PA, USA, model WS400B-6NPP-LITE) from dilute solutions (Table 2.1) for the work presented in Chapters 4 and 5. Typically 25 – 50 µL of polymer solution (0.5 – 50 mg mL^{-1}) was deposited onto the clean silicon substrate and spun at 2500 – 6000 rpm to achieve the desired film thickness. Spin coating produces film of uniform thickness h, based on the following relationship:[1]

$$h \propto \frac{C_0 M}{\omega^{1/2}} \tag{2.1}$$

where C_0 is the concentration of the polymer solution, M is the molecular weight of the polymer and ω is the rotation speed.

Table 2.1: Technical details of the polymers and the notations used in this Thesis.

Polymer (solvent)	Denotation	M_w, kg mol^{-1} (M_w/M_n)	Supplier
Polystyrene (Toluene)	PS96k	96 (1.04)	Polymer Standards Service
	PS192k	192 (N/a)	Sigma Aldrich
	PS350k	350 (2.06)	Sigma Aldrich
Poly(4vinylpyridine) (Ethanol)	P4VP22k	22 (1.15)	Polymer Source Inc.
	P4VP60k	60 (N/a)	Sigma Aldrich

For the work presented in Chapter 6, copper substrates were prepared by polishing with metal polish (Autosol, TX, USA) and wiping with petroleum spirit,

followed by sonicating in ethanol and blowing dry with pure nitrogen. Plasma treatment and treatment in a solution bath of basic pH was not used as it led to extensive surface oxidation, as evidenced by surface discolouration.

Polymer films were cast onto the copper substrates by dip-coating (KSV, NIMA, Stockholm, Sweden). Dip coating was chosen to accommodate the coating of three-dimensional substrates, such as copper tubing, with polymer films. For dip coating, polymer solutions in Table 2.1 were prepared in concentrations between 0.5% – 7.5% wt. The substrates were coated with polymer films, of varying thickness, by immersing into the solution bath at a speed of 100 mm min^{-1}, allowed to rest for 1 min, and extracted at a constant speed between 15 and 200 mm min^{-1}. The film thickness was measured by spectroscopic ellipsometry and the dip coating process was identified to be in the viscous drag regime (Figure 2.1(b)).

In order to prepare a uniform polymer coating, several parameters which are summarised in Figure 2.1(a) must be considered. A discussion of the practical steps undertaken to prepare polymer coatings by dip coating is provided in Section 3.2.2. Figure 2.1(c) illustrates the force balance between the substrate and polymer solution that ultimately determines film thickness during substrate extraction. Theoretically the film thickness h_0, when a substrate is extracted from a dilute solution at a speed u, can be determined by the relationship:[2]

$$h_0 = k_i \left(\frac{E}{Lu} + Du^{2/3} \right) \tag{2.2}$$

where E is the evaporation rate, L is the substrate width, k_i is the solution composition constant, and D the solution physical-chemical characteristics as described by Faustini et al.[3]

In Chapters 5 and 6 bilayer films were prepared by casting the P4VP from solution onto the prepared PS layer using either spin coating or dip coating depending on the application. Film thicknesses for all the prepared samples are noted in the relevant chapter sections.
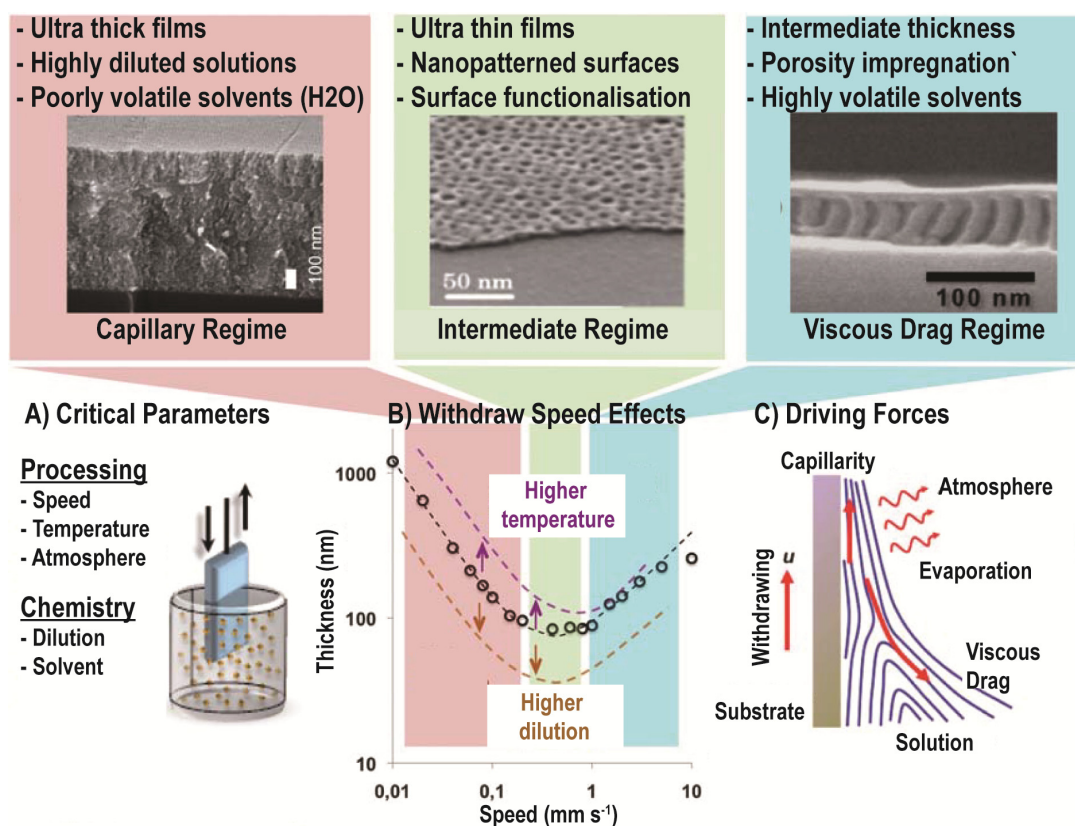
Figure 2.1: (a) Schematic illustration of the dip coating process and a list of parameters that affect the thickness of the prepared films. (b) Plot showing film thickness as a function of withdrawal speed overlayed with the effects of temperature and concentration. The different coating regimes as withdrawal speed is increased are described in further detail in the upper panels. (c) Schematic representation of the force balance that dictates film thickness on a withdrawing substrate. Reproduced from the review by Grosso[2]

2.2   Spectroscopic Ellipsometry

Optical spectroscopic ellipsometry was used to analyse the thickness of uniform polymer films by measuring the degree of elliptical polarisation of an incident light beam as it is reflected from the coated substrate being investigated.[4] The light beam emitted by our setup, from a polychromatic light source in the VIS-IR region, is linearly polarized, with perpendicular (*s* - polarization) and parallel (*p* - polarization) orthogonal polarisation components to the plane of incidence, before interacting with the sample. The change in polarization of the reflected light beam is determined by a second polarizer in combination with a detector (Figure 2.2).

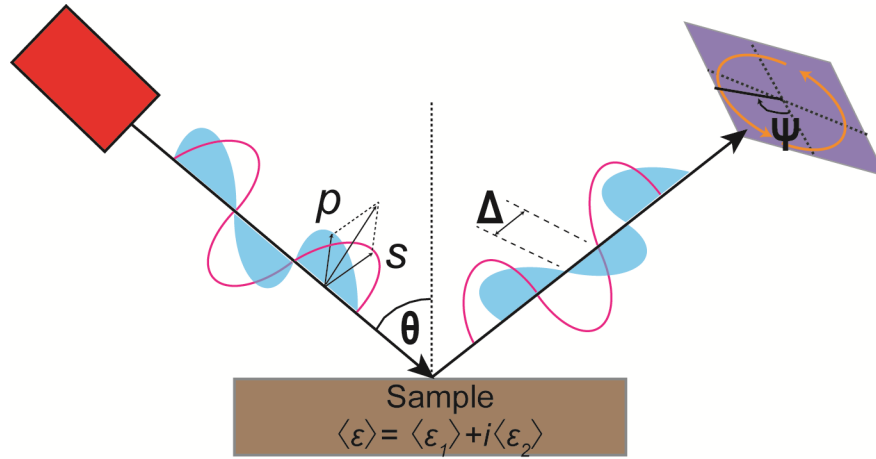Figure 2.2: Schematic representation of spectroscopic ellipsometry. A linearly polarised light beam interacts with a sample with dielectric function $\langle\varepsilon\rangle = \langle\varepsilon_1\rangle + i\langle\varepsilon_2\rangle$. The light beam becomes elliptically polarised following reflection from the surface and the detector records the change in phase angle (Δ) and amplitude ratio (Ψ).

The polarisation change is quantified by the amplitude ratio ψ, and the phase angle Δ. These parameters are related to the complex Fresnel reflectance coefficients for p and s-polarized light, r_p and r_s, respectively, by the complex ellipsometric parameter, ρ:[5]

$$\rho = \frac{r_p}{r_s} = tan(\Psi)e^{i\Delta} \qquad (2.3)$$

The complex ellipsometric parameter ρ, can be related to the complex dielectric function ε, of the material:

$$\langle\varepsilon\rangle = \langle\varepsilon_1\rangle + i\langle\varepsilon_2\rangle = \sin^2(\phi)\left[1 + \left(\frac{1-\rho}{1+\rho}\right)^2 \tan^2(\phi)\right] \qquad (2.4)$$

where ε_1 and ε_2 are the real and imaginary parts of the dielectric function respectively, and ϕ denotes the angle of incidence. The components of the dielectric coefficient are related by the refractive index n, and extinction coefficient k of the material:

$$\varepsilon_1 = n^2 - k^2 \qquad (2.5)$$

$$\varepsilon_2 = 2nk \qquad (2.6)$$

The experimental ψ and Δ values make it possible to obtain the thickness of the polymer coatings and optical constants of the material by performing a model analysis. Apart from the simplest of cases, information on the refractive index and thickness of all individual layers of a sample must be established in the correct order. Using iterative least squares minimisation, unknown optical constants and/or thickness parameters are varied and theoretical ψ and Δ values are calculated using the Fresnel equations to fit the experimental data.

In this body of work a J. A. Woollam Co. Inc. M-2000V spectroscopic ellipsometer was used to determine the thickness of the polymer coatings prepared by spin coating and dip coating on silicon and copper substrates. Measurements were performed using an angle of incidence of 75° in a wavelength range of 370 – 1000 nm. A model describing a multi-layer system was fitted to the experimental Ψ and Δ values in order to calculate the thickness and refractive index of the polymer films (Figure 2.3). For the polymer bilayer system, the model used to fit the ellipsometric data was:

<div align="center">substrate / oxide/ polymer 1/ polymer 2</div>

The Cauchy equation was used to model the refractive index of the polymer films:

$$n(\lambda) = A_n + \frac{B_n}{\lambda^2} + \frac{C_n}{\lambda^4} + \cdots, \qquad (2.7)$$

where n is the refractive index; λ is the wavelength of the incident light; A_n, B_n, C_n are the refractive index coefficients. The contributions of the fourth term and above are considered negligible for most applications.
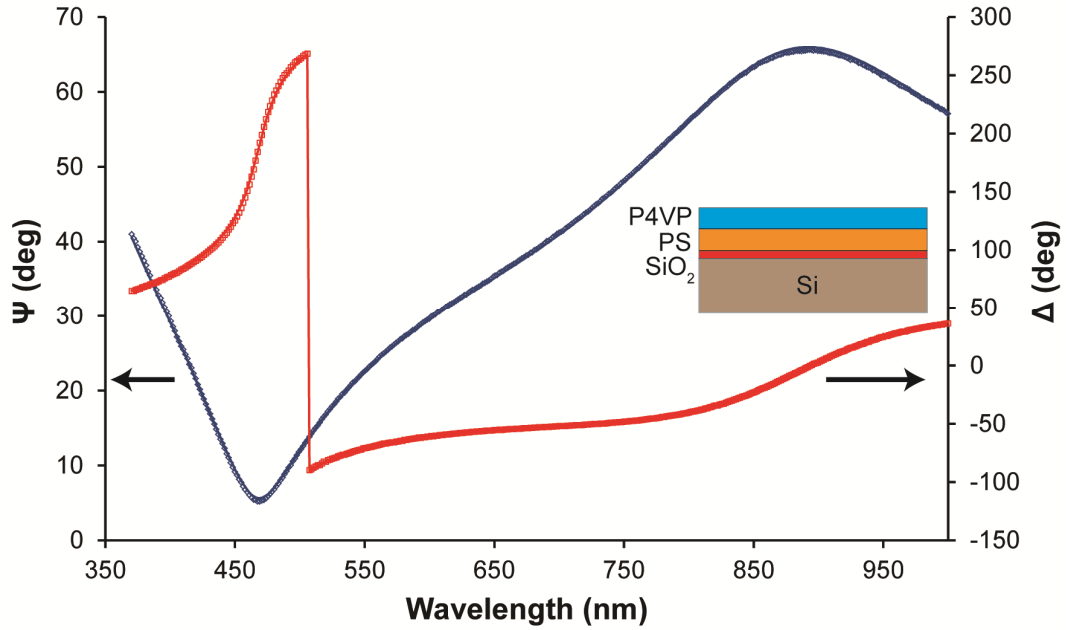
Figure 2.3: Experimental Ψ (◊) and Δ (□) data for a PS / P4VP bilayer on silicon with a native oxide layer acquired for wavelengths in the 370 – 1000 nm range at an angle of incidence of 75°. Experimental data were fitted with the multilayer model (solid lines) shown in the inset.

To minimise fitting errors, the complexity of the modelling was reduced by measuring the thickness and refractive index of each layer independently and setting the values to be constants when modelling subsequent layers (Table 2.2). The data was processed and fitted using the WVASE32 software provided with the instrument.

Table 2.2: Fitted thickness, Cauchy coefficients and mean squared error (MSE) of the model fit obtained from the modelling of the optical data for a typical P4VP/ PS bilayer film.

MSE = 13.11		MSE = 15.55	
PS thickness	92.258 ± 0.0324	P4VP thickness	18.28 ± 0.12
A_n	1.5672 ± 0.0005	A_n	1.5064 ± 0.0034
B_n	0.00782 ± 0.00011	B_n	0.0125 ± 0.0005

2.3   Atomic Force Microscopy (AFM)

Atomic force microscopy (AFM) was introduced by Binning *et al.*[6] to analyse, at an atomic scale, the surface of non-conducting materials, to overcome the

limitation of scanning tunnelling microscopy (STM) on such surfaces. AFM utilises a sharp tipped (< 20 nm) stylus attached on the end of a cantilever to trace the topographic features of a surface at the nano scale.

AFM may be operated in *contact* mode, where the stylus is in continuous contact with the substrate, or in *tapping* mode, where the cantilever is driven by a piezoelectric element near its resonant frequency allowing only intermittent contact with the surface. The attractive and repulsive interactions between the stylus and the surface cause the cantilever to bend in contact mode, or experience a dampening of the amplitude of oscillation in tapping mode. The position of the tip in terms of bending deflection and oscillation as well as torsion is monitored optically by means of a laser beam focussed on the cantilever and reflected towards a four quadrant photodetector. A second piezoelectric element drives the sample in the xy plane in a raster pattern under the stylus, while the vertical motion (z distance) is controlled by a feedback mechanism (Figure 2.4).

In contact mode, the sample is raised or lowered based on the deviation of the cantilever deflection from a setpoint value. In tapping mode, the vertical position of the sample is adjusted to maintain the amplitude of oscillation near a set value. In both modes, the variation in the vertical position of the sample during scanning is plotted as a function of the horizontal position of the stylus to create topography images, where colour contrast is used to illustrate variations in height.
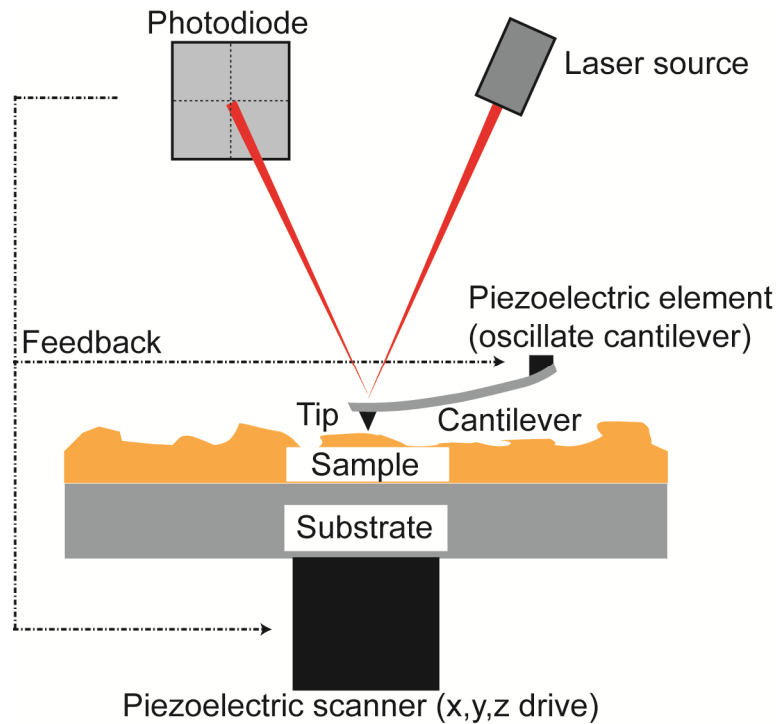
Figure 2.4: Schematic representation of the components and operation of an AFM. The sharp tip on the end of the spring cantilever probes the surface while oscillating at a set frequency near the resonance frequency of the cantilever. The piezoelectric scanner moves the sample in the XY plane and adjusts the Z distance in accordance to the feedback loop, guided by the laser signal reflected from the upper side of the cantilever. The feedback loop works to keep the tip-surface distance (or force) constant.

Contact mode imaging can result in pressures at the tip of up to a few GPa, which is on the order of the yield stress of glassy polymers, resulting in plastic deformation of the surface. The risks of damage and distortion to the sample surface, makes contact mode imaging unfavourable for polymeric and biological samples.[7] In tapping mode, the cantilever tip oscillates at the film surface rather than continuously contacting the surface, resulting in less abrasion for soft polymer surfaces. The trace of the surface is provided by digital analysis of a light signal reflected off the upper side of the cantilever into a photodetector, which provides feedback for the system to adjust the cantilever distance from the substrate. In addition to imaging the topography of a surface, the phase shift of the cantilever in tapping modes is dependent on the hardness of the material, which can provide information on the mechanical properties and composition of the surface.[8]

In this Thesis, AFM was used to measure the surface roughness of the copper substrate and subsequent polymer coatings prior to annealing (Chapter 6) as well as to image the patterned surfaces (Chapters 4 and 5). Feature distributions, sizes and

contact angles on the substrate were determined from the images and trace raw data. Measurements were performed with two instruments; a Bruker (Billerica MA, USA) Multimode VIII and an ASYLUM Research (Santa Barbara CA, USA) MFP 3D. The probes used had a nominal resonance frequency of 300 kHz and a force constant of 40 Nm^{-1} (Budget Sensors, Bulgaria; model Tap300Al-G). A representative micrograph of a polymer surface obtained by tapping mode AFM and the range of features that can be extrapolated from the data are presented in Figure 2.5.
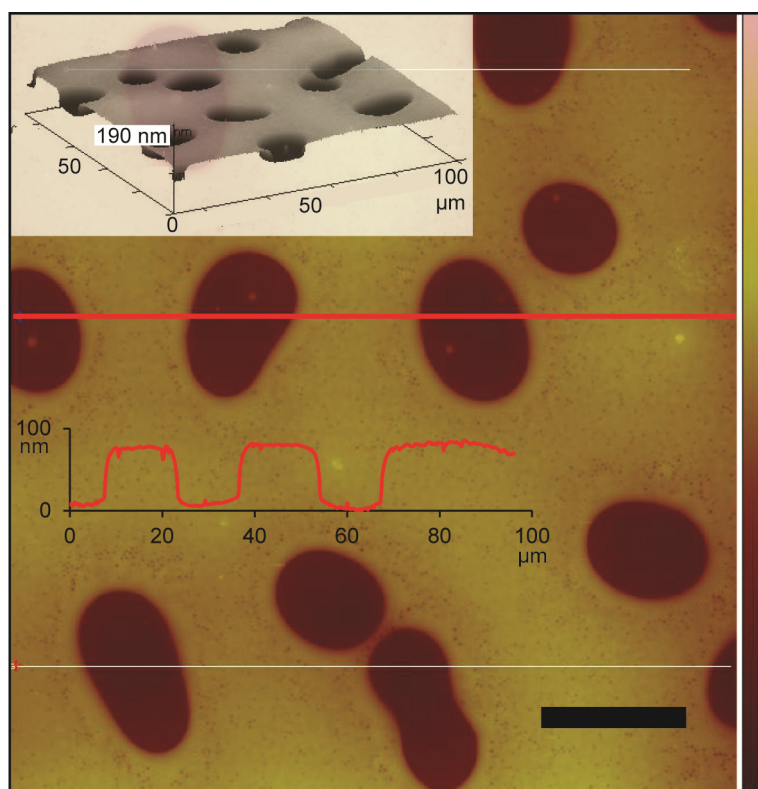
Figure 2.5: AFM micrograph of a P4VP/PS blend cast on a silicon substrate from chloroform showing feature heights. Insets: a three-dimensional surface rendering and a plot of the surface cross section (red line). Scale bar = 20 μm and height colour scale = 200 nm

2.4   Contact Angle Goniometry

Measurement of the contact angle of a liquid droplet on a surface provides a quantitative analysis of the wettability of a solid by the liquid of interest. The contact angle is defined as the internal angle, measured within the liquid drop, formed by a liquid at the three phase contact line where the liquid, solid and gas phases intersect.[9]

A static contact angle is measured when the three phase contact line is stationary; whereas a dynamic contact angle can be measured when the three phase contact line is advancing (droplet expansion) or receding (droplet contraction). The difference between the advancing and receding contact angles is the contact angle hysteresis, and is a measure of the surface roughness and heterogeneity of the surface.[10]

Goniometry is the science associated with the measurement of contact angles. A typical goniometer is composed of a light source, sample stage, lens and a camera. (Figure 2.6) In this work, a KSV (Helsinki, Finland) CAM200 was used to obtain information on the wetting behaviour of water on patterned polymer substrates, measuring static, advancing and receding contact angles.
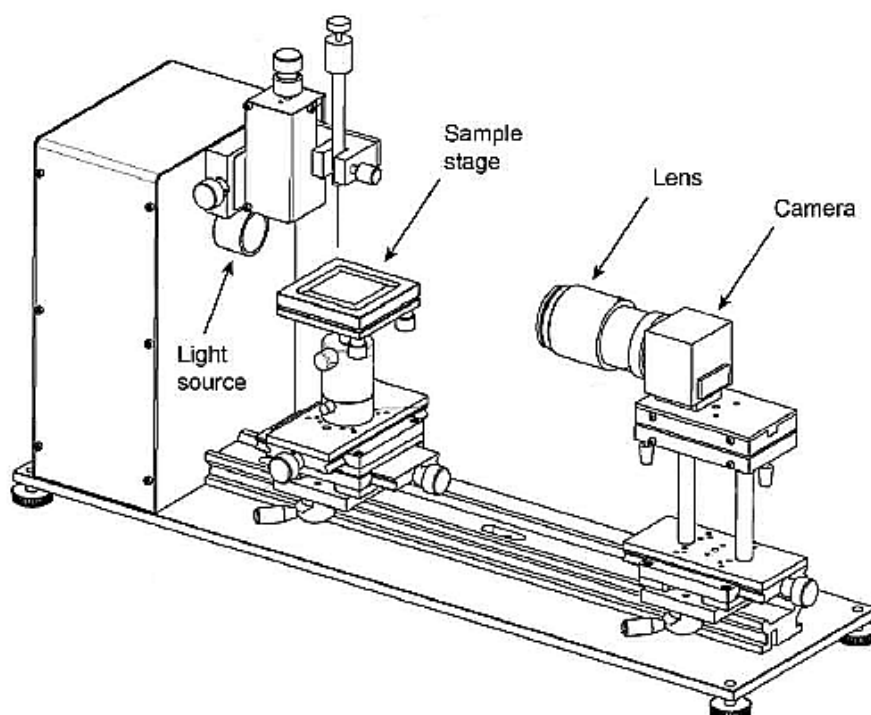
Figure 2.6: Schematic representation of a KSV CAM 200 contact angle goniometer.

In a typical experiment, a 5 µL water droplet was deposited on the surface with an automated syringe to measure the static contact angle. Advancing and receding contact angles were measured in two ways (Figure 2.7). In the volume addition-subtraction method: the contact angles were measured by increasing or decreasing, by 10 µL the volume of a 5 µL droplet at 0.5 µL s^{-1} and continuously capturing images of the expanding / shrinking droplet (50 frames, 1 fps). In the sliding-droplet

method, the substrate is tilted at 45° and the droplet volume is incrementally increased until roll-off occurs. The advancing contact angle is observed at the downhill side of the droplet and the receding contact angle at the uphill side immediately prior to roll off (Figure 1.3).
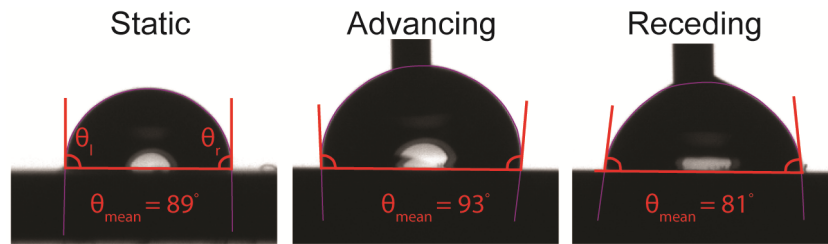
Figure 2.7: Profiles of water droplets on a polystyrene substrate fitted with the Young-Laplace equation to measure static, advancing and receding contact angles. Advancing and receding contact angles were measured using the volume addition / subtraction method.

The contact angle was determined by computer analysis (Attension Theta software) of the droplet profile as it intersects the baseline. by fitting the shape of the droplet with the Young-Laplace equation, which relates the pressure difference across an interface to the shape of the surface:

$$\Delta p = \gamma \left(\frac{1}{R_1} + \frac{1}{R_2} \right) \tag{2.8}$$

where Δp is the pressure difference across the fluid interface, γ is the surface tension at the liquid/gas interface, R_1 and R_2 are the principal radii of curvature. It is important for reproducibility that the tangent is determined as the gradient of the Young-Laplace equation at the point where the droplet intersects the baseline.

2.5   X-ray Reflectometry (XRR)

Reflectometry is a technique that uses the specular reflection of radiation to quantitatively provide information on the electron density profile, in a non-destructive manner, of materials with buried interfaces.[11] X-ray reflectometry, applied to polymer thin films, can allow for the determination of total film thickness,

interfacial roughness, mean densities and more. The length scales that can be measured with reflectometry range from 1 nm to approximately 300 nm, depending on the reflectometer.[12] In this Thesis, x-ray reflectometry was used to analyse the swelling behaviour of polystyrene films in the presence of solvent vapours (Chapter 4).

X-ray reflectivity (XRR) experiments for this Thesis were conducted by Dr Andrew Nelson at the Australian Nuclear Science and Technology Organisation (ANSTO) facilities located at Lucas Heights in Sydney NSW, (Panalytical X'Pert Pro, operating at 8.048 keV). A collimated beam was directed onto the sample at a given angle, θ. The specularly reflected intensity was measured as a function of Q, the momentum transfer vector:

$$Q = 4\pi sin\frac{\theta}{\lambda} \tag{2.9}$$

The reflectivity of a sample is the ratio of the reflected intensity to the direct beam intensity. In the Born approximation, where Q is much greater than $Q_{c,}$ the critical edge for the system, the reflectivity is related to the scattering length density profile, $\rho(z)$, by:

$$R(Q) \propto \frac{16\pi^2}{Q^2}\left|\int_{-\infty}^{\infty} \rho(z)e^{-iQz}dz\right|^2 \tag{2.10}$$

Since x-rays interact with the electron shell surrounding the nucleus the scattering length density is given by:

$$\rho = r_e\rho_e \tag{2.11}$$

with r_e = 2.813 x 10^{-6} nm (the classical electron radius) and ρ_e, the electron density.
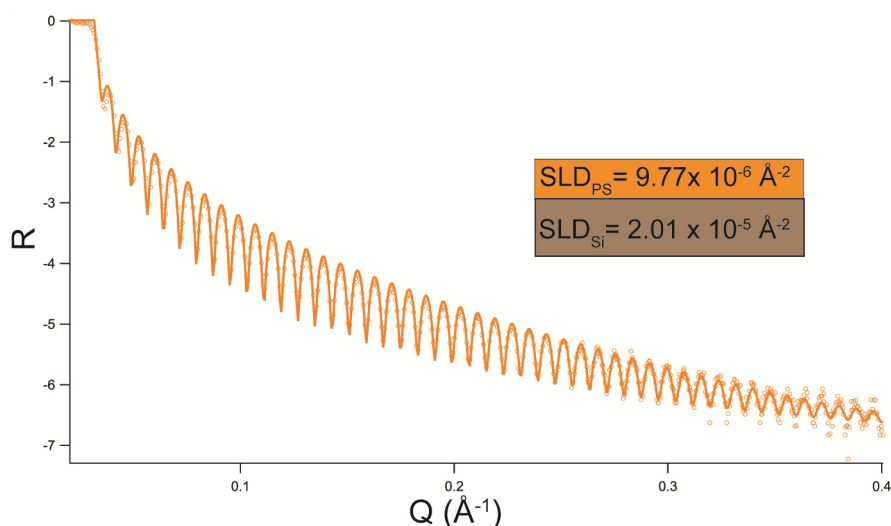
Figure 2.8: Representative x-ray reflectivity profile from a PS film on a silicon substrate. Experimental data (empty circles) and fits (lines) are shown. The profile shows Kiessing fringes due to the constructive and destructive interactions of waves scattered at the interfaces. The inset schematic indicates the scattering length densities (SLD) used in the model system.

In XRR, Q is varied by altering the incidence angle of the x-ray beam. Figure 2.8 shows a plot of an XRR profile for a polystyrene film on a silicon wafer, a typical system explored in this Thesis. The XRR data are fitted with a model with thickness and electron density as the variables. The profile shows Kiessing fringes, from the constructive and destructive interaction of waves scattered by the different layers, where the distance between the fringes is inversely proportional to the film thickness.

2.6   Solvent Vapour Annealing of Polymer Coatings

For the polymer dewetting experiments on flat substrates described in Chapters 4 - 6, a custom designed Teflon cell (Figure 2.9(a)) was manufactured to allow *in situ* observations of the progress of film dewetting by optical microscopy (Nikon, Melville NY, USA, model Eclipse LV150 with DS-F1 CCD) to be made. To induce dewetting, the polymer films, which were coated onto the flat substrates, were sealed within the cell, surrounded by a solvent bath and allowed to anneal in the saturated vapour environment. In addition to the Teflon cell, a custom brass cell (Figure 2.9(b)) was used to solvent vapour anneal and dewet polymer films coated onto copper tubes for the water collection experiments described in Chapter 6.
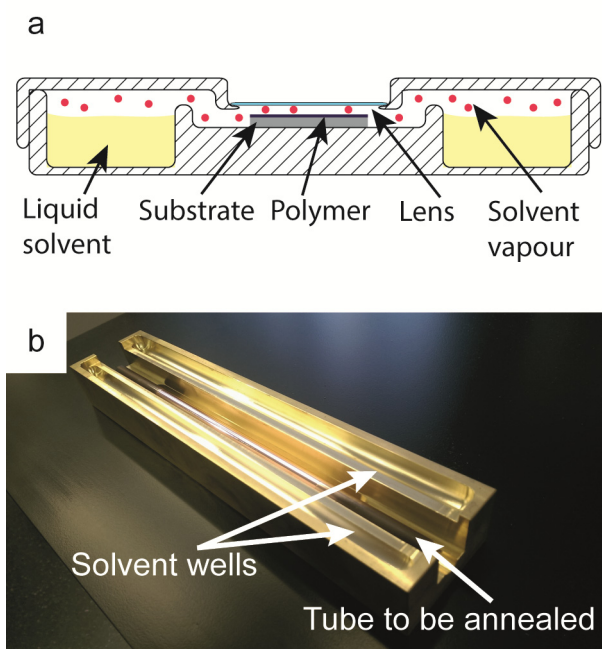
Figure 2.9: (a) Schematic diagram of the Teflon cell used to observe, *in situ*, the dewetting of polymer films by solvent vapors. The Teflon cell has a port open to the atmosphere to allow solvent injection and pressure equilibration (not shown). A microscope cover lens is situated above the sample for observation using optical microscopy. (b) Photograph of the custom made brass cell for solvent vapour annealing polymer-coated tubes.

2.7   Water Vapour Condensation Studies

Studying the condensation behaviour of water on polymer coatings requires control over sample temperature, relative humidity and ambient temperatures. A condensation chamber was designed to provide an appropriate degree of accuracy and allow the condensation behaviour of water vapour on the sample surface to be followed over time by optical microscopy (Figure 2.10). A thermoelectrically cooled Peltier plate (TE Technologies, MI, USA, CP-031 with TC48-20 controller) was set to have a surface temperature, measured by a T-type thermocouple and thermometer (Cole-Parmer IL, USA, model DigiSense 91100-40), which was offset 1 - 5 °C below the ambient temperature, and this temperature difference was   maintained within ±0.5 °C over the course of the experiment. The sample was placed on the cold plate within an enclosure where the humidity was controlled by manually adjusting the flow rates of a dry air stream and a wet air stream independently (Figure 2.10, yellow lines). The humidity and ambient temperature were measured by a Lutron (Instrument Choice, SA, Australia) model HT 305 sensor. The wet air stream was

provided by bubbling air through deionised water (Ω = 18 MOhm cm, Millipore, model Direct 5Q).
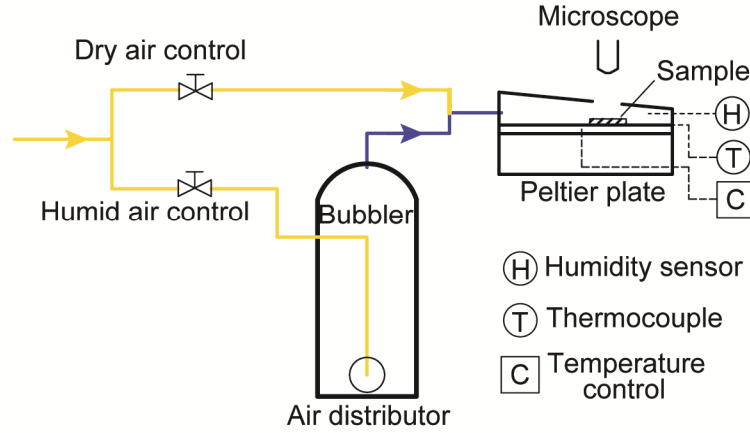
Figure 2.10: Schematic representation of a purpose-built chamber for condensation studies under the optical microscope. The flow of compressed air, provided for general lab use, was controlled by two needle valves to maintain the relative humidity at the desired value. An aerator ball was used to ensure the air stream could be sufficiently saturated with water. The Peltier plate was manually controlled to maintain the desired ambient - substrate temperature difference as there was no digital feedback between the temperature sensor and the controller.

The time-lapse images of the condensation behaviour on each surface were individually analysed using the microscope software (NIS Elements, Nikon, Melville NY, USA) to determine the area coverage of water accumulated on each surface. The volume of water V was calculated using a derived equation for the volume of a spherical cap, illustrated in Figure 2.11, relating V to the contact angle, θ, of the droplet on the surface, and the radius, R, of the droplet, which was calculated from the projected droplet surface area measured by image analysis:

$$V = \frac{1}{3}\pi R^3 (2 - 3\sin\alpha + \sin^3\alpha) \qquad (2.12)$$

With $\alpha = 90 - \theta$ and $R = a/\cos(90 - \theta)$ substituted into Equation 2.12, the droplet volume was calculated by:

$$V = \frac{1}{3}\pi \left(\frac{a}{\sin\theta}\right)^3 (2 - 3\cos\theta + \cos^3\theta) \qquad (2.13)$$

where the contact angle of the water droplets on the substrate were assumed to be the same as those obtained at the macro scale from contact angle goniometry measurements.
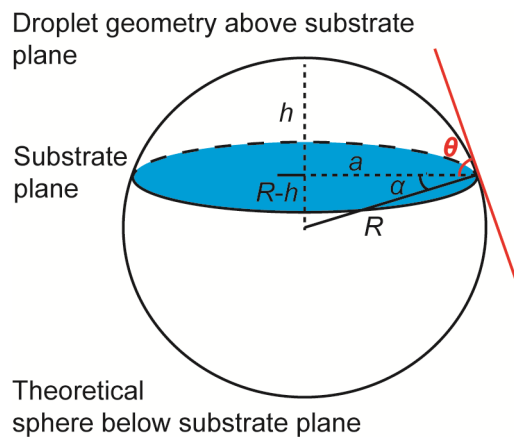
Figure 2.11: Schematic illustration of the spherical cap method for calculating droplet volume from information on the diameter and contact angle of a liquid droplet.

Water condensation studies provide insight into the *condensation* behaviour of water on materials with different surfaces properties. The amount of water that these surfaces will effectively *collect* requires a more sophisticated testing system. The construction and characterisation of a purpose-built apparatus for quantitative water collection measurements is described in Chapter 3.

2.8   References

1.   Lawrence, C. The mechanics of spin coating of polymer films. *Phys. Fluids* **1988,** *31* (10), 2786-2795.

2.   Grosso, D. How to exploit the full potential of the dip-coating process to better control film formation. *J. Mater. Chem.* **2011,** *21* (43), 17033-17038.

3.   Faustini, M.; Louis, B.; Albouy, P. A.; Kuemmel, M.; Grosso, D. Preparation of Sol− Gel Films by Dip-Coating in Extreme Conditions. *J. Phys. Chem. C* **2010,** *114* (17), 7637-7645.

4.   Jenkins, T. E. Multiple-angle-of-incidence ellipsometry. *J. Phys. D: Appl. Phys.* **1999,** *32* (9), R45.

5.   Langereis, E.; Heil, S. B. S.; Knoops, H. C. M.; Keuning, W.; van de Sanden, M. C. M.; Kessels, W. M. M. In situ spectroscopic ellipsometry as a versatile tool for studying atomic layer deposition. *J. Phys. D: Appl. Phys.* **2009,** *42* (7), 073001.

6.   Binnig, G.; Quate, C. F.; Gerber, C. Atomic Force Microscope. *Phys. Rev. Lett.* **1986,** *56* (9), 930-933.

7.   McConney, M. E.; Singamaneni, S.; Tsukruk, V. V. Probing soft matter with the atomic force microscopies: imaging and force spectroscopy. *Polym. Rev.* **2010,** *50* (3), 235-286.

8.   Magonov, S. N.; Reneker, D. H. Characterization of polymer surfaces with atomic force microscopy. *Annu. Rev. Mater. Sci.* **1997,** *27* (1), 175-222.

9.   de Gennes, P. G.; Brochard-Wyart, F.; Quéré, D. *Capillarity and wetting phenomena: drops, bubbles, pearls, waves*; Springer Science & Business Media, 2013.

10.   Berg, J. *Wettability*; Courier Corporation, 1993; Vol. 49.

11.   Bracco, G.; Holst, B. *Surface Science Techniques* [Online]; 1 ed; Springer: Berlin/Heidelberg, 2013.

12.   Stamm, M.; Reiter, G.; Kunz, K. The use of X-ray and neutron reflectometry for the investigation of polymeric thin films. *Physica B Condens. Matter* **1991,** *173* (1), 35-42.

CHAPTER 3

Design and Development of a Water

Collection Apparatus

3.1 Introduction

To date, experimental determination of the water collection efficiency of purpose-designed materials, where the surface chemistry and topography has been modified directly or by the application of surface coatings, is conducted in many labs by mounting the substrate onto a cooling module at the desired angle of inclination within a humid environment. A collection tray situated below the sample collects the water droplets that roll off the surface and after a period of time the mass of the collected water is noted (Figure 3.1). Typically the results are reported as the volume of water normalised against the projected surface area of the surface and the time frame of the experiment. In some cases a camera has been used to image the formation and roll-off of droplets from the substrate. [1-4] In other studies, the growth behaviour of water droplets on a modified or coated surface was observed and qualitatively analysed by microscopic techniques, similar to the method described in Section 2.7.[4-7] High resolution studies into the nucleation of water droplets are often conducted within an environmental scanning electron microscope (ESEM), where a humid environment is produced by altering the pressure within a sealed chamber with liquid water present.[6, 8, 9-10] Normally a combination of one or more these techniques have been used to characterise the performance of a water collection surface under condensation conditions.
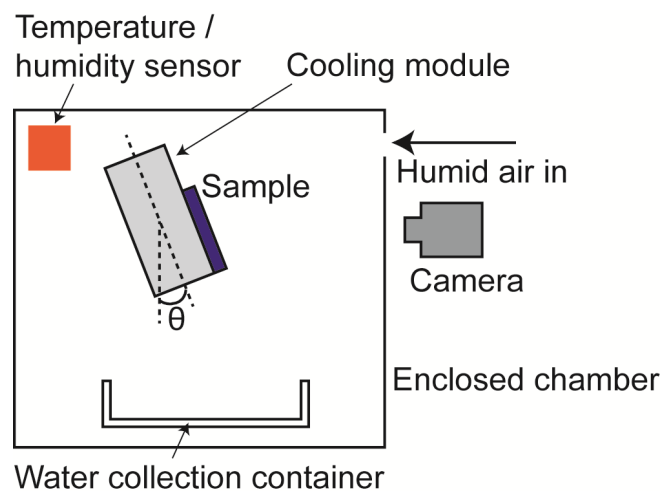

Figure 3.1: Representative schematic from the literature, of an experimental apparatus for quantifying the water collection properties of surface coatings.

As well as the quantifying water collection, the heat transfer properties of surfaces and coatings have also been explored, both theoretically[11-14] and experimentally.[10, 15-16] As an example, Cheng *et al.* designed a vapour chamber for heat transfer measurements which were used to deduce the heat transfer coefficient of their surfaces.[15] Their system was composed of an insulated sealed chamber, where the pressure could be controlled by a vacuum pump and saturation of the chamber atmosphere with water vapour was achieved by the evaporation of water from a temperature controlled reservoir within the chamber. The modified silicon sample was attached horizontally to a chiller plate mounted on the roof of the chamber with thermocouples embedded within the plate at precise intervals to deduce the heat flux through the material. The heat transfer coefficient was evaluated from the heat flux measurement along with the measurements from thermocouples in the vapour space, used to measure the vapour temperature, and thermocouples embedded in the underside of the silicon sample to measure the sample temperature.[15]

It has been shown that the experimental setup for water collection described above (Figure 3.1) is inadequate for accurate quantification of the performance of modified or coated surfaces. Firstly, as observed by Lee and co-workers, the water droplets that condense and roll off the surface have a tendency to pin to the bottom edge of the underlying substrate and form a "puddle".[1] This puddle leads to an increase in the thermal resistance of the surface and adversely affects its condensation performance. The deterioration of performance is exaggerated on hydrophilic surfaces due to the filmwise condensation mechanism of water droplets on these surfaces. The pinning behaviour and puddle growth, due to pinning effects at the edge of the substrate, is extrinsic to the manufactured surface properties of the material; therefore these pinning points must be removed.

Secondly, this experimental methodology tests the water collection of each coating sequentially. Sequential testing of each sample increases the experimental errors associated with the variables that influence water condensation. Ambient temperature, humidity and pressure, air flow rate and the substrate temperature all affect the rate at which water will condense on a sample. A setup where the samples could be tested simultaneously under the same conditions would reduce the random errors associated with each measurement and allow a direct comparison of the water collection efficiency of each surface to be made.

Finally, the small size of the testing samples, typically 10 x 10 mm^2, can lead to large systematic errors in condensation efficiency due to edge effects, surface defects, asymmetric substrate dimensions and coating quality. For example, a 10 x 10 mm^2 square silicon wafer with a polymer coating cast by spin coating will have a proportion of the surface suffering from coating defects due to edge effects, and these defects are expected to affect the collection performance.

In an effort to mitigate some of the problems mentioned above, a custom designed condensation system was constructed. Details of the design, setup, optimisation and operation of the system are described in the subsequent sections. In principle, the system design is similar to the apparatus used by Miljkovic *et al.* to measure the heat flux of a copper surface that was repetitively oxidised to produce a nanostructured surface with superhydrophobic properties.[10] In that work a tube, with the outer surface oxidised, was installed within a humidified chamber and cooled by flowing cold water through it. The log mean water to vapour temperature difference (ΔT_{LMTD}) was calculated by measuring the temperature of the cooling water at the tube inlet and outlet, as well as the vapour temperature (Equation 3.3). The heat flux could be determined from the increase in temperature, the flow rate and the specific heat capacity of the cooling fluid (Equation 3.1). The overall heat transfer coefficient of the surface could therefore be calculated from the ratio of the ΔT_{LMTD} and the heat flux (Equation 3.2). This design mitigates the first and third problems outlined above; however, as the set up only tests one sample at a time, strict control over the condensation parameters within the system was required to maintain identical environments between testing each surface.

3.2   Apparatus Design

For the purpose of this Thesis, a specialised condensation system was designed with the aim of minimising the sources of the experimental errors described in Section 3.1. The design was based on a traditional shell and tube heat exchange system,[17-20] composed of four tubes within a rectangular acrylic condensation chamber (Figure 3.2). The outer surface of the tubes was coated with polymer films, by dip coating, and treated by a solvent vapour annealing technique, developed in

this Thesis and presented in Chapters 4 and 5, to induce film dewetting, leading to the formation of polymer patterns on the tube surface. The prepared coatings were then exposed to a controlled humid environment within the condensation chamber, and the tubes subcooled below the ambient temperature allowing the condensation performance of the coatings could be compared simultaneously.
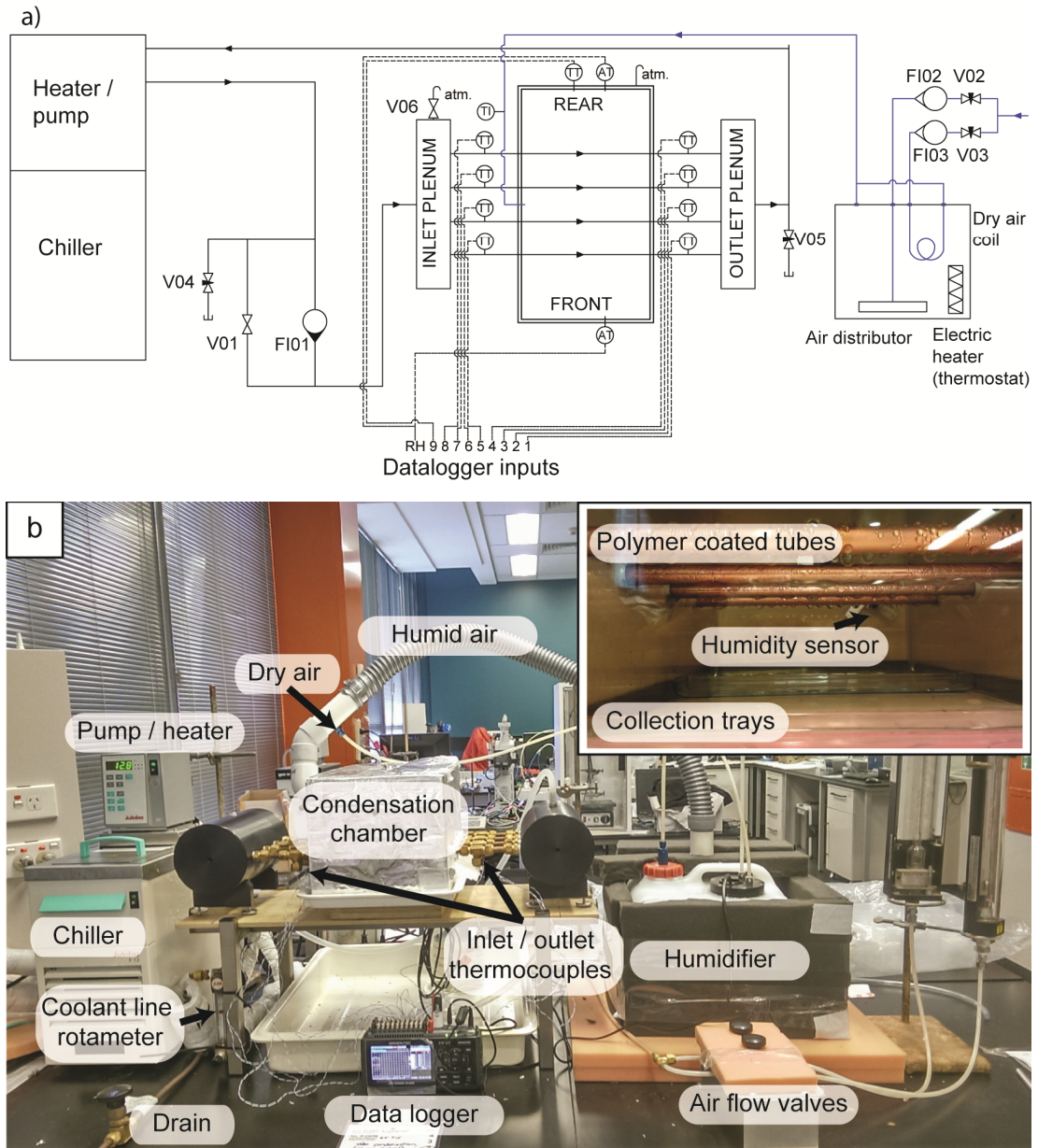
Figure 3.2: (a) Process and instrument diagram of the condenser system. The cooling system is drawn with solid black lines. Humidified and dry air streams are designated solid blue lines. Ambient temperature and coolant temperature are measured by sensors at several locations and the signal relayed to a data logger throughout the duration of the experiment (black, dashed lines). (b) Photograph of the complete condenser system with the main components labelled. Inset: Photograph of the inner layout of the condensation chamber, showing the tubes, humidity sensor and plastic containers for water collection.

3.2.1   Ambient environment control

Figure 3.2(b) is a photograph showing the complete condensation system. Centrally located is the condensation chamber within which the ambient temperature and relative humidity could be controlled.

Laboratory compressed air was humidified by bubbling through a 20 L reservoir filled with filtered water and a rectangular air stone (AquaOne, Australia) was used to distribute air bubbles, maximising the vapour-liquid interfacial area and increasing the water vapour content in the air stream. A thermostatically controlled heater (AquaOne, Australia, model 25 W) maintained the water temperature within the reservoir at approximately 29.1 ± 1.0 °C. A dry air stream intersected the main humidified air-line to provide accurate control over the relative humidity within the condensation chamber (Figure 3.2(a), blue solid line), which was measured by a humidity sensor within the chamber. The dry air temperature was equilibrated with temperature of the humid air stream by running through a length of tube coiled within the temperature controlled water reservoir.

To control the humidity, rotameters and needle valves on both the humid (FI02, V02 in Figure 3.2(a)) and dry (FI03, V03) air streams, prior to mixing, were used to indicate and control the relative flow of each stream. The flowmeters were not used to provide quantitative information regarding the flow rate of the streams as the relative flow rates of each line to achieve the desired humidity was strongly dependant on laboratory conditions. The ambient temperature within the condensation chamber was measured by T-type thermocouples (RS-Australia, model 158-907) located at the same vertical location as the condensing tubes; the temperature difference between the coated tubes and the ambient environment, ΔT, was assessed against this value.

The condensation chamber was isolated from convective and radiative heat transfer from the external laboratory environment by insulating with a fibre cladding and reflective aluminium foil with air flow allowed to exit the chamber through a 2 mm separation between the chamber and the base.

3.2.2   Tube preparation and polymer coating

Four copper tubes, 10 mm in diameter and 200 mm in length with a 150 mm length section machined to a depth of 0.5 mm to expose a smooth, clean surface in

the middle of the tube, were mounted within the condensation chamber as shown in in the inset photograph in Figure 3.2(b). The tubes were polished with metal polish then wiped clean with petroleum spirit and sonicated in ethanol prior to dipcoating a polymer film onto the outer surface (Figure 3.3). The parameters to achieve the desired polymer film thickness, as determined by spectroscopic ellipsometry, were first established by polymer films cast on two-dimensional copper substrates prepared by the same polishing and cleaning procedure due to the difficulties associated with measuring the thickness of films cast on three-dimensional curved substrates directly by spectroscopic ellipsometry. The colour of the polymer films, arising due to thin film interference, was the primary method by which the film thickness was deduced to be the same on both substrates.
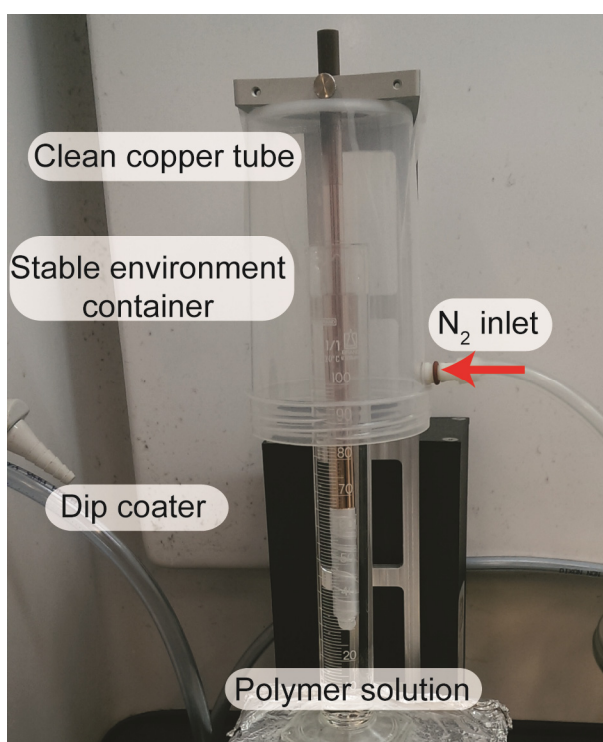
Figure 3.3: Setup for dip coating polymer films onto copper tubes. The tubes were capped to ensure only the outer surface was coated. They were also wrapped in Teflon tape from the bottom to the start of the machined section as it was unnecessary to coat this section. A container was used to control air flow around the tube and maintain a clean, inert environment.

Due to the unstable conditions within the fume hood in which the dip coating process was carried out, a plastic container was placed over the polymer vessel to minimise interference by the airflow during tube withdrawal and solvent

evaporation. Nitrogen gas flowed into the container during the dip coating process to ensure an inert, stable and clean environment and facilitate evaporation of the solvent. The copper tubes were plugged at the ends to ensure only the outer surface was coated. Any polymer material that was cast outside the machined length desired section was wiped off with an appropriate solvent, toluene for PS and ethanol for P4VP. The quality and uniformity of the coatings on the copper tubes, which was assessed based on colouration, was acceptable for the purposes of the water collection experiments described in Chapter 6. Minor variations in the film thickness did not significantly affect the size and distribution of the surface patterns produced by dewetting, which were observed by optical microscopy and compared against the patterns prepared on copper sheets under the same conditions with a known initial polymer film thickness.

The optimal dip coating parameters to produce homogenous polymer coatings on two dimensional copper and silicon substrates were determined by Mr Kieran Geraghty, a summer scholar under my supervision. These parameters were used to produce the films discussed in Chapter 6 and are shown below in Table 3.1. A single solution of 2 %wt. polystyrene with $M_w = 350\,000$ g mol^{-1} in toluene (PS350k) was used, while solutions of increasing concentration of poly(4vinylpyridine) with $M_w = 60\,000$ g mol^{-1} (P4VP60k) in ethanol were used for bilayer preparation.

Table 3.1: Film thickness of polymer coatings applied onto two-dimensional copper sheets.

Polymer solution (substrate)	Extraction speed (mm min^{-1})	Film thickness (nm)
PS350k 2 %wt. in toluene (copper)	120	110 ± 2
P4VP60k 0.5 %wt. in ethanol (PS)	25	5 ± 1
P4VP60k 3 %wt. in ethanol (PS)	50	87 ± 5
P4VP60k 7.5 %wt. in ethanol (PS)	200	826 ± 6

3.2.3   Cooling system

A cooling system (Figure 3.2(a), black solid lines) was designed to control the temperature of the coated copper tubes within the condensation chamber. Ethanol was used as the cooling fluid due to its low specific heat capacity, and was chilled and circulated around the system by a combined pump-heater (Julabo, Germany, model F12-MP). Two plenum chambers on the inlet and outlet sides of the

condensation chamber were designed to equalise the fluid pressure and evenly distribute the flow between the four tubes which were connected between them. T-type thermocouples were inserted into the tubes at tee junctions on the inlet and outlet sides of each tube (Figure 3.2(b)).

The cooling circuit was designed to operate in two modes. In *open mode* the maximum flow rate of the pump could be achieved (10 L min^{-1}) by opening a bypass valve (Figure 3.4, V01). In this mode, the temperature drop of the ethanol within the tubes at the outlet of the condensation chamber could be reduced to within 0.2 °C, on average, of the inlet temperature across all tubes due to the high cooling fluid flow rate. In *closed mode*, the coolant flow rate could be measured and moderated. In the controlled mode, the coolant flow is diverted through a rotameter (ABB Ltd. Zurich, Switzerland, model A6141 Purgemaster) with a needle valve to control and monitor flow rates (Figure 3.4, FI01) up to 25 L h^{-1}.
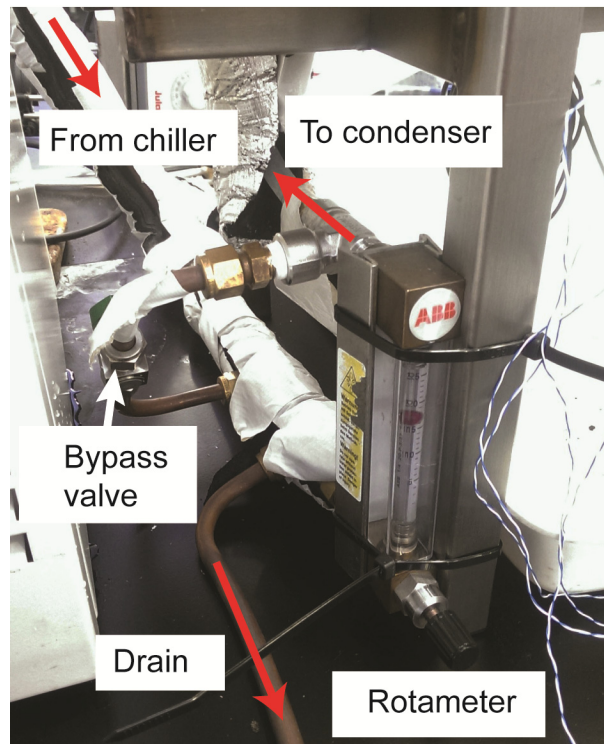

Figure 3.4: Cooling fluid inlet stream showing the flow indicator / controller and the bypass valve for 'open' flow mode.

In this configuration, the apparatus could be used to measure the heat flux of each surface coating during water condensation and collection. A low cooling fluid

flow rate is required for heat transfer experiments in order to maximise the temperature difference across each tube due to heat gain by the cooling fluid as calculated by Equation 3.1, providing a more accurate measurement of condensation heat transfer.

$$Q = \dot{m}c_p\Delta T \tag{3.1}$$

where Q is the heat flux, $\dot{m}$ is the mass flow rate of the cooling flow, c_p the specific heat capacity of the cooling fluid and ΔT the temperature gradient across each tube. With knowledge of the heat flux (Equation 3.1) and the ΔT_{LMTD} (Equation 3.3) of each tube, the heat transfer coefficient h, of each coating could be calculated by:

$$h = \frac{Q}{\Delta T_{LMTD}} \tag{3.2}$$

$$\Delta T_{LMTD} = \frac{\Delta T_A - \Delta T_B}{ln\left(\frac{\Delta T_A}{\Delta T_B}\right)} \tag{3.3}$$

where ΔT_A is the temperature difference between the air and cooling fluid inlets and ΔT_B, the temperature difference between air and cooling fluid outlets respectively.

3.2.4   Data logging

A 10 channel data logger (Graphtec, Japan, model midi Logger GL220) was used to record the inlet and outlet temperature of the cooling fluid across each tube as well as the ambient air temperature using T-type thermocouples (measurement error ± 0.5 °C), and the relative humidity of the environment within the chamber (probe model B-530, measurement error ± 3%RH) during each experimental run. The ratio of humid air to dry air was manually adjusted in response to the relative humidity measurement within the chamber. Due to changing lab conditions, it was also necessary to monitor and adjust the coolant temperature throughout the experiment to maintain the desired temperature differential between the tubes and the humidified air stream, which is discussed in Section 3.3.2.

The amount of water collected, during steady state operation, was the main measurement of interest. This variable was measured by weighing the water collected over the course of a single experiment as it rolled off the tubes and into the plastic containers located below each tube. These containers were weighed dry, before each run and then a second time following droplet shedding from all tubes, which was considered to be the starting point of steady state condensation. The mass of water collected was then weighed multiple times over the course of the experiment, typically lasting 6 h. The amount of water collected by each coating was calculated and converted into a collection efficiency value for each coating with units of mL m^{-2} h^{-1}.

3.3   Design Optimisation

3.3.1   Coolant flow problems and plenum chamber redesign

Initial trial runs of the cooling system resulted in anomalous temperature measurements as shown in Figure 3.5(d). While the spread in the temperature gradients between the inlets and outlets and the inlet cooling fluid temperatures between the four tubes was 0.3 °C, on average, there was a clear bias in the inlet temperatures, as Tube 4 was consistently warmer than the remaining tubes. Secondly, the temperature gradient within the tubes was also consistently higher in Tube 2 and the lowest in Tube 3.   Following the addition of thermal insulation to the original brass chambers (Figure 3.5(a), OD 30, ID 16) and a thorough investigation of other causative factors, the problem was attributed to flow irregularities of the cooling fluid within the inlet and outlet plenum chambers.

It was hypothesised that due to the small bore size of the brass plenum chambers, unequal flow distribution resulted in uneven cooling fluid flow between the four tubes. Furthermore, the configuration of the inlet and outlet ports to the plenum chambers was also expected to affect irregularities in the fluid flow and lastly, the high thermal conductivity of the brass was attributed to the presence of thermal gradients along the length of the chambers. A schematic representation of the predicted fluid flow behaviour in the brass plenum chamber is presented in Figure 3.5(c).

To rectify this issue, larger bore plenum chambers were designed and manufactured from acetal plastic (Figure 3.5(b), OD 150, ID 130). To ensure even pressurisation of both chambers, the inlet port to the inlet plenum chamber was shifted to the bottom of the chamber and the outlet chamber outlet was moved to the top. A 66 fold increase in the internal volume of the chambers, coupled with the rearrangement of the inlet and outlet ports, was found to improve the flow of the coolant between the four tubes and resulted in a reduction in the deviation of the temperature gradient between the four tubes. Furthermore, the thicker wall and thermally insulating property of acetal minimised the heat gain of the cooling fluid due to the external laboratory conditions.
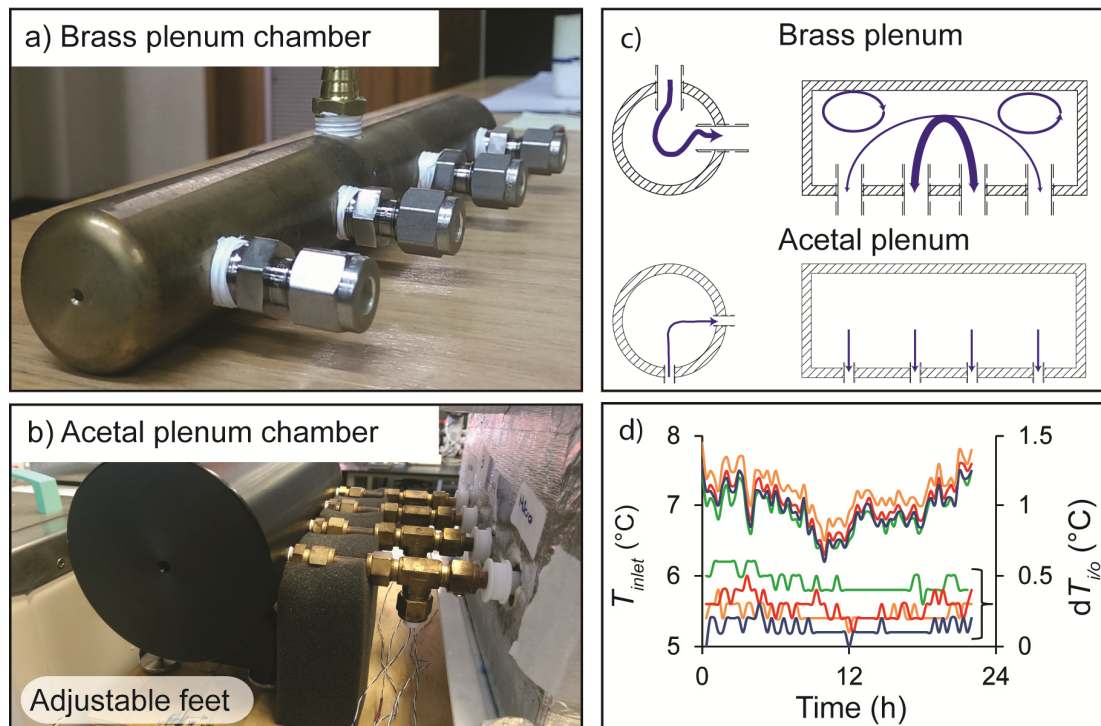
Figure 3.5: (a) Photographs of brass (OD 30, ID 60) and (b) acetal (OD 160 ID 130) plenum chambers. For the purpose of scale, the tube fittings on both chambers are the same size. (c) Schematic drawings of the predicted turbulent, uneven flow (depicted by arrow width) in the smaller bore brass chamber compared with laminar, even flow in the larger acetal chamber. (d) Plot of the inlet temperatures (T_{inlet}) and the temperature difference ($dT_{i/o}$) between the inlet and outlet for tube 1 (red), tube 2 (green), tube 3 (blue) and tube 4 (orange) in the condensation chamber.

3.3.2   Mixing humid and dry air

Control over the ambient humidity within the condensation chamber was important for the purpose of reporting the water harvesting performance of the

surface coatings. To provide sufficient control over the humidity levels, two air streams where used, one flowing through a water reservoir to humidify and the second, a dry air stream. Both streams were independently controlled by needle valves V02 and V03 respectively. Rotameter FI02, with a maximum flow rate of 160 L min^{-1}, was used to monitor the flow rate of the humid air stream and provide feedback for coarse adjustment of the relative humidity within the condensation chamber. Meanwhile the rotameter on the dry air stream, FI03, with a maximum flow rate of 30 L min^{-1}, was used to provide feedback for fine control over the relative humidity. With this design, humidity levels in the chamber could be maintained within 2 %RH of the average value, which is within the error of the measurement of the humidity sensor ($\pm$ 3 %RH).
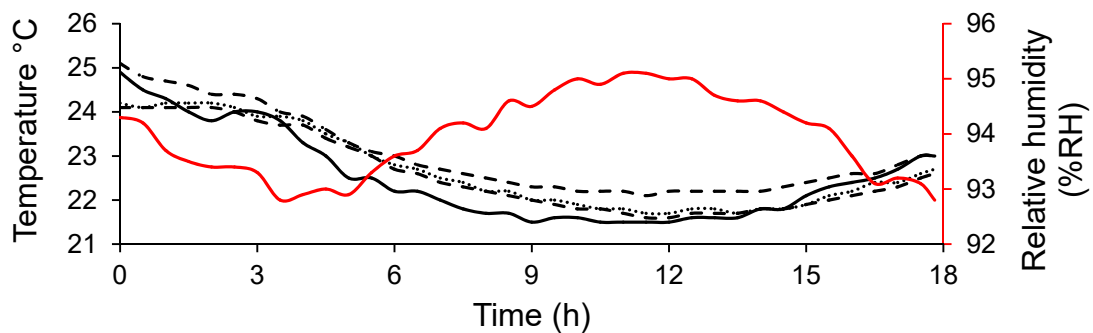
Figure 3.6: Effect of laboratory temperature (black, solid) on the front (black, dashed) and rear (black, dotted) internal temperatures of the condensation chamber, the humid air stream (black, dash dot) and the relative humidity within the chamber (red, solid). Experiment was initiated at 16:00 with a sampling rate of 2 measurements per minute. A sampling rate of 2 measurements per hour is presented in the plot.

To show the effects of a change in lab conditions on the insulated chamber, the stability of the humidity levels and temperatures within the condensation chamber were studied over an 18 h period after initially setting the humidity levels at 94%RH (Figure 3.6). During this experiment, the lab temperature decreased by 3.5 °C, which led to a 2 °C decrease in the internal temperature of the condensation chamber. The ambient temperature was monitored at the front and the rear of the condensation chamber with T-type thermocouples and the temperature at the two locations was found to be within $\pm$ 0.1 °C. The level of variability demonstrated in this experiment was deemed acceptable for the purpose of the water collection experiments described

in Chapter 6 because a simultaneous and direct comparison across 4 samples within the condensation chamber was possible over long periods.

3.3.3   Thermocouple connections for the cooling system

It was important to the design of the system to be able to monitor both the inlet temperature of the cooling fluid within the tubes and the temperature gradient between the inlets and outlets of the tubes. The size and location of the fittings was dependant on spatial restrictions imposed by the small diameter of the tubes and the dimensions of the condensation chamber. Therefore a tee junction fitting was used and a special Teflon holder machined to position the weld bead of the thermocouples precisely in the centre of the sample tubes to provide an accurate measurement of the coolant temperature (Figure 3.7). Permanent adhesive (Henkel Pty Ltd, 3137 Vic, Australia, model Loctite gasket maker 596) was used to bond the thermocouple wires within the Teflon holder. The thermocouples emerged vertically downwards from the condenser tubes to ensure that air bubbles were not trapped around the Teflon holder, which would affect the reliability of the temperature measurements.

Figure 3.7: Photograph of the components of the thermocouple housing and the Teflon thermocouple holder.

3.4   Apparatus Commissioning

3.4.1   Coolant filling

The cooling circuit required approximately 4 L of ethanol to sufficiently fill the whole system. Drain valves V04 and V05 were closed and the four sample tubes within the condensation chamber were fitted between the plenum chambers with sufficient tightness that the cooling fluid did not leak. It was important not to over tighten the tube fittings on the condenser tubes as the Swagelok fittings needed to be removed to interchange the tubes. Filling was done via the reservoir in the chiller with the pump running to circulate the cooling fluid around the system. Care was taken to maintain a sufficient level of fluid in the chiller reservoir, otherwise a low level alarm sounded and the pump turned off. The bypass valve, V01, was open to allow the system to fill at the maximum flow rate of the pump. In order to ensure the inlet plenum chamber was filled with coolant, without a headspace of air, the bleed screw located on top of the inlet chamber, was loosened to allow air to escape. This screw was tightened once the cooling fluid emerged from the top of the chamber.

3.4.2   Interchanging condenser tubes

The four sample tubes were designed to be removable to facilitate the need to test different coatings as well as to refresh the coatings between experimental runs. The tubes were designed to be connected into the tube fitting on the thermocouple tee junctions sufficiently tightly to achieve a liquid seal but not enough to swage the tubes, in order to enable the removal of the fittings to dip coat the tubes. The tubes were centrally located within the holes in the condensation chamber by purpose made, tapered Teflon sealing grommets. The grommets were asymmetric lengthwise, extending within the chamber to cover the redundant section of tube (Figure 3.8). The externally tapered shape of the grommet resulted in a tight seal with the condensation chamber and squeezed the grommet around the tube.
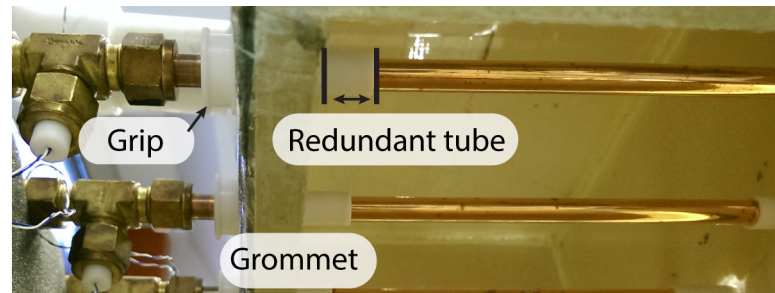
Figure 3.8: Grommets for aligning and sealing the sample tubes within their location in the condensation chamber.

In order to remove and replace the tubes, the cooling system was first drained as described below in Section 3.4.4. All sensors that were attached to the condensation chamber were removed and the tubes were unscrewed from the tee fittings on the inlet and outlet chambers. The outlet plenum chamber was subsequently removed allowing sufficient clearance to withdraw the tubes. The tubes were then removed from the thermocouple junctions on the inlet side to the chamber. Pulling outwards loosened the tapered grommets and the entire chamber could be inclined to provide internal access. The grommets could be removed and the tubes were uninstalled sequentially by drawing towards the outlet side carefully. The most practical method was to hold the outside of the tube on the outlet side and the redundant section of the tube within the chamber to withdraw the tube without making contact with the acrylic chamber. Installation of the tubes proceeded in the reverse manner and care was required to ensure the coatings were not damaged against the chamber walls. Prior to an experimental run it was important for the tubes and chamber to be horizontally level, to ensure fluid flow was even across the tubes.

3.4.3   Apparatus characterisation

To quantify and compare the water collection efficiency of different surface coatings on the condenser tubes it was necessary to characterise the natural variability in water collection rate between the four tubes that arose due to irregularities in the cooling fluid flow in the tubes and the flow of humid air within the condensation chamber as well as external laboratory temperature gradients across the four tubes at the inlets and outlets to the condensation chamber.

Table 3.2: Systematic error characterisation for water collection apparatus based on the deviation of the amount of water collected by the four, polystyrene coated, tubes as a function of ambient humidity and the temperature difference, ΔT, between the cooling fluid and the ambient. The error in the relative humidity measurements ± 3 %RH and in the temperature measurements ± 0.5 °C.

Relative humidity (%RH)	ΔT (°C)	Measurement error (mL h^{-1})
95	10.1	± 0.08
96	6.1	± 0.06
95	5.1	± 0.05
95	2.7	± 0.01

The variability in the rate of water collection was measured between the four tubes coated with a 110 nm thick polystyrene coating. The humidity within the chamber was maintained at 95 ± 3 %RH and the temperature difference between the cooling fluid inlet temperature and the ambient temperature ΔT, was varied between 2.7 – 10.1 °C with multiple water collection measurements taken during steady state condensation at each value of ΔT. The magnitude of the systematic error for each RH and ΔT combination was calculated and tabulated with units of mL h^{-1} (Table 3.2).

3.4.4   Draining the system

Complete or partial draining of the system was required for interchanging the sample tubes within the condensation chamber, cleaning the cooling circuit, interchanging the cooling fluid or any other modification to the cooling circuit that would result in the cooling fluid leaking from the system.

There were two drain valves; V04 (Figure 3.9(a)) and V05 (Figure 3.9(b)) built into the cooling circuit for the purpose of draining the system. The correct procedure for draining involved unscrewing the bleed screw on the inlet plenum chamber, followed be clamping the inlet tube from the chiller, and opening the bypass valve V01. One or both of the drain valves could then be opened and drained into an appropriate container and the coolant could be recycled into the system.
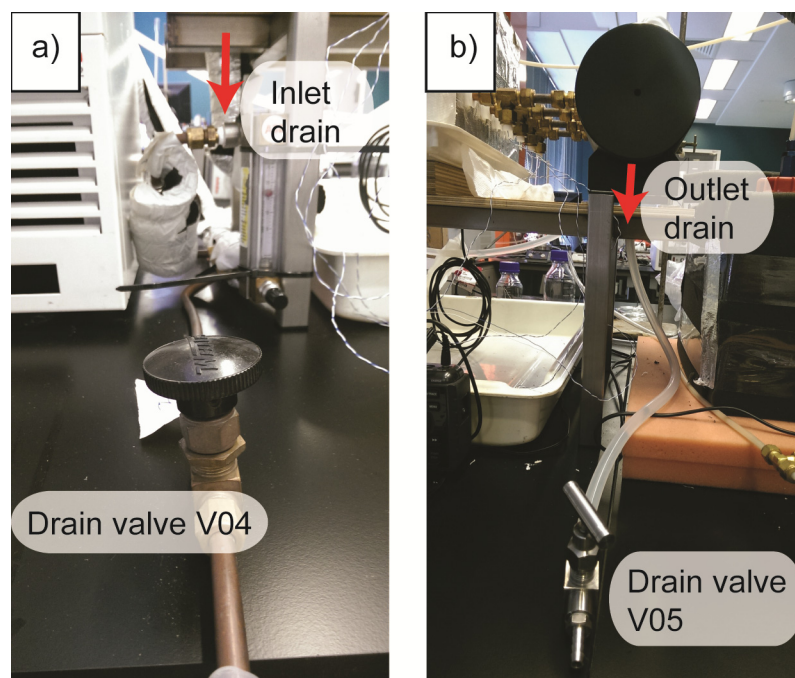
Figure 3.9: Locations of (a) the inlet chamber drain valve V04 and (b) the outlet chamber drain valve V05.

3.4.5 Cooling fluid safety

The safety of the operator has been of foremost consideration during the design and manufacture of this condensation system. The procedures outlined above, if followed correctly, ensured that the system was prepared and operated in a safe and reliable manner.

As the cooling fluid is ethanol, a flammable and volatile solvent, care was taken when filling and draining the cooling circuit to avoid spills, and any spills were dealt with appropriately. A tray is located below the condensation chamber as a precaution against any spills from the plenum chambers and tube fittings. The outlet valves V05 and V04 were tightly closed during normal operation to avoid an undetectable slow leak. While filling the circuit with cooling fluid, a small leak from the bleed valve was expected but was wiped with absorbent material immediately and care was taken to ensure the bleed screw was not completely removed from the chamber. Any time that the cooling system contained ethanol, the chiller need to continue to run. This chiller model maintained the reservoir temperature at -20 °C, which reduced the ethanol vapour pressure around the system to 133 Pa. The entire system was kept below the boiling point of ethanol, 78 °C, at all times to prevent two phase flow and pressure build up within the tubes and chambers.

3.5   Continuing Issues and Future Work

Water condensation is a very sensitive process and the error associated with external environmental conditions could result in large uncertainties when considering the water collection efficiency of different surface coatings. Great care has been taken to ensure uniform humidity and temperature conditions within the condensation chamber to minimise the uncertainty associated with the water collection measurement. However extrinsic conditions had a significant effect on the environment within the condensation chamber and these are discussed below. Some remedies are suggested to enhance the reliability and accuracy of future measurements.

Figure 3.6 illustrates the effect of laboratory conditions on the internal conditions of the condensation chamber during an 18 h cycle. Due to the observed lag in time between the decrease in temperature in the lab and the subsequent temperature decrease in condensation chamber temperature, the insulation of the chamber was considered satisfactory and therefore any future remedy of this effect will require accurate control over the laboratory environment or the provision of another location to set up the apparatus with temperature control.

As mentioned in Section 3.3.1, individual flow meters were not installed on the four sample tubes due to the high cost and heat transfer experiments were not conducted in the work presented in this Thesis. For the purpose of flow control and measurement, a single rotameter (FI01) was placed at the inlet to the condensation chamber and the measurement was used to infer the flow rate through each sample tube. The assumptions associated with this method were that the pressure within the plenum chambers was stable and the cooling fluid flow evenly distributed across all four tubes. The assumption of even flow was validated by the low variation in the measured temperature gradients of the cooling fluid between the four condensation tubes, following the redesign of the plenum chambers.

The issues discussed above highlight the difficulty of providing a quantitative comparison of the performance of water collection surfaces in this field. The custom apparatus described in this chapter addresses many of the problems identified with previous works; however it has also raised new issues, including the need for high-resolution sensors for temperature and humidity measurements due to the sensitivity

of water collection to environmental and surface conditions. For the purpose of atmospheric water collection, this apparatus provides control over conditions that replicate real world scenarios. In comparison to works that rely on the change of pressure within a sealed chamber to alter humidity, the current design incorporates the effects of the presence of non-condensable gases and realistic water vapour concentrations. As a result, the materials tested in this set up can be directly scaled up for application in atmospheric water harvesting.

Regarding the practical aspects of the design, the current method of installing and removing the tubes requires manual dexterity and mental concentration to avoid damaging the surface coatings by abrasion against the condensation chamber walls. To remove this risk, any future design should incorporate an installation mechanism internally contained within the condensation chamber to enable the condensation tubes to 'snap' in and out of the cooling circuit.

3.6   Acknowledgments

3.7   References

1.   Lee, A.; Moon, M. W.; Lim, H.; Kim, W. D.; Kim, H. Y. Water harvest via dewing. *Langmuir* **2012,** *28* (27), 10183-10191.

2.   Garrod, R.; Harris, L.; Schofield, W.; McGettrick, J.; Ward, L.; Teare, D.; Badyal, J. Mimicking a stenocara beetle's back for microcondensation using plasmachemical patterned superhydrophobic-superhydrophilic surfaces. *Langmuir* **2007,** *23* (2), 689-693.

3.   White, B.; Sarkar, A.; Kietzig, A. M. Fog-harvesting inspired by the Stenocara beetle–an analysis of drop collection and removal from biomimetic samples with wetting contrast. *Appl. Surf. Sci.* (0).

4.   Zhang, L.; Wu, J.; Hedhili, M. N.; Yang, X.; Wang, P. Inkjet printing for direct micropatterning of a superhydrophobic surface: toward biomimetic fog harvesting surfaces. *J. Mater. Chem. A* **2015,** *3* (6), 2844-2852.

5.   Yu, T. S.; Park, J.; Lim, H.; Breuer, K. S. Fog Deposition and Accumulation on Smooth and Textured Hydrophobic Surfaces. *Langmuir* **2012,** *28* (35), 12771-12778.

6.   Hou, Y.; Yu, M.; Chen, X.; Wang, Z.; Yao, S. Recurrent Filmwise and Dropwise Condensation on a Beetle Mimetic Surface. *ACS Nano* **2014,** *9* (1), 71-81.

7.   Thickett, S. C.; Neto, C.; Harris, A. T. Biomimetic surface coatings for atmospheric water capture prepared by dewetting of polymer films. *Adv. Mater.* **2011,** *23* (32), 3718-3722.

8.   Chen, X.; Wu, J.; Ma, R.; Hua, M.; Koratkar, N.; Yao, S.; Wang, Z. Nanograssed micropyramidal architectures for continuous dropwise condensation. *Adv. Funct. Mater.* **2011,** *21* (24), 4617-4623.

9.   Nosonovsky, M.; Bhushan, B. Biomimetic superhydrophobic surfaces: multiscale approach. *Nano Lett.* **2007,** *7* (9), 2633-2637.

10.   Miljkovic, N.; Enright, R.; Nam, Y.; Lopez, K.; Dou, N.; Sack, J.; Wang, E. N. Jumping-Droplet-Enhanced Condensation on Scalable Superhydrophobic Nanostructured Surfaces. *Nano Lett.* **2012,** *13* (1), 179-187.

11.   Miljkovic, N.; Enright, R.; Wang, E. N. Effect of Droplet Morphology on Growth Dynamics and Heat Transfer during Condensation on Superhydrophobic Nanostructured Surfaces. *ACS Nano* **2012,** *6* (2), 1776-1785.

12.   Kim, S.; Kim, K. J. Dropwise condensation modeling suitable for superhydrophobic surfaces. *J. Heat Transfer* **2011,** *133* (8).

13.   Ghosh, A.; Beaini, S.; Zhang, B. J.; Ganguly, R.; Megaridis, C. M. Enhancing Dropwise Condensation through Bioinspired Wettability Patterning. *Langmuir* **2014**.

14.   Bansal, G. D.; Khandekar, S.; Muralidhar, K. Measurement of heat transfer during drop-wise condensation of water on polyethylene. *Nanosc. Microsc. Therm.* **2009,** *13* (3), 184-201.

15.   Cheng, J.; Vandadi, A.; Chen, C. L. Condensation heat transfer on two-tier superhydrophobic surfaces. *Appl. Phys. Lett.* **2012,** *101* (13), 131909-131909-4.

16.   Xiao, R.; Miljkovic, N.; Enright, R.; Wang, E. N. Immersion Condensation on Oil-Infused Heterogeneous Surfaces for Enhanced Heat Transfer. *Sci. Rep.* **2013,** *3.*

17.   Nitsche, M.; Gbadamosi, R. O. *Heat Exchanger Design Guide: A Practical Guide for Planning, Selecting and Designing of Shell and Tube Exchangers*; Butterworth-Heinemann, 2015.

18.   Stewart, M.; Lewis, O. T. *Heat exchanger equipment field manual: common operating problems and practical solutions*; Gulf Professional Publishing, 2012.

19.   Thulukkanam, K. *Heat exchanger design handbook*; CRC Press, 2013.

20.   Hesselgreaves, J. E. *Compact heat exchangers: selection, design and operation*; Gulf Professional Publishing, 2001.

CHAPTER 4

Dewetting Polystyrene Films with Toluene-Ethanol Vapour

4.1   Introduction

The dewetting of thin polymer films from a solid substrate has been studied extensively over the past three decades,[1-7] and has interesting applications in surface patterning.[8-9] The Neto group at the School of Chemistry has demonstrated applications of polymer dewetted patterns in protein and cell patterning[10-12] and in atmospheric water capture.[13]

In most unstable and metastable polymer liquid films (thickness < 100 nm) dewetting occurs by nucleation of holes at random locations, whereby the substrate is exposed and the polymer removed accumulates in a rim around each hole.[14] With time the holes grow in diameter, the rims of neighboring holes coalesce into liquid cylinders, and finally into isolated droplets of the polymer on the substrate. Dewetted holes have often circular shape and regular rims, but, in cases where interfacial slip is strong, undulations of the rim shape lead to fingering and droplet shedding.[7, 15-21] One of the main causes of dewetting is the unfavorable interfacial interactions of the liquid film at the solid surface. For example, one proposed form of the interfacial potential $\Phi(h)$, Equation 1.7, includes the effects of short-range forces (first term) and long-range van der Waals forces (two following terms) for polystyrene films of thickness h on top of silicon substrates coated with silicon oxide of thickness d, with Hamaker constants A_{Si} (negative) and A_{SiO} (positive).[14] In the case of a thick oxide layer (thickness d of 200 nm), this expression correctly predicts a van der Waals attraction which promotes film dewetting.

When polar interactions are important, i.e. when either the film or the fluid environment in which it is immersed are polar, polar attractions also contribute to increasing the driving force for film dewetting.[22-23] The polar contribution often takes the form $S_p \, exp\left(-\frac{h}{l}\right)$, where S_p is the polar component of spreading coefficient, and l is a correlation length.

In the past 10 years there has been increased understanding of another important driving force for dewetting, the chain equilibration process in thin films.[24-31] Spin-coating induces strongly out-of-equilibrium conformations of the chains and low entanglement density due to the fast evaporation of the solvent. This leads to residual elastic stresses that relax upon annealing, and drastically affect dewetting rate,[27-29] entanglement density and viscosity,[32] and thermal expansion.[25, 33-35]

Although annealing of polymer films by exposure to solvent vapours of different quality has been explored before,[33-40] there has not been a systematic study of how solvent quality affects dewetting, and in particular the elastic forces within the polymer film.

In this Chapter, the effect of gradually changing the quality of the solvent used for annealing polystyrene (PS) films of thickness 75 - 500 nm on top of silicon wafers with a native (1.8 nm thick) oxide layer was observed. A system that does not dewet when thermally annealed, as the van der Waals driving force in Equation 1.7 is weak. The films dewetted very slowly in a good solvent (toluene) vapour, where the PS chains assume a loose, open coil conformation.[41, 42] However, the PS films dewetted readily in a mixture of the vapour of a good solvent (toluene) and a non-solvent (ethanol), and the results highlight the role of elastic recoiling forces. In pure ethanol the PS chains are completely insoluble and hardly even swell, assuming a compact globule conformation through volume interactions in dilute solutions,[43] but in mixtures of toluene and ethanol the chain behavior is more complicated and somewhat paradoxical.[44-45] The preferential adsorption of the toluene in the vapour mixture leads to a strong collapse of the chains, so that, compared to the pure good solvent case, an overall shrinking of the polymer chains is observed. Although this behavior has been predicted by Monte-Carlo calculations in pioneering work by Magda et al.,[45] and observed in scattering experiments in dilute regimes,[42-43, 46] or on brushes,[47] this is the first demonstration of how thoroughly the addition of the non-solvent affects dewetting morphology, dewetting rate, and dewetting mechanism.

4.2   Methods and Materials

Polystyrene films of thickness 75 – 100 nm (PS96k, M_w = 96 kg mol^{-1}, M_w/M_n = 1.01) were spin-coated (20 - 30 mg mL^{-1} in toluene) onto prime grade silicon wafers coated with a native oxide layer (1.8 ± 0.2 nm thick), which were cleaned according to the procedure described in Section 2.1. To induce dewetting, the PS films were placed in a saturated vapour environment of mixtures of toluene and ethanol, varying the weight ratio of the solvents in the liquid phase, in a custom-

designed Teflon cell (Figure 2.9(a)), which allowed for *in situ* observation of dewetting by optical microscopy.

Thicker films (thickness 100 - 500 nm) were prepared by dip coating the wafers in a PS192k solution (M_w = 192 kg mol^{-1}, 26 – 61 mg mL^{-1} in toluene, lowered at 100 mm min^{-1}). Spectroscopic ellipsometry and x-ray reflectometry were used to establish film thickness, with measurements over three points on each sample. Atomic force microscopy (AFM) was used to characterize hole morphology and to measure the contact angle of the isolated PS droplets on the substrate at the end of dewetting.

The dewetting rate of the PS films was calculated using the central difference first derivative of the equivalent radius of the area of a growing hole in the polymer film as measured by NIS-Elements software from timelapse images typically taken at 30 s intervals.

The quality of the solvents for PS was estimated using Hansen Solubility Parameters (Table 4.1). These were used to predict, qualitatively, the relative solubility of each polymer/solvent combination. The cohesive energy density of the polystyrene and solvent molecules (square of the solubility parameter δ) was expressed in terms of the dispersive (*D*), polar (*P*) and hydrogen (*H*) bonding contributions to the total solubility parameter. The similarity in the cohesive energy density of two molecules 1 and 2 (R_a) was calculated in the three-dimensional space defined by the contributing solubility parameters by:[48]

$$R_a{}^2 = 4(\delta_{D1} - \delta_{D2})^2 + (\delta_{P1} - \delta_{P2})^2 + (\delta_{H1} - \delta_{H2})^2 \qquad (4.1)$$

Where an experimentally determined sphere of radius R_o = 8 MPa$^{1/2}$ for PS enclosed all of the 'good' solvents, and the relative energy difference (RED) was calculated from the ratio of the interaction distance R_a and the radius R_o.[48] As illustrated in Table 4.1, toluene is a good solvent for polystyrene (RED < 1), whereas ethanol is a non-solvent (RED >1).[48]

Table 4.1: Dispersive (D), polar (P) and hydrogen bonding (H) contributions to the total Hansen solubility parameters for polystyrene, toluene and ethanol. Relative energy density (RED) reflects the quality of the solvents for solvating polystyrene. RED < 1 represents a good solvent, RED > 1 is a non-solvent.[48]

Material	Hansen Solubility Parameters (MPa$^{1/2}$)			RED_{PS}
	δ_D	δ_P	δ_H	
Polystyrene (PS)	18	5	5	0
Toluene	18	1.4	2	0.6
Ethanol	15.8	8.8	19.4	1.9

Toluene and ethanol are entirely miscible and were mixed in the liquid phase inside the custom-designed Teflon chamber, depicted in Figure 2.9(a), in different weight proportions (99:1, 95:5, 90:10, 85:15, 60:40, and 40:60 (w/w) toluene/ethanol). The mole fraction of each component in the vapour phase is known,[49] and tabulated in Appendix A. For clarity, the weight composition of the liquid mixture will be referred to in this Chapter.

4.3   Results

Thermal annealing of the prepared PS96k films at 180 °C (above the $T_g = 100$ °C for bulk PS)[50] for long periods of time (> 65 h) increased the surface roughness, but did not initiate film dewetting from the substrate, due to the small van der Waals driving force (Figure 4.1).[14]
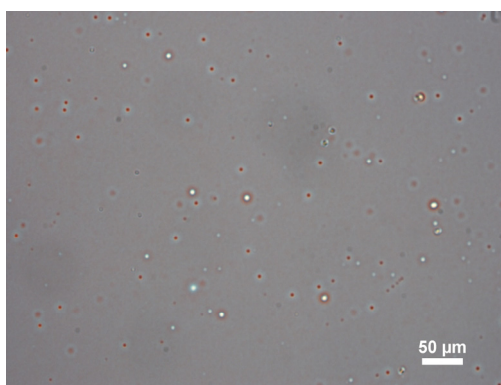

Figure 4.1: Representative optical micrograph of PS96K film of thickness 95 nm on a silicon wafer with 1.8 nm oxide layer after thermal annealing at 150 °C for 5 days.

Upon exposure to the solvent vapour environment, the PS96k films immediately changed color due to swelling. X-ray reflectometry data showed that a 78 ± 0.5 nm PS96k film swelled to 109 nm in the saturated toluene vapour (a thickness increase of 31 nm, 40% of the initial thickness) (Figure 4.2). Using the empirical rule that 1% of toluene lowers the T_g by 5 °C,[51] the increase in chain mobility was dramatic, leading to a T_g below room temperature. In contrast, upon exposure to vapours of a 30:70 (w/w) toluene/ethanol mixture, the swelling of the PS film was only 20 nm, 65% of the value obtained in pure toluene. The swelling of the same film in pure ethanol vapour was just 3 nm. This information will be used later to explain the observed dewetting behavior.
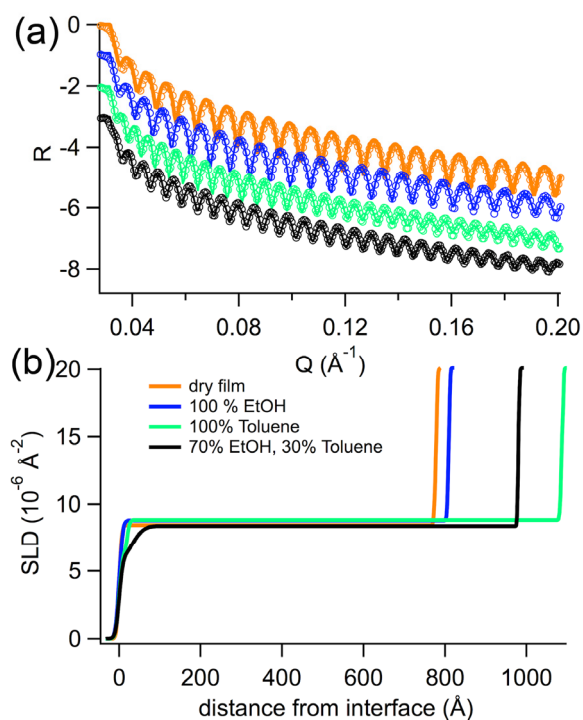
Figure 4.2 (a) X-ray reflectivity profiles from solvent swollen PS96k films. Experimental data (empty circles) and fits (lines) are shown. From top to bottom the lines correspond to: as prepared (dry) PS film (orange), film annealed on 100% ethanol (blue), film annealed in 100% toluene (green), and annealed in 30:70 toluene/ethanol (black). (b) Corresponding scattering length density (SLD) profiles.

4.3.1   Overview on the effect of annealing in good/non-solvent vapour mixture

Annealing the PS96k films in pure toluene resulted in a very slow dewetting process, as expected due to the small van der Waals driving force[14] (Figure 4.4(a-d)):

few holes nucleated and grew slowly, reaching the size of 100 μm after two hours of toluene vapour annealing. Complete dewetting into isolated droplets occurred only after 3 days of annealing. The nucleated holes had irregular shape, and jagged hole rims, that led to irregular, wide fingers, which did not develop into droplets. In comparison, thermal dewetting of the same PS films on an underlying polymethylmethacrylate (PMMA) film led to regular, circular holes as illustrated in Figure 4.3(a-d). It should be noted that the striated appearance of the film is attributed to the non-uniform casting of the underlying PMMA film from acetone solution. These striations are also evident when poly4vinylpyridine (P4VP) films are cast from ethanol in subsequent Chapters. In all cases, the striations appeared to not affect the formation and growth of holes in the film layer during dewetting.
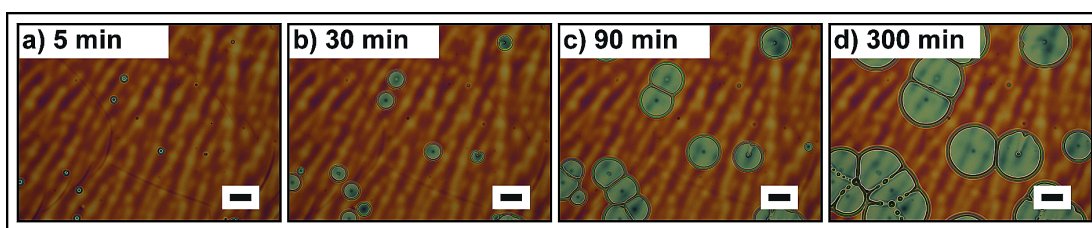
Figure 4.3: Representative optical micrographs of *in situ* annealing of PS 96k thin films (75 ± 0.8 nm) (a-d) on a film (150 nm thick) of PMMA at 180 °C. Scale bar = 50 μm.

The addition of the saturated vapours of ethanol to the annealing environment resulted in much faster dewetting of the PS96k films. In 85:15 toluene/ethanol mixture, the PS96k film dewetted completely within 10 minutes (Figure 4.4(e-h)). Upon addition of more than 1% wt. ethanol, the hole rims became unstable in all cases, leading to numerous and regular fingers, which pinched off and shed numerous droplets inside the growing hole (Figure 4.4(e-h)). In contrast, in the case of pure toluene annealing, isolated polymer droplets were only formed upon coalescence of adjacent holes, and the droplets were found not inside the holes, but on lines of coalescence of neighboring holes.
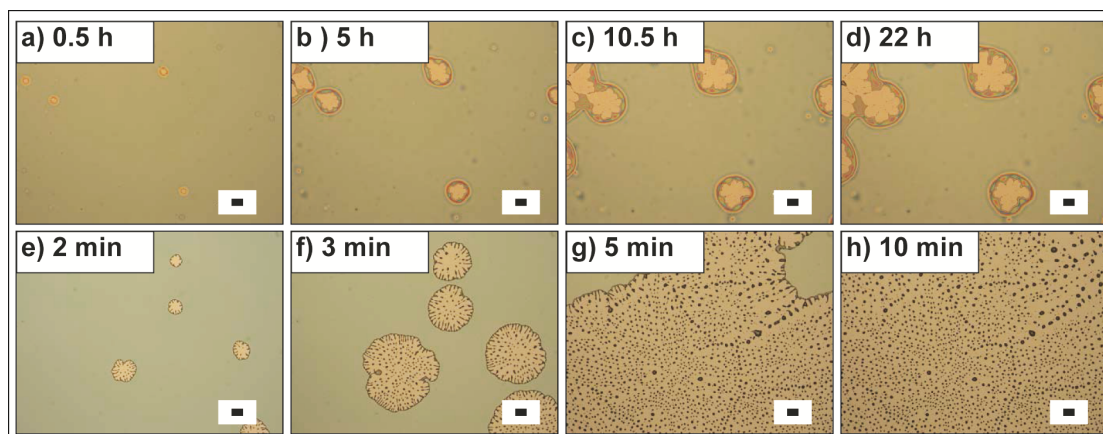
Figure 4.4: Representative optical micrographs of *in situ* annealing of PS 96k thin films (75 ± 0.8 nm), at room temperature (23 ± 1 °C), (a-d) dewetting in the saturated vapour of toluene; and (e-h) in a mixture of 85:15 (w/w) toluene and ethanol vapour. Time stamps indicate time since start of vapour annealing. Scale bars = 100 μm.

4.3.2   Rim morphology

The morphology of rims around dewetted holes was strikingly dependent on annealing solvent, as shown in Figure 4.5, which compares two hole rims of similar width ≈ 40 μm, formed in pure toluene (part a) and in 80:20 (w/w) toluene/ethanol mixture (b). The rim obtained in pure toluene was low and wide, with a low contact angle of 2° - 4° on top of the silicon wafer (Figure 4.5(c); also discussed later in Table 4.2); the hole at this stage was still round and regular in shape, with minimal fingering, and the rim width w increased slowly (Figure 4.6), and linearly with increasing hole radius, $w \propto 0.33\ r$ (Figure 4.5(d), blue diamonds).

Upon the addition of 5% wt. (or greater) ethanol, the rim grew much faster (Figure 4.6), reaching a much higher aspect ratio (six times greater height for a rim of similar width, approximately 1200 nm versus 200 nm in pure toluene, Figure 4.5 b and c) and higher contact angle (9° - 14°). From a width of less than 8 μm the rim developed periodic undulations along the circumference, with some portions becoming thicker and elongated (cross-section *i*, Figure 4.5(c)), and some portions becoming thinner and narrower (cross-section *ii*, Figure 4.5(c)). The thick elongated portions formed fingers, which repeatedly formed a neck and broke up into droplets. The rim width (averaged over the whole circumference) followed a linear growth with hole radius, $w \propto 0.04\ r$ (Figure 4.5, green triangles). The labels **I**, **II**, and **III** on the data for the 95:5 and 99:1 wt. mixtures correspond to the optical micrographs in Figure 4.8(c), which identify the first captured dewetted hole (**I**), the stage when the

rim is well established (**II**), and the stage when undulations (for the 99:1 case) or fingering (for the 95:5 case) were well established (**III**).
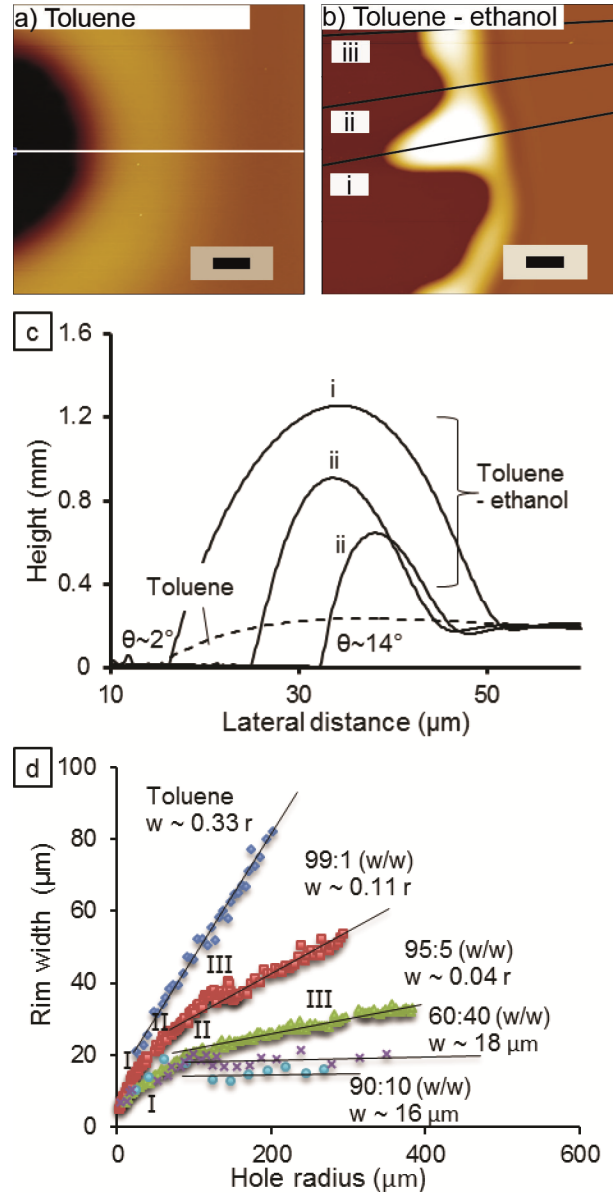
Figure 4.5: AFM micrographs of the rim surrounding a hole in PS96k films (154.8 ± 0.7 nm thick) annealed in saturated (a) toluene vapour, height scale = 400 nm; (b) 80:20 (w/w) toluene/ethanol mixture, height scale = 1400 nm, scale bars = 20 μm. (c) AFM cross-sections of hole rims, showing the receding contact angle (error ± 2°) of the rims on the substrate (dashed line for toluene, solid line for toluene/ethanol); sections i – iii were taken along the lines indicated in part (b). (d) Hole rim width versus hole radius for PS96k films (75 ± 0.8 nm) annealed in saturated toluene (blue diamonds), 99:1 (red squares), 95:5 (green triangles), 90:10 (blue circles) and 60:40 (purple crosses) (w/w) toluene/ethanol mixtures. Roman numerals refer to the micrograph sequences for 99:1 and 95:5 in Figure 4.8(c). The standard deviation in the data points is smaller than the size of the symbols.

The observation of large undulations of the rim width are indicative of a dewetting mechanism dominated by interfacial slip of the melt at the solid substrate.[19] Upon addition of ethanol in the annealing atmosphere, ethanol molecules likely adsorbed to the silicon oxide substrate, increasing the interfacial slip of the PS on top of the ethanol layer. This effect was clear at 5% wt. ethanol, but already observable at a reduced level at 1% wt. ethanol: the undulations in the rim width became more frequent than those observed in pure toluene (see micrographs in Figure 4.8(c)). For both 90:10 and 60:40 (w/w). toluene/ethanol proportions, the rim width was similar and reached an averaged constant value at early stages. Figure 4.6 shows the same rim width data as in Figure 4.5(d) plotted against time, and highlights how much faster the maturation of the rim occurred in the presence of ethanol.
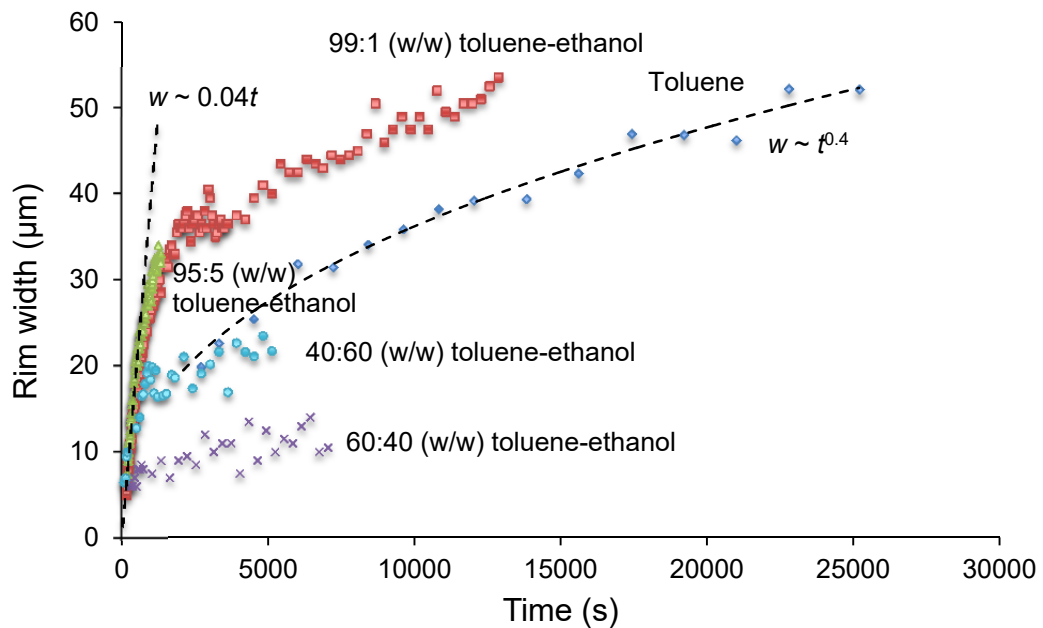
Figure 4.6: Growth of rim width over time for holes dewetting in PS96k (78 nm thick) films annealed in the saturated vapour of pure toluene (blue diamonds), 99:1 (w/w) toluene-ethanol mixture (red squares), 95:5 (w/w) toluene-ethanol mixture (green triangles), 60:40 (w/w) toluene-ethanol mixture (blue circles) and 40:60 (w/w) toluene-ethanol mixture (purple crosses). The data (symbols) are shown, with two fits (broken lines).

4.3.3   Droplet morphology

The PS droplets found on the silicon substrate at the end of dewetting in pure toluene vapours were irregular in shape, appearing pinned to the substrate (Figure 4.7(a)), while they were nicely round and regular upon addition of 15% wt. ethanol (Figure 4.7(b)).
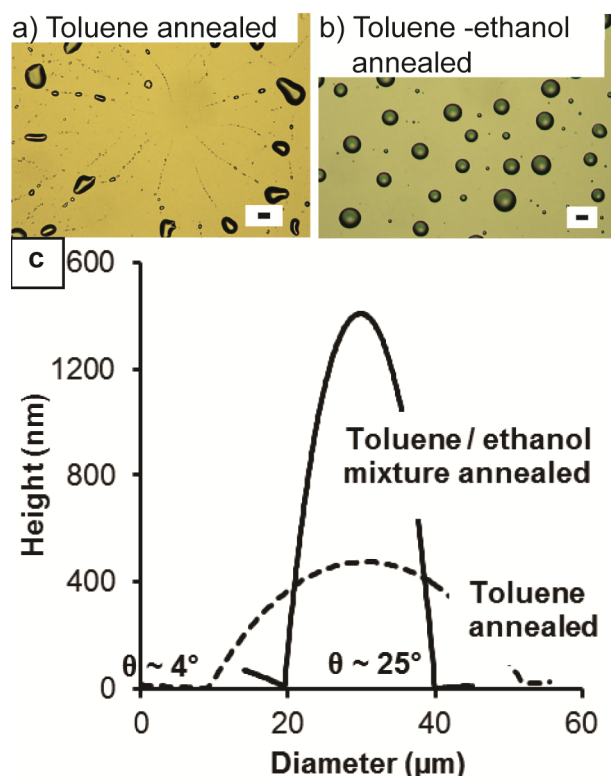
Figure 4.7: Optical micrographs of isolated PS96k droplets after completely dewetting 97 ± 1 nm thin polystyrene films at room temperature (23 ± 1 °C) in (a) saturated toluene vapours. Scale bar = 100 μm; (b) 85: 15 (w/w) toluene/ethanol mixture. Scale bar = 20 μm. (c) *Ex situ* AFM cross sections of PS96k droplets dewetted under toluene annealing (broken line), and 85:15 (w/w) toluene/ethanol mixture annealing (solid line), with indicated contact angle.

The contact angle of PS droplets on the silicon substrate was higher (25° ± 2°) when the films were annealed in the presence of 15% wt. ethanol, compared to the pure toluene vapours (4° ± 2°, Figure 4.7(c), and Table 4.2). Adding 15% wt. ethanol into the annealing vapour decreased the spreading parameter of PS on the substrate by one order of magnitude compared to annealing thermally and in pure toluene (Table 4.2). This effect can be explained with the polar interactions between ethanol

and silicon oxide, which reduced the spreading of PS, and increased its dewetting rate.

Table 4.2: Contact angle, diameter, deviation from the mean diameter, and distribution density of the isolated PS96k droplets after annealing 97 nm thick films in solvent vapours. The spreading parameter is calculated from $S = \gamma_{PS} (\cos\theta - 1)$, where γ is the surface tension of PS (41 mN/m at 20 °C)[52] and θ is the contact angle of PS droplets on silicon oxide/ silicon substrates.

Annealing procedure	Contact angle (°)	Droplet diameter (μm)	Deviation from mean diameter (μm)	Droplet density (mm^{-2})	Spreading parameter (mN/m)
Thermal above T_g	7.5 ± 5 [a]	-	-	-	-0.35
Toluene vapour	4 ± 1	21 ± 2	25	50	-0.10
85:15 (w/w) toluene-ethanol vapours	25 ± 2	13 ± 1	3	746	-3.8

[a] Literature value obtained by dewetting thermally a PS film on a 200 nm thick silicon oxide layer on silicon.[53]

4.3.4   Dewetting rate

It is obvious from Figure 4.8 that film dewetting became much faster upon addition of ethanol vapour to toluene vapour. The dewetting rate reached a maximum at 15% wt. ethanol, and decreased again at values higher than 15% wt., until no dewetting was observed in pure ethanol vapour (inset of Figure 4.8(a)). Figure 4.8 (a and b) illustrate the growth of the diameter of the dewetted holes, D, versus time, t, and the dewetting velocity versus hole radius, respectively, until hole coalescence or until the holes grew outside the frame. In all annealing conditions, in the early stage $D \propto t^{2/3 \pm 0.1}$, characteristic of a regime where interfacial slip of the polymer at the solid surface is the dominating mechanism.[16, 54] In a later stage, $D \propto t^{1 \pm 0.1}$, characteristic of a regime where dissipation takes place mainly by viscous flow within the rim.

.
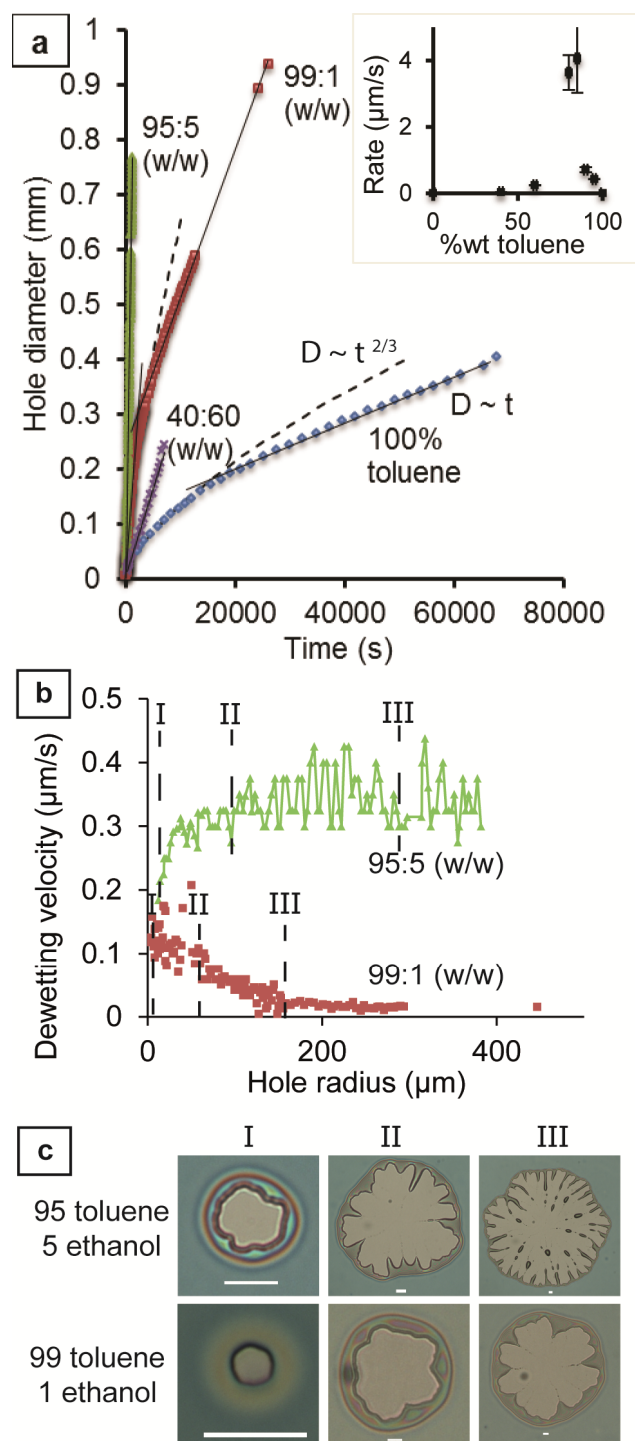
Figure 4.8: (a) Hole growth rate during dewetting of a 74.2 ± 0.8 nm thick PS96k film on a silicon substrate. The data is fitted by a power law $D \propto t^{2/3}$ at short times, and by $D \propto t$ at later times. Inset: dewetting rate as a function of toluene content in the annealing solvent mixture. (b) Evolution of the dewetting velocity of the PS film when annealed in 99:1 (w/w) toluene/ethanol (red squares) and 95:5 (w/w) toluene/ethanol vapour (green triangles). (c) Optical micrographs of dewetted holes at three successive stages indicated in the text. Scale bars = 20 μm.

The transition between these two regimes is clearly visible in Figure 4.8(a) for the pure toluene case (blue diamonds with dashed line and solid line fits) and the 99:1 (w/w) toluene/ethanol case (red squares with solid line fits), while it cannot be appreciated for the 95:5 and 40:60 (w/w) cases, as it occurs at shorter times and smaller hole radius. This transition between slip and viscous dissipation is well known for polymer thin films dewetting.[16-17, 54] It is expected that in the case of interfacial slip the frictional forces are proportional to the size of the moving rim, so that when a critical rim size is reached, interfacial slip becomes a minor contributor to dewetting, and the dewetting rate becomes dominated by the viscous dissipation within the rim.[17] From the characteristic time of this transition, an estimate of the slip length and reptation times can be derived, as shown in Table 4.3 below

The change in rim width over time (Figure 4.6) can be matched up with the change in dewetting velocity (Figure 4.8(b)), and the appearance of rim undulations (Figure 4.8(c)). For the 99:1 (w/w) toluene/ethanol case, the dewetting rate decreased steadily in the initial stages (stages **I** - **II**), while the rim width was still growing, and undulations in the transverse direction were starting to grow (Figure 4.8(c)). Once the rim width growth slowed down and the undulations in rim width reached a steady state (stage **III**), the dewetting rate also reached a constant value ($v \approx 0.02$ μm/s at a hole radius of 160 μm, stage **III**), corresponding to the transition from a slip regime to dynamics dominated by viscous dissipation.[16]

In the 95:5 (w/w) toluene/ethanol case, the dewetting velocity initially grew with time while the hole was opening up (up to stage **I**) and fingering was developing (stages **II**), and then reached an average constant value in correspondence to the stage where fingering and droplet shedding also reached an established steady state (stage **III**).

4.3.5   Dewetting thick polymer films

To further demonstrate the strong drive for dewetting with toluene/ethanol mixtures, increasingly thicker films of a higher molecular weight polymer, PS192k, were annealed in the vapour mixture of 85:15 (w/w) toluene/ethanol. Strikingly, films of thickness from 100 nm to over 500 nm, very thick compared to expected range of action of interfacial forces (< 100 nm), could be easily dewetted this way. Similar fingering behavior was observed as with thinner films (Figure 4.9(a-d)). As

expected, droplet diameter increased with increasing film thickness, and droplets as large as 250 μm were produced (Figure 4.9(e)), with the density distribution of droplets decreasing accordingly. Dewetting rate decreased with increasing film thickness (Figure 4.9(f)), as expected, but still maintaining high values compared to the negligible dewetting that would occur in pure toluene.
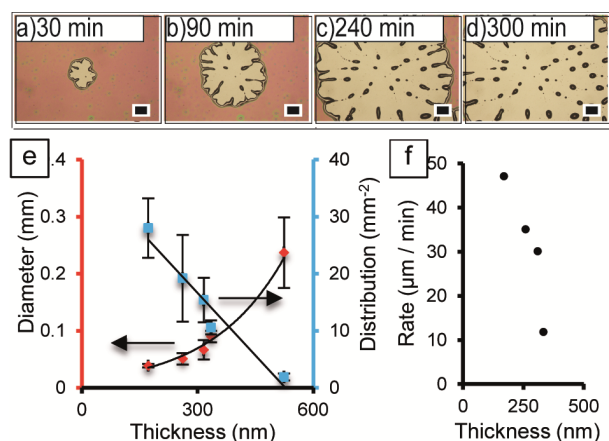
Figure 4.9: (a) – (d) Optical micrographs illustrating the dewetting of thick PS192k films (335 nm thick) in a mixture of 85:15 (w/w) toluene/ethanol, at room temperature (23 ± 1 °C), for the indicated times. Scale bars = 200 μm. (e) Average PS192k droplet diameter (red diamonds) and droplet distribution (blue squares) as a function of film thickness (lines are to guide the eye); (f) hole growth rate as a function of film thickness. Rate data was not collected for the 520 nm thick films as dewetting proceeded over a period of five days.

4.3.6   Reducing residual stress

Thermally annealing polymer films for extended periods of time at temperatures below T_g is known to reduce the elastic stress within the film, and lead to a decrease in hole nucleation density.[28, 33] Here, a PS96k film (75 nm thick) was thermally pre-annealed at 105 °C for 72 h (just above the bulk T_g of PS) prior to annealing in a saturated environment of 80:20 (w/w) toluene/ethanol mixture (Figure 4.10(a-c)). The dewetting morphology and rate were compared with the dewetting of an untreated film of the same thickness and molecular weight (Figure 4.10(d-f)). The holes in the thermally pre-treated film grew with a constant velocity that was approximately two orders of magnitude lower than that for untreated films (Figure 4.10(g-h)). These findings confirm earlier results that residual elastic stresses stored in the films provide an additional driving force for dewetting, and that when films are pre-equilibrated above T_g, these stresses may relax and the

hole growth slows down. In these pre-equilibrated films the dewetting rates are still much larger than in pure toluene, so we can conclude that the additional elastic stress specifically due to the exposure to a good/non-solvent mixture contributes substantially to the dewetting forces.
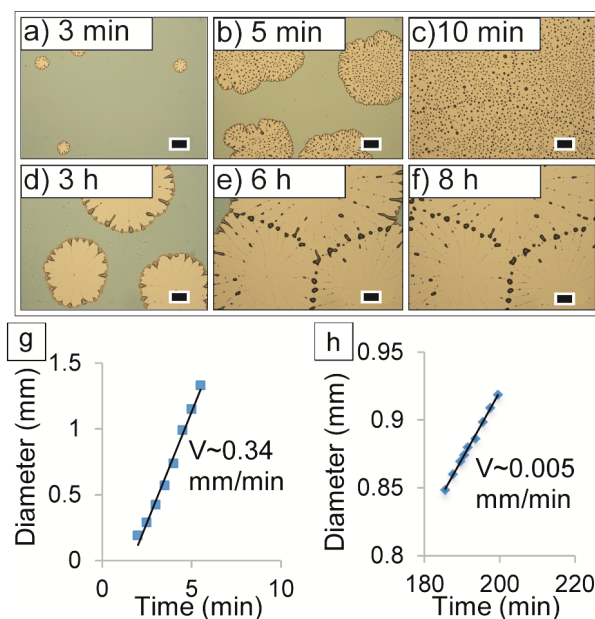
Figure 4.10: Thin PS96k film (76 ± 2 nm thick) annealed in the saturated vapour of 80:20 (w/w) toluene – ethanol mixture. (a-c) Film was solvent annealed as cast. (d-f) Film was thermally aged at 105°C for 72 h to reduce internal stress prior to annealing. Scale bars = 200 μm. Hole diameter as a function of annealing time of the (g) as cast, and (h) thermally pre-annealed films.

4.4   Discussion

By collating all of the presented results, the effect of adding a small amount of ethanol to a toluene annealing environment for PS films can be rationalised. The investigated PS films did not dewet when annealed thermally and dewetted very slowly when exposed to pure toluene, but dewetted readily when even a small amount (2% wt.) of ethanol was added. The main conclusion is that annealing polystyrene films in good/non-solvent mixtures led to much stronger elastic recoiling forces than those usually observed when thermally annealing spin-cast films. This conclusion is substantiated in a few points below.

4.4.1   Rim morphology and dewetted droplet shape

The low contact angle of dewetted droplets and the shallow and wide rims obtained in pure toluene (Figure 4.5(a)) are a consequence of the conformation of the PS chains, which take on a loose, open coil conformation, retained and locked-in even after the toluene vapour evaporates. The higher contact angle and the narrower and taller rims obtained when a small quantity of ethanol (1% wt.) was added to the system are a consequence of the PS chains retracting into a compact globule conformation, as a result of the preferential adsorption of toluene in the vapour mixture. This peculiar situation could be thought of as an 'onion-like' structure: a core in which toluene molecules swell the PS chains, bridging together different chain segments, surrounded by an outer shell of ethanol, which ultimately drives the chain compaction (Figure 4.12). The macro- and microscale observations are a consequence of the change in conformation of the polymer chains in the different solvents. It is believed that this is the first time that the collapse of the chains due to preferential adsorption of a good solvent in solvent mixture, as predicted by simulations,[45, 55] has been observed in a thin polymer film.

4.4.2   Effect of adding ethanol on dewetting rate

Upon addition of up to 15% wt. ethanol to toluene, the steady-state dewetting rate increased by more than two orders of magnitude (Figure 4.8(b)) compared to the pure toluene case. The bell- shaped curve of the average dewetting rate versus solvent mixture composition, with a maximum rate at 15% wt. concentration of ethanol (inset of Figure 4.8(a)), can be explained with the competition between the effects of the two solvents. The solvation of PS in toluene is required for dewetting to occur; as it plasticises the chains and allows PS to flow (no dewetting was observed in pure ethanol vapour). The addition of ethanol drove the dewetting faster in two ways: on the one hand, by establishing polar interactions with the hydroxide groups on the silicon oxide substrate, which favor the spreading of ethanol and reduce the spreading parameter of PS. On the other hand, by reducing the PS viscosity as a consequence of the collapsed and less entangled conformation of the PS chains, as will be discussed later. Increasing the amount of ethanol vapour above 15% wt. reduced the average dewetting velocity, due to reduced mobility of the chains because of the lower toluene content when dewetting started. Indeed, the

uptake of the toluene in PS films has been seen to be considerably slowed down in an under-saturated atmosphere.[56] X-ray reflectometry data reinforce this explanation, as at 30:70 (w/w) toluene/ethanol the swelling of the PS film was only 60% of the value obtained when annealing in pure toluene (Figure 4.2(b)).

4.4.3   Molecular recoiling forces

Thermally pre-annealing the films close to T_g, and then exposing them to a mixed toluene/ethanol atmosphere, reduced the dewetting rate significantly. Very thick PS films - as thick as 520 nm - could be dewetted by annealing in toluene/ethanol vapour mixtures. The latter two observations point to strong elastic forces driving dewetting, in addition to the polar interactions at the interface.

Annealing the PS films above T_g drives the chains away from their out-of-equilibrium 'frozen' conformation obtained through casting, towards more energetically favoured quasi-equilibrium conformations.[27] This elastic rearrangement has been described in the past, particularly in ultra-thin films where elastic forces due to extreme confinement are strong.[57] Since the films prepared here had a thickness between $4R_g$ and $60R_g$, confinement effects were not very strong, and it was instead the addition of the non-solvent ethanol that drove dewetting dramatically. These observations are closely related to previous work by the Reiter and other groups on dewetting driven by relaxation of residual elastic stresses within the film.[28-29, 33-34, 42, 58-59] However, in this study, introducing ethanol in the annealing environment substantially increased the recoiling forces in the rim region, and made the phenomenon more obvious.

4.4.4   Transition from slip to no-slip regimes

In all the vapour annealing situations investigated the hole growth followed the typical behavior expected for thin PS films dewetting upon thermal annealing (power law $D \sim t^{2/3}$ for slip dominated behavior, followed by a constant dewetting rate $D \sim t$ for a viscous dominated behavior) at a characteristic time, τ.[16] However, when more than 1% wt. ethanol was added to the environment, the transition between the two regimes occurred at earlier times (Figure 4.8(b)).

According to accepted models,[16] in the initial dewetting period when the rim width is still growing, the dewetting velocity is dominated by interfacial slip, and is described by the power law $D \propto t^{2/3}$. In this regime the velocity is determined by:[17]

$$V_{slip} = \frac{1}{6}\frac{\gamma}{\eta}\theta^2\frac{b}{w} \tag{4.2}$$

with γ and η the surface tension and viscosity of the liquid respectively, θ the contact angle of the liquid on the substrate, b the slip length (the distance at which the velocity of the liquid extrapolates to zero) and w the width of the rim. It is straightforward to see from Equation 4.2 that as the rim width w grows, there is a proportional reduction in dewetting velocity, and this regime is clearly visible for the 99:1 (w/w) mixture (Figure 4.8(b)).
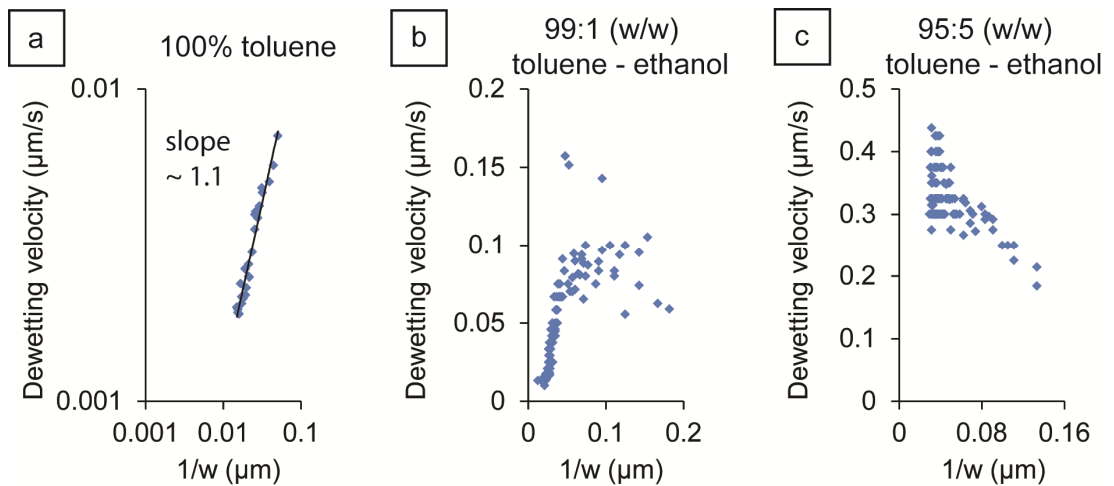
Figure 4.11: Dewetting velocity as a function of the inverse of rim width for PS96k films annealed at 23 ± 1 °C in the saturated vapours of (a) toluene, (b) 99:1 (w/w) toluene – ethanol mixture and (c) 95:5 (w/w) toluene-ethanol mixture.

Figure 4.11(a) clearly shows that V_{slip} decreases with increasing rim width during toluene vapour annealing. Adding only 1% wt. ethanol to the vapour environment results in the initial V_{slip} decreasing not as strongly with increasing rim width (Figure 4.11(b)). Further addition of ethanol to the vapour mixture, results in V_{slip} becoming independent of the rim width, suggesting possibly a change both in the interfacial properties of the substrate and the molecular properties of the

polystyrene. When $w = bL/\theta$, where L is a constant of order 10,[60] the dynamics become viscosity-dominated, and slip is no longer the main dissipation mechanism.

Slip length values, b, shown in Table 4.3 were estimated from the value of rim width at which this transition from $R \propto t^{2/3}$ (slip) to $R \propto t$ (no-slip) occurred for the cases of annealing in pure toluene and in 95:5 (w/w) toluene/ethanol (in these two cases the viscosity could be approximated to be unchanged). The value of slip length, $b = 700$ nm, obtained for the 95:5 wt. toluene/ethanol case, is close to that obtained for PS dewetting on hydrophobised silicon OTS monolayers.[61] The increase in slip length on addition of ethanol is corroborated by the observation that the dewetted patterns in this case developed extensive fingering and droplet shedding, which is a signature of slip-dominated regimes.[21] Finally, it is expected that slip should become more dominant in situations, such as the mixed toluene/ethanol atmosphere, where the liquid wets the substrate less, and where the polymer coils are more compact and solid-like.[62-63] By adding ethanol to the annealing mixture, the interfacial slip mechanism in the early stage of dewetting has been enhanced in a manner that is more immediate and tunable than the modification of surface energy via self-assembled monolayers.[64-65]

Table 4.3: Slip length and characteristic transition time from elastic to viscous dewetting regimes for PS96k films (75 nm thick) annealed in toluene and toluene/ethanol vapours. The derivation of the slip length is explained in the text.

Annealing environment	Slip length, b (nm)	Characteristic time, τ (s)
Pure toluene	350	20 000
99:1 (w/w) toluene - ethanol	-	3000
95:5 (w/w) toluene - ethanol	700	270
60:40 (w/w) toluene - ethanol	-	1000
40:60 (w/w) toluene – ethanol	-	2000

4.4.5   Film viscosity

From the experiments described, a reptation time could be extracted (the time required for the polymer chain to completely emerge from its 'tube'[41-42]), which is proportional to the viscosity of the polymer solution and its concentration. The time, τ, at which the hole growth rate in a dewetting film transitions from the slip-dominated to the viscous-dominated regime is proportional to the reptation time of

the chains within the melt.[29] Table 4.3 shows the characteristic times at which this transition occurred for PS films annealed in the different solvent mixtures.
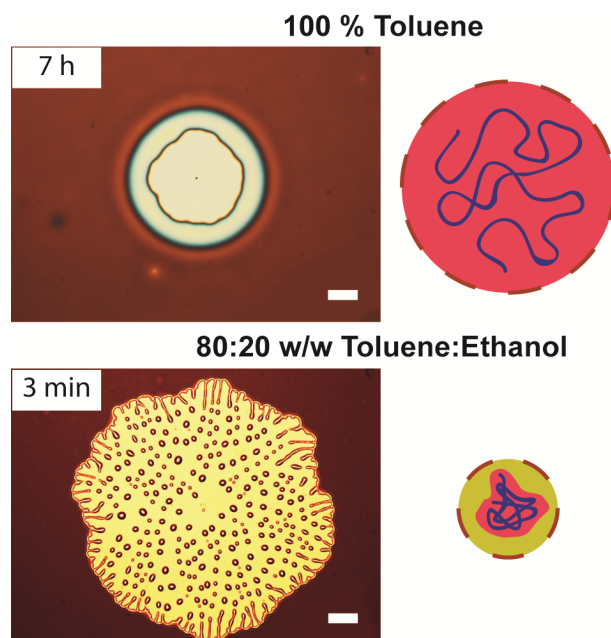
Figure 4.12: Schematic summary of these experiments: optical micrographs of a hole formed in a PS96k film (75 nm) dewetting in toluene vapour (above) after the indicated time of annealing, and in toluene/ethanol vapour mixture (below), scale bars = 200 μm; on the right corresponding chain conformations: swollen PS chain in toluene (red colour), and collapsed chain in the solvent mixture (toluene red, ethanol yellow outside).

For relatively constant toluene content, (100% toluene, 99:1 (w/w) toluene/ethanol and 95:5 (w/w) toluene/ethanol) there is a two orders of magnitude decrease in characteristic transition time upon addition of ethanol. It is reasonable to consider that these transition times are proportional to the reptation time of the PS chains in the films, which can be attributed to two concurrent effects: an increase in interfacial slip due to adsorption of ethanol molecules to the substrate, and a reduction of polymer viscosity due to the collapse of the polymer chains and subsequent decrease in entanglement. It is not possible to distinguish and isolate these two effects, but it is likely they both play a role. The collapse of the polystyrene chain due to the preferential adsorption of toluene in the mixed vapour environment, was simulated by Magda in infinitely dilute solutions,[45] and is nicely replicated here, and partially explains the increased dewetting rate upon addition of ethanol. Figure 4.12 is a schematic summary of the observations discussed in this

chapter, whereby the presence of ethanol in the solvent mixture results in dramatically increased dewetting rates and extensive fingering in the dewetted holes, due to the 'onion-like' structure of the toluene preferentially adsorbed to the PS chains within an ethanol shell.

4.5   Conclusions

The experiments discussed in this Chapter demonstrate that the addition of ethanol vapour to a toluene vapour atmosphere affects drastically and on many levels the dewetting process of PS films. The consequences of adding up to 15% wt. ethanol to the toluene vapour atmosphere are: a reduced spreading parameter of the PS on the silicon oxide substrate, a reduced viscosity of the PS, an increased dewetting rate, a slip-dominated hole growth with extensive fingering, and the ability to dewet films as thick as 520 nm. The observed phenomena are attributed to the transition of the polymer chains to a globular conformation in a toluene/ethanol mixture, due to the strong preferential adsorption of the toluene. This behavior, predicted by Shultz and Flory,[44] and explored by numerical simulations by Magda *et al.*[45] for infinitely dilute polymer solutions, is much more pronounced in polymer melts. The addition of ethanol drives the dewetting faster, not only because the spreading parameter becomes more negative, but because the strong elastic recoiling forces on the chains drive hole growth and interfacial slip is increased. From an application perspective, annealing metastable films in mixed solvent vapours is a convenient and tunable way to produce very large dewetted droplets, and to tune the dewetting dynamics more strongly towards a slip regime, without the need for surface modification.

4.6   References

1.   de Gennes, P. G. Wetting: statics and dynamics. *Rev. Mod. Phys.* **1985,** *57* (3), 827.

2.   Srolovitz, D. J.; Safran, S. A. Capillary instabilities in thin films. II. Kinetics. *J. Appl. Phys.* **1986,** *60*, 255-260.

3.   Reiter, G. Dewetting of Thin Polymer Films. *Phys. Rev. Lett.* **1992,** *68* (1), 75-78.

4.   Xie, R.; Karim, A.; Douglas, J. F.; Han, C. C.; Weiss, R. A. Spinodal Dewetting of Thin Polymer Films. *Phys. Rev. Lett.* **1998,** *81* (6), 1251-1254.

5.   Saulnier, F.; Raphaël, E.; de Gennes, P.-G. Dewetting of thin-film polymers. *Phys. Rev. E* **2002,** *66* (6), 061607.

6.   Seemann, R.; Herminghaus, S.; Neto, C.; Schlagowski, S.; Podzimek, D.; Konrad, R.; Mantz, H.; Jacobs, K. Dynamics and structure formation in thin polymer melt films. *J. Phys.: Condens. Matter* **2005,** *17* (9), S267.

7.   Bäumchen, O.; Jacobs, K. Slip effects in polymer thin films. *J. Phys.: Condens. Matter* **2010,** *22* (3), 033102.

8.   Gentili, D.; Foschi, G.; Valle, F.; Cavallini, M.; Biscarini, F. Applications of dewetting in micro and nanotechnology. *Chem. Soc. Rev.* **2012,** *41* (12), 4430-4443.

9.   Xue, L.; Han, Y. Pattern formation by dewetting of polymer thin film. *Prog. Polym. Sci.* **2011,** *36* (2), 269-293.

10.   Thickett, S. C.; Moses, J.; Gamble, J. R.; Neto, C. Micropatterned substrates made by polymer bilayer dewetting and collagen nanoscale assembly support endothelial cell adhesion. *Soft Matter* **2012,** *8* (39), 9996-10007.

11.   Telford, A.; Meagher, L.; Glattauer, V.; Gengenbach, T.; Easton, C.; Neto, C. Micropatterning of polymer brushes: grafting from dewetting polymer films for biological applications. *Biomacromolecules* **2012,** *13* (9), 2989-2996.

12.   Ghezzi, M.; Wang, P. Y.; Kingshott, P.; Neto, C. Guiding the Dewetting of Thin Polymer Films by Colloidal Imprinting. *Adv. Mater. Interfaces* **2015,** *2* (11).

13.   Thickett, S. C.; Neto, C.; Harris, A. T. Biomimetic surface coatings for atmospheric water capture prepared by dewetting of polymer films. *Adv. Mater.* **2011,** *23* (32), 3718-3722.

14.   Seemann, R.; Herminghaus, S.; Jacobs, K. Dewetting Patterns and Molecular Forces: A Reconciliation. *Phys. Rev. Lett.* **2001,** *86* (24), 5534-5537.

15.   Brochard-Wyart, F.; Redon, C. Dynamics of liquid rim instabilities. *Langmuir* **1992,** *8* (9), 2324-2329.

16.   Brochard-Wyart, F.; de Gennes, P. G.; Hervert, H.; Redon, C. Wetting and slippage of polymer melts on semi-ideal surfaces. *Langmuir* **1994,** *10* (5), 1566-1572.

17.   Reiter, G.; Sharma, A. Auto-optimization of Dewetting Rates by Rim Instabilities in Slipping Polymer Films. *Phys. Rev. Lett.* **2001,** *87* (16), 166103.

18.   Münch, A.; Wagner, B. Impact of slippage on the morphology and stability of a dewetting rim. *J. Phys.: Condens. Matter* **2011,** *23* (18), 184101.

19.   Münch, A.; Wagner, B. Contact-line instability of dewetting thin films. *Physica D* **2005,** *209*, 178-190.

20.   Reiter, G. Evolution of rim instabilities in the dewetting of slipping thin polymer films. *J. Adhesion* **2005,** *81* (3-4), 381-395.

21.   Bäumchen, O.; Marquant, L.; Blossey, R.; Münch, A.; Wagner, B.; Jacobs, K. Influence of Slip on the Rayleigh-Plateau Rim Instability in Dewetting Viscous Films. *Phys. Rev. Lett.* **2014,** *113* (1), 014501.

22.   Sharma, A. Relationship of thin film stability and morphology to macroscopic parameters of wetting in the apolar and polar systems. *Langmuir* **1993,** *9* (3), 861-869.

23.   Sharma, A.; Khanna, R. Pattern Formation in Unstable Thin Liquid Films. *Phys. Rev. Lett.* **1998,** *81* (16), 3463-3466.

24.   Reiter, G. Dewetting of highly elastic thin polymer films. *Phys. Rev. Lett.* **2001,** *87* (18), 186101.

25.   Reiter, G.; de Gennes, P. G. Spin-cast, thin, glassy polymer films: Highly metastable forms of matter. *Eur. Phys. J. E* **2001,** *6* (1), 25-28.

26.   Bollinne, C.; Cuenot, S.; Nysten, B.; Jonas, A. M. Spinodal-like dewetting of thermodynamically-stable thin polymer films. *Eur. Phys. J. E* **2003,** *12* (3), 389-396.

27.   Yang, M.; Hou, S.; Chang, Y.; Yang, A. M. Molecular recoiling in polymer thin film dewetting. *Phys. Rev. Lett.* **2006,** *96* (6), 066105.

28.   Reiter, G.; Hamieh, M.; Damman, P.; Sclavons, S.; Gabriele, S.; Vilmin, T.; Raphaël, E. Residual stresses in thin polymer films cause rupture and dominate early stages of dewetting. *Nat. Mater.* **2005,** *4* (10), 754-758.

29.   Damman, P.; Gabriele, S.; Coppée, S.; Desprez, S.; Villers, D.; Vilmin, T.; Raphaël, E.; Hamieh, M.; Al Akhrass, S.; Reiter, G. Relaxation of residual stress and reentanglement of polymers in spin-coated films. *Phys. Rev. Lett.* **2007,** *99* (3), 036101.

30.   Thomas, K. R.; Steiner, U. Direct stress measurements in thin polymer films. *Soft Matter* **2011,** *7*, 7839.

31.   Ediger, M. D.; Forrest, J. A. Dynamics near Free Surfaces and the Glass Transition in Thin Polymer Films: A View to the Future. *Macromolecules* **2014,** *47* (2), 471-478.

32.   Barbero, D. R.; Steiner, U. Nonequilibrium Polymer Rheology in Spin-Cast Films. *Phys. Rev. Lett.* **2009,** *102* (24), 248303.

33.   Thomas, K. R.; Chenneviere, A.; Reiter, G.; Steiner, U. Nonequilibrium behavior of thin polymer films. *Phys. Rev. E* **2011,** *83* (2), 021804.

34.   Clough, A.; Chowdhury, M.; Jahanshahi, K.; Reiter, G.; Tsui, O. K. C. Swelling with a Near-Θ Solvent as a Means to Modify the Properties of Polymer Thin Films. *Macromolecules* **2012,** *45* (15), 6196-6200.

35.   Raegen, A.; Chowdhury, M.; Calers, C.; Schmatulla, A.; Steiner, U.; Reiter, G. Aging of thin polymer films cast from a near-theta solvent. *Phys. Rev. Lett.* **2010,** *105* (22), 227801.

36.   Lee, S. H.; Yoo, P. J.; Kwon, S. J.; Lee, H. H. Solvent-driven dewetting and rim instability. *J. Chem. Phys.* **2004,** *121* (9), 4346-4351.

37.   Xu, L.; Shi, T.; An, L. Nonsolvent-Induced Dewetting of Thin Polymer Films. *Langmuir* **2007,** *23* (18), 9282-9286.

38.   Xu, L.; Shi, T.; An, L. The dewetting dynamics of the polymer thin film by solvent annealing. *J. Chem. Phys.* **2008,** *129* (4), 044904.

39.   Burtovyy, R.; Luzinov, I. Reversibility of pH-Induced Dewetting of Poly(vinyl pyridine) Thin Films on Silicon Oxide Substrate. *Langmuir* **2008,** *24* (11), 5903-5910.

40.   Xu, L.; Sharma, A.; Joo, S. W. Dewetting of stable thin polymer films induced by a poor solvent: role of polar interactions. *Macromolecules* **2012,** *45* (16), 6628-6633.

41.   de Gennes, P. G. *Scaling concepts in polymer physics*; Cornell University Press, 1979.

42.   Grosberg, A. Y.; Khokhlov, A. *Statistical Physics of Macromolecules*; American Institute of Physics: New York, 1994. p 1-144.

43.   Baysal, B. M.; Karasz, F. E. Coil - Globule Collapse in Flexible Macromolecules. *Macromol. Theory Simul.* **2003,** *12* (9), 627-646.

44.   Shultz, A.; Flory, P. Polymer chain dimensions in mixed - solvent media. *J. Polym. Sci.* **1955,** *15* (79), 231-242.

45.   Magda, J.; Fredrickson, G.; Larson, R.; Helfand, E. Dimensions of a polymer chain in a mixed solvent. *Macromolecules* **1988,** *21* (3), 726-732.

46.   Nakata, M. Coil-globule transition of poly (methyl methacrylate) in a mixed solvent. *Phys. Rev. E* **1995,** *51* (6), 5770.

47.   Auroy, P.; Auvray, L. Collapse-stretching transition for polymer brushes: preferential solvation. *Macromolecules* **1992,** *25* (16), 4134-4141.

48.   Hansen, C. M. *Hansen solubility parameters: a user's handbook*; CRC press, 2007.

49.   Kretschmer, C. B.; Wiebe, R. Liquid-Vapor Equilibrium of Ethanol--Toluene Solutions. *J. Am. Chem. Soc.* **1949,** *71* (5), 1793-1797.

50.   Brandrup, J.; Immergut, E. *Polymer Handbook*; John Wiley & Sons, New York, NY, 1975.

51.   O'Driscoll, S.; Demirel, G.; Farrell, R. A.; Fitzgerald, T. G.; O'Mahony, C.; Holmes, J. D.; Morris, M. A. The morphology and structure of PS-b-P4VP block copolymer films by solvent annealing: effect of the solvent parameter. *Polym. Adv. Technol.* **2011,** *22* (6), 915-923.

52.   *Solid surface energy data for common polymers*; DataPhysics Instruments2006.

53.   Seemann, R.; Herminghaus, S.; Jacobs, K. Gaining control of pattern formation of dewetting liquid films. *J. Phys.: Condens. Matter* **2001,** *13* (21), 4925.

54.   Jacobs, K.; Seemann, R.; Schatz, G.; Herminghaus, S. Growth of Holes in Liquid Films with Partial Slippage. *Langmuir* **1998,** *14*, 4961-4963.

55.   Termonia, Y. Polymer solubility in mixed solvents. *J. Polym. Sci., Part B: Polym. Phys.* **1999,** *37* (19), 2782-2787.

56.   Mueller-Buschbaum, P.; Bauer, E.; Maurer, E.; Nelson, A.; Cubitt, R. Competitive swelling and de-swelling of thin polystyrene films by toluene. *Phys. Status Solidi* **2007,** *1* (2), 68-70.

57.   Zhao, W.; Rafailovich, M.; Sokolov, J.; Fetters, L.; Plano, R.; Sanyal, M.; Sinha, S.; Sauer, B. Wetting properties of thin liquid polyethylene propylene films. *Phys. Rev. Lett.* **1993,** *70* (10), 1453.

58.   Gabriele, S.; Sclavons, S.; Reiter, G.; Damman, P. Disentanglement time of polymers determines the onset of rim instabilities in dewetting. *Phys. Rev. Lett.* **2006,** *96* (15), 156105.

59.   Vilmin, T.; Raphael, E. Dewetting of thin polymer films. *Eur. Phys. J. E* **2006,** *21*, 161-174.

60.   Redon, C.; Brochard-Wyart, F.; Rondelez, F. Dynamics of dewetting. *Phys. Rev. Lett.* **1991,** *66* (6), 715.

61.   Fetzer, R.; Jacobs, K. Slippage of newtonian liquids: Influence on the dynamics of dewetting thin films. *Langmuir* **2007,** *23* (23), 11617-11622.

62.   Neto, C.; Evans, D. R.; Bonaccurso, E.; Butt, H. J.; Craig, V. S. Boundary slip in Newtonian liquids: a review of experimental studies. *Rep. Prog. Phys.* **2005,** *68* (12), 2859.

63.   Lee, T.; Charrault, E.; Neto, C. Interfacial slip on rough, patterned and soft surfaces: A review of experiments and simulations. *Adv. Colloid Interface Sci.* **2014,** *210* (0), 21-38.

64.   Haefner, S.; Benzaquen, M.; Bäumchen, O.; Salez, T.; Peters, R.; McGraw, J. D.; Jacobs, K.; Raphael, E.; Dalnoki-Veress, K. Influence of slip on the Plateau-Rayleigh instability on a fibre. *Nat Commun* **2015,** *6*, 7409.

65.   Choi, S. H.; Newby, B. M. Z. Dynamic contact angle in rim instability of dewetting holes. *J. Chem. Phys.* **2006,** *124* (5), 054702.

CHAPTER 5

Dewetting Poly(4vinylpyridine) Films from Polystyrene

5.1   Introduction

In the past ten years there has been increased understanding of the role of the chain equilibration processes in thin films as a driving force for dewetting.[1-8] Spin-coating induces strongly out-of-equilibrium conformations of the chains and low entanglement density due to the fast evaporation of the solvent. This leads to residual elastic stresses that relax upon annealing, and drastically affect dewetting rate,[4-6] entanglement density and viscosity,[9] and thermal expansion.[2, 10-12] Solvent annealing polymer films has been explored before as an approach alternative to thermal annealing above the glass transition temperature.[10-17] In the previous Chapter, polystyrene films annealed in solvent vapour mixtures were investigated, and it was demonstrated that adding only 2% of a poor solvent for polystyrene, ethanol, to the vapour of a good solvent, toluene, led to extensive viscous fingering, high dewetting velocity, and high contact angles of the dewetted droplets and rims. These effects were attributed to a combined effect of highly enhanced interfacial slip and strong elastic forces within the polymer film.

In this Chapter, the effects of tuning the chemical composition of the vapour environment used for annealing on the dewetting dynamics, mechanism, and morphology of a polymer bilayer are investigated. The studied bilayer is made of a poly(4-vinylpyridine) (P4VP) film on top of a polystyrene (PS) film. As the spreading parameter S for P4VP on PS is negative (-12.8 mN m^{-1}), if the bilayer is thermally annealed above the glass transition temperature T_g of the P4VP (145 °C),[18-20] the top P4VP liquid film dewets from the bottom PS liquid film (both polymers are above T_g) and at the same time layer inversion occurs, because of P4VP's higher surface tension.[18, 20 21-24] Layer inversion becomes obvious when the dewetted P4VP film is selectively dissolved, and the morphology of the bilayer before and after solvent treatment is revealed (Figure 1.9(a)). Co-dewetting of both top and bottom films may also occur if both films in the bilayer are in a liquid state and metastable on their respective substrates. For example, annealing P4VP/PS bilayers in a toluene-ethanol mixture leads to sequential dewetting of both layers, as shown in Figure 1.9(b). In this Chapter, appropriately choosing the vapour composition is demonstrated to prevent layer inversion.

5.2   Materials and Methods

Polystyrene films 98 ± 4 nm thick (PS, M_w = 350 kg mol^{-1}, M_w/M_n = 2.06, Sigma Aldrich) were spin-coated (25 mg mL^{-1} in toluene at 6000 rpm) on prime grade silicon wafers coated with a native oxide layer (1.8 ± 0.2 nm thick). Poly (4-vinylpyridine) films 107 ± 4 nm thick (P4VP, M_w = 60 kg mol^{-1}, Sigma Aldrich) were spin coated (3% wt. in ethanol at 6000 rpm) on top of the PS films. Solvent vapour annealing of films was carried out in a custom-designed Teflon cell (Figure 2.9(a)), which allowed for *in situ* observation of film dewetting by optical microscopy. The employed solvent mixtures were composed of ethanol (99.7%, Merck), acetone (99.8%, Merck) and water (Millipore, resistance = 18.1 MΩ cm), which are entirely miscible and were mixed in the liquid phase in different weight proportions and reach equilibrium with the vapour phase in the experimental cell. For the binary mixtures, the solvent ratios are presented as mole fractions in the vapour phase, using empirical data and literature references (Appendix A). Vapour-liquid equilibrium data for the ternary acetone-ethanol-water mixtures is also tabulated in Appendix A, however the mixture ratios are reported in mass fractions in the liquid phase due to a lack of accurate empirical information in the literature for the mixture ratios used in this study. *In situ* observation of thermally annealed films was conducted by placing the coated substrates on a temperature-controlled hot plate (ATV Technology, Munich, GmBH, model TR-124) under the optical microscope. Image analysis of holes in the P4VP layer prior to coalescence and while they remained within the frame was used to determine hole growth rates during annealing.

Spectroscopic ellipsometry was used to establish film thickness, with measurements over three points on each sample. Atomic force microscopy was used to characterize the cross section of the rims surrounding holes in the P4VP layer and to measure the contact angle of the isolated P4VP droplets on the underlying PS film at the end of dewetting.

5.3   Results

5.3.1   Dewetting and solvent quality

In this Chapter, an investigation of the dewetting of P4VP thin films on top of PS films upon exposure to mixtures of solvent vapours is presented. Heating the bilayers above T_g has been used before to induce dewetting,[19] but extended thermal annealing led also to layer inversion (Figure 1(a)).[18] This is due to the lower surface tension of PS with respect to that of P4VP (Table 5.1), which drives the PS to migrate to the air interface, and to the affinity of P4VP for the polar silicon oxide, which drives the P4VP towards the substrate.

In this study three different solvent vapours and their binary or ternary mixtures were employed to anneal the bilayers. Upon exposure to the solvent vapour environment, the P4VP films immediately changed color due to swelling. Solvent quality for P4VP and PS films was estimated using the polymer-solvent interaction parameter, χ_{p-s} calculated from the Hildebrand solubility parameters (Table 5.1).

Table 5.1: Solubility and surface energy data for the polymers and solvents used in this study. Equation 2 in Appendix B may be used to calculate Hildebrand solubility parameters from Hansen parameters.[26]

Material	Surface energy at 20 °C [27]	Solubility Parameters, MPa$^{1/2}$				Interaction parameters between polymer and solvent (S) [b]	
	γ, mN.m^{-1}	δ_D	δ_H	δ_P	δ	X_{PS-S}	X_{P4VP-S}
Polystyrene (PS)	41	18.0	5.0	5.0	19.0	0.00	1.23
Poly(4-vinylpyridine) (P4VP)	72^a	-	-	-	24.5^{28}	1.33	0.00
Ethanol	22	15.8	8.8	19.4	26.6	2.35	0.18
Acetone	25	15.5	10.4	7.0	20.1	0.05	0.79
Water	73	15.5	16.0	42.4	47.9	34.01	22.3

[a]The empirical data used to calculate P4VP surface energy is tabulated in Appendix B.[29]   [b]Polymer-polymer and polymer-solvent interaction parameters, χ are calculated from the Hildebrand parameters using Equation 3 in Appendix B.

A liquid is a good solvent for a polymer when the Flory-Huggins interaction parameter $\chi < 0.5$, and it swells the polymer film (but does not completely dissolve

it) for values slightly above this.[25] Based on data in Table 5.1, ethanol is a good solvent for P4VP (and a non-solvent for PS), acetone is a poor solvent for P4VP (and a good solvent for PS), and water is a non-solvent for P4VP (and for PS).

5.3.2 Dewetted hole morphology

To understand the role of each solvent (ethanol, acetone and water) in the dewetting of P4VP from the underlying PS film, the bilayer system was annealed in the presence of the saturated vapours of each solvent and their binary mixtures (and one ternary mixture). By varying systemically the weight fraction of each solvent in the liquid phase, the average dewetting rate of holes in the P4VP film versus vapour composition was established.
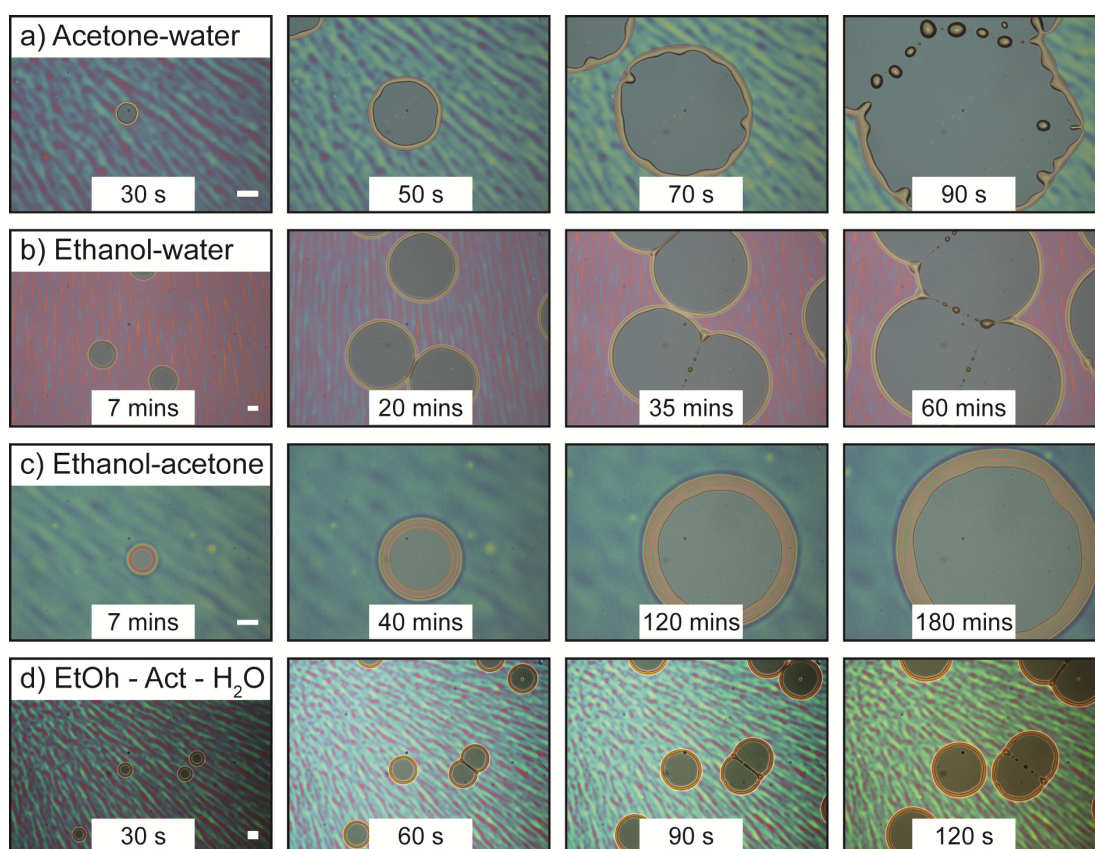

Figure 5.1: Series of time lapse optical micrographs of a dewetting P4VP (107 ± 4 nm)/PS (98 ± 4 nm) bilayer annealed at 23 ± 1°C in vapour mixtures of: (a) acetone – water (90:10), (b) ethanol – water (51:49) and (c) ethanol – acetone (15:85), (d) ethanol – acetone – water (30:30:40 w/w (liq.)). Scale bars = 50 μm.

Figure 5.1 shows a series of time-lapse micrographs of holes nucleating and growing in the P4VP film while annealing in different vapour mixtures. In the nomenclature of the mixtures employed here, e.g. ethanol-water, the first vapour is the better solvent for P4VP, and the second (and third) vapours are increasingly poorer solvents.

Among the binary mixtures tested, the acetone-water vapour mixture induced very fast dewetting, indeed the fastest dewetting rate, as indicated in Figure 5.1 by the time required to reach hole coalescence and break-up of the liquid rims into droplets. In the acetone-water case (Figure 5.1 (a)) hole rims occasionally developed transversal oscillations in thickness and height, leading to the formation of viscous fingers and detachment of internal droplets (Figure 5.1 (a(iv)), due to Rayleigh instability. In the ethanol-water mixture (Figure 5.1 (b)) dewetting was much slower, and then again slower in the ethanol-acetone mixture (Figure 5.1 (c)), with complete dewetting occurring only after several hours. In the latter two cases the rims were regular and stable; the rim width was observed to be the widest in the ethanol-acetone vapour mixture (Figure 5.1 (c)). In the ternary ethanol-acetone-water case, dewetting was slower than in the acetone-water case, but faster than in the other two binary mixtures.

5.3.3   Rates of dewetting in different vapour solvent compositions

Quantitative data on the growth of holes versus composition of the annealing vapour environment is presented in Figure 5.2. Annealing the bilayer in the saturated vapours of pure acetone and pure ethanol resulted in very low average dewetting rates, around 0.05 μm min^{-1}. P4VP films did not dewet upon annealing in pure water vapours within the time frame of the experiment (over 1 hour). In all cases, the solvent mixtures induced faster dewetting than each of the pure solvents (insets in Figure 5.2). The fact that the average growth rate of the holes reached a maximum in mixture of solvent vapours highlights that the two (or three) solvents have different roles in affecting dewetting, as discussed below.

The diameter of the dewetted holes in P4VP films annealed in different vapour environments versus time was fitted by power law models, $D \propto t^{x}$, where the exponent x depended on solvent vapour environment. The trend observed is that the

exponent of the power law was highest in mixtures that contained the largest amounts of poor solvents for P4VP, acetone and water.
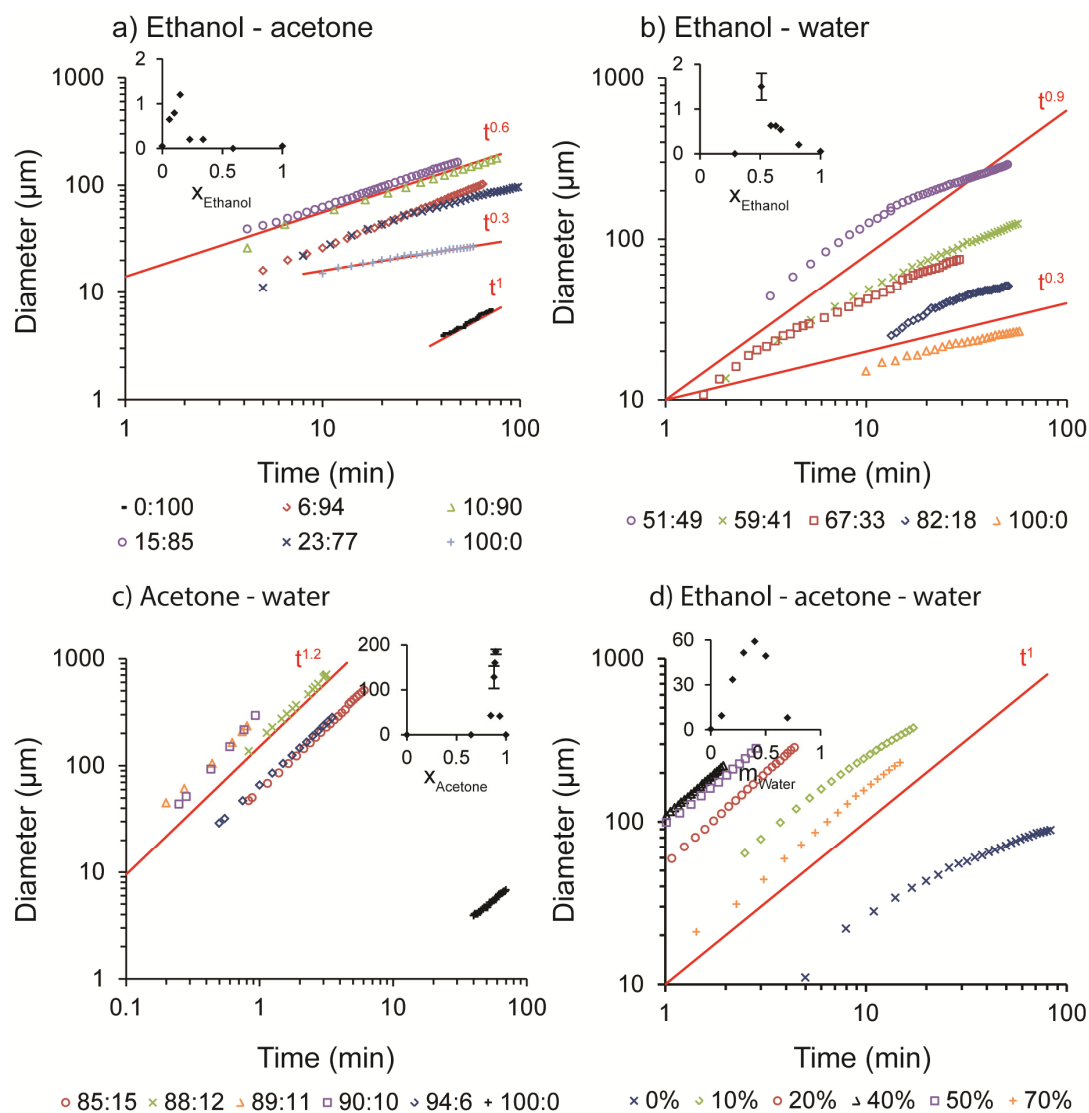
Figure 5.2: Dewetting rate of holes in P4VP films (107 ± 4 nm) on top of PS films (98 ± 4 nm), upon annealing in a vapor mixture of (a) ethanol-acetone, (b) ethanol-water, (c) acetone-water; in (d) ethanol – acetone – water, where increasing water content (% wt.) was added to 50:50 (w/w) ethanol-acetone mixture. Insets: Average hole growth rate (μm min^{-1}) as a function of molar fraction in the vapor of (a) acetone, (b-c) ethanol and (d) mass fraction of water added to a 50:50 (w/w) (liq.) ethanol-acetone mixture. Annealing was carried out at 23 ± 1°C.

For pure acetone, the hole growth was linear with time over the duration of the experiment, with $x \approx 1$ (Figure 5.2(a), black dashes), whereas in pure ethanol vapours the exponent was lower, $x \approx 0.3$ (Figure 5.2(a), grey plus signs). The ethanol-acetone vapour mixtures induced a larger exponent of growth the larger the acetone vapour

mole fraction, with a maximum $x \approx 0.6$ for acetone fraction 77% mol. and above. The fastest average hole growth rate was 1.2 μm min^{-1} at a 15:85 ethanol-acetone vapour phase mole ratio (Figure 5.2(a) purple circles, and inset). The fact that the average dewetting rate reached a maximum at a majority acetone composition suggests that acetone, the poorer solvent of the two, drives the dewetting; a small amount of good solvent ethanol in the annealing environment is sufficient to solubilise the P4VP and allows the flow to occur.

A similar effect was observed in ethanol – water vapour mixtures, where increasing the poor solvent (water) vapour content led to an increase in the hole growth rate, to a maximum of 1.6 μm min^{-1} for a 51:49 vapour phase mole ratio (Figure 5.2(b, purple circles). In all the ethanol-water mixtures, the hole growth profile displayed a clear transition between two regimes: the first faster regime with an exponent of $x \approx 0.9$, followed by a second slower regime with $x \approx 0.3$-0.4. The onset of this transition is due to the increasingly dominating viscous (frictional) forces at the P4VP/PS interface as the rim grows, slowing down P4VP flow.[30-31] The hole diameter at which this transition occurred increased with increasing water content: 35 μm for 18% mol. water, and 160 μm for 49% mol. These observations for water and acetone, that a large content of poor solvent increased the power law exponent and delayed the transition to lower exponents, are evidence that an increasing water and acetone content increased the driving force for dewetting, and overcame interfacial viscous (frictional) forces in the rim.

Annealing in the acetone – water vapour mixtures resulted in a much higher (two orders of magnitude higher) dewetting rate than in the other two binary vapour mixtures: 190 μm min^{-1} for the 90:10 acetone – water mole ratio (Figure 5.2(c), purple squares). This result is remarkable, given that both acetone and water are poor solvents for P4VP. In all the acetone-water mixtures the hole growth profiles followed a purely linear growth $D \propto t^x$, with a high exponent $x \approx 1.2$.

To further explore the significant effect of water on the dewetting rate of the film, increasing amounts of water were added to a mixture of ethanol and acetone (1:1 w/w) (Figure 5.1(d)). Figure 5.2(d) shows that increasing water vapour content up to 40% wt. increased the average hole growth rate by 2 orders of magnitude up to 59 μm min^{-1} (Figure 5.2(d, black triangles)); mostly, in presence of water the hole growth profile followed a single linear growth rate with $x \approx 1$.
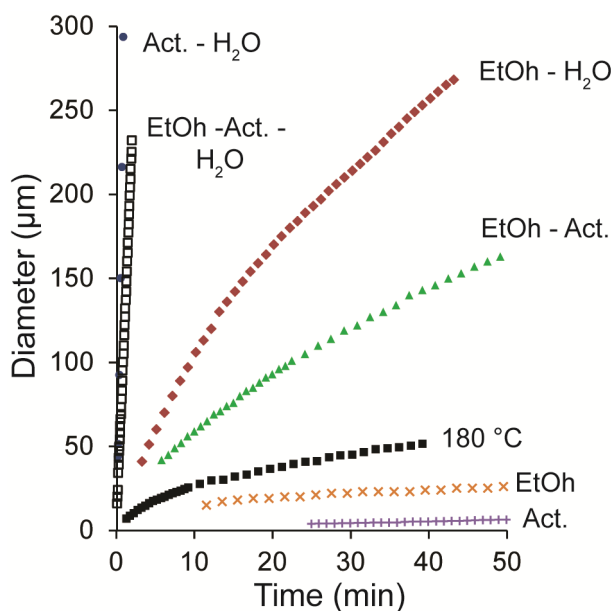
Figure 5.3: Diameter of dewetted holes in P4VP films (107 ± 4 nm) on top of PS films (98 ± 4 nm) versus time, during solvent vapour annealing in 90:10 (mol./mol.) acetone – water vapour (blue circle), 30:30:40 (w/w)(liq.) ethanol – acetone – water (black squares), 51:49 (mol./mol.) ethanol – water (red diamond), 15:85 (mol./mol.) ethanol – acetone (green triangle), pure ethanol (orange cross) and pure acetone (purple plus sign). Thermal annealing at 180 °C is represented by filled black squares.

Figure 5.3 concisely summarises the hole growth profiles of dewetting P4VP films from an underlying PS film during thermal annealing, solvent vapour annealing in pure ethanol and acetone, and in the binary mixtures at the ratios that induced the maximum dewetting rates. Thermal annealing at 180 °C, above the T_g of P4VP (145 °C), resulted in an initial hole growth profile of $D \propto t^{0.67}$, typical of a film experiencing interfacial slip,[31] followed by a second regime (for hole diameter > 20 µm) with $D \propto t$, typical of viscous-dominated flow.

The dependence of the dewetting dynamics on vapour composition is neatly highlighted in Figure 5.3. The clear trends here are that:

-mixtures of solvents induced faster dewetting than pure solvents thermal annealing;

-replacing the poor solvent acetone or the non-solvent water with the better solvent ethanol in the annealing environment reduced the rate of dewetting;

-when acetone was present, mostly the dewetting dynamics followed a single linear trend, with larger exponent the larger the acetone content;

-in the ethanol-water case, increasing the non-solvent water content delayed the transition to a low x exponent to a larger hole diameter.

5.3.4   Rim and droplet geometry

Cross sectional profiles of rims surrounding dewetted holes which were approximately 100 μm in diameter, and of completely dewetted P4VP droplets on the PS substrate were imaged by AFM after annealing in each solvent mixture and thermally annealing at 180 °C (Figure 5.4). As shown in Table 5.2, the thermally annealed P4VP films had the highest contact angle of both rims and droplets, followed by acetone-water, close to ethanol-water mixtures, and the lowest ethanol-acetone. The contact angle of thermally annealed droplets was more difficult to measure due to the effect of partial layer inversion altering the profile at the P4VP-PS contact line and reducing the contact angle, as can be seen from Figure 5.4(b, green profile). In this case the contact angle was deduced by extrapolating the largest gradient measured on the P4VP droplet to the substrate.

Table 5.2: Contact angle of dewetted P4VP droplets and dewetted hole rims of P4VP on top of PS film, upon exposure to different annealing environments, as measured by tapping mode AFM. The error bar on the measurements is ± 1°. The composition ratios refer to the % mol. in the vapour phase.

Annealing environment	Droplet contact angle (°)	Rim contact angle (°)
Thermal at 180 °C	42	30
Acetone - water (90:10)	26	13
Ethanol - water (51:49)	24	13
Ethanol - acetone (15:85)	6	3

The large variation in contact angle of rims and droplets with varying vapour composition is remarkable, as these large variations would usually be induced through substantial modification of the underlying substrate, for example with self-assembled monolayers. The addition of water to the vapour annealing environment led to a 20 degrees increase in the droplet contact angle.
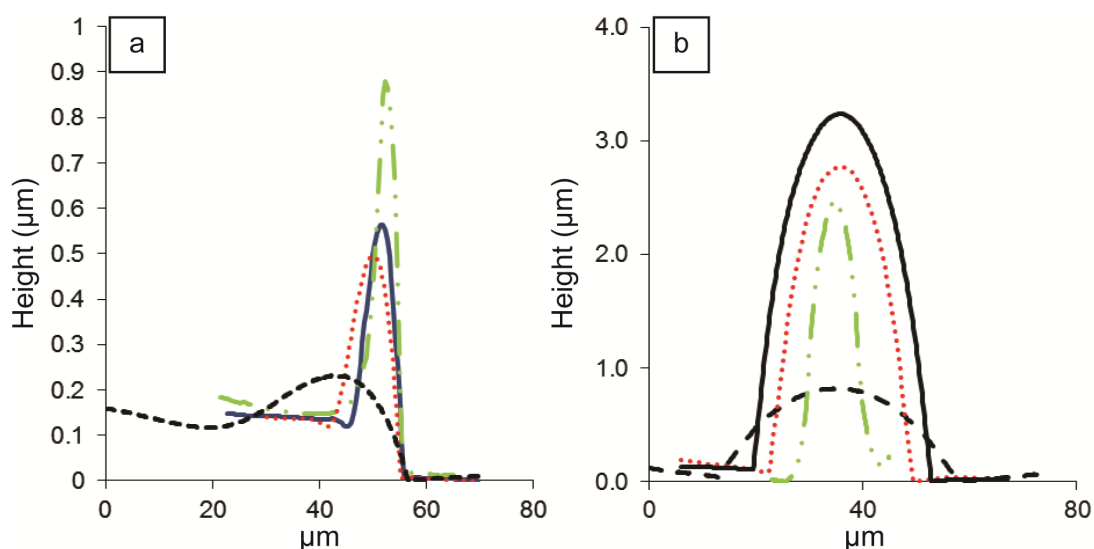
Figure 5.4: (a) AFM cross section of the rim surrounding holes approximately 100 μm in diameter in a dewetting P4VP (107 ± 4 nm) film from a PS (98 ± 4 nm) substrate when annealed in a solvent vapour mixture at 23° ± 1°C composed of acetone–water (90:10) (blue solid line), ethanol-water (51:49) (red dotted line), ethanol-acetone(15:85) (black dashed line) and upon thermal annealing at 180°C (green dashed-dotted line). (b) AFM cross section profiles of droplet for P4VP fully dewetted from the underlying PS. The line styles and colour denote the annealing conditions as they are indicated in (a).

The contact angle of the droplets was made to reversibly change by sequentially changing the saturated vapour environment from a mixture of ethanol-acetone-water to only ethanol-acetone, as illustrated in Figure 5.5. For simplicity, in this figure mixture ratios are reported by mass in the liquid phase. P4VP droplets formed in the vapours of an ethanol – acetone – water (25:25:50) mixture had a contact angle of approximately 26° (Figure 5.5(a)); exposing these droplets to an ethanol – acetone (30:70) mixture led to the droplets spreading on the substrate, obtaining a contact angle close to 4° (same area shown in Figure 5.5(b)). The P4VP droplets returned to the original large contact angle upon reintroduction into an ethanol -acetone-water (25:25:50) saturated vapour environment.

Figure 5.5: Representative optical micrographs illustrating reversible wetting behavior of P4VP droplets on a PS film, acquired after sequentially annealing a P4VP (43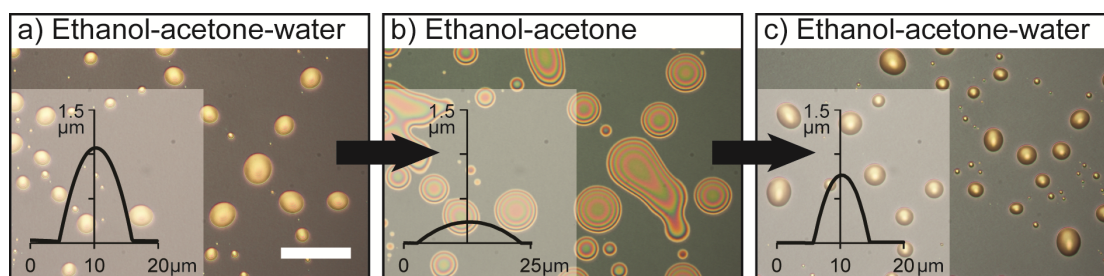 ± 1 nm) / PS (96 ±1 nm) bilayer in (a) 25:25:50 (w/w) ethanol-acetone - water, (b) 50:50 (w/w) ethanol - acetone and (c) 25:25:50 (w/w) ethanol - acetone – water. Scale bar = 50 µm. Insets: representative AFM cross sectional profiles of droplets at each step of annealing.

5.3.5 Thermal annealing and layer inversion

To explore the occurrence of layer inversion in the bilayers, dewetted films were imaged before and after selectively dissolving the P4VP in liquid ethanol (good solvent for P4VP, non-solvent for PS). Figure 5.6 illustrates thermally annealed and solvent annealed P4VP/PS bilayers, which have reached the final stage of dewetting (isolated droplets). The features in parts (b) and (d) remaining after selective dissolution consist of the bottom PS film. In the thermally annealed case, extensive and strong deformation of the PS film was evident after ethanol washing, with indents in the PS films which directly matched the position of the dissolved P4VP droplets and rims, as clear evidence that the dewetting front and droplets in the P4VP layer penetrated into the PS layer underneath. The initially distinct interface between the two polymer films became mixed during thermal annealing, with PS flowing from the hole up inside the P4VP rims and droplets (Figure 5.6 (a-b)). On the other hand, annealing the bilayer in the acetone-water mixture for a prolonged period (17 h) caused little evidence of flow in the PS layer, with only minor, nanoscale rim formation on the PS film (Figure 5.6(c) and (d)), as both solvents are poor solvents for PS.
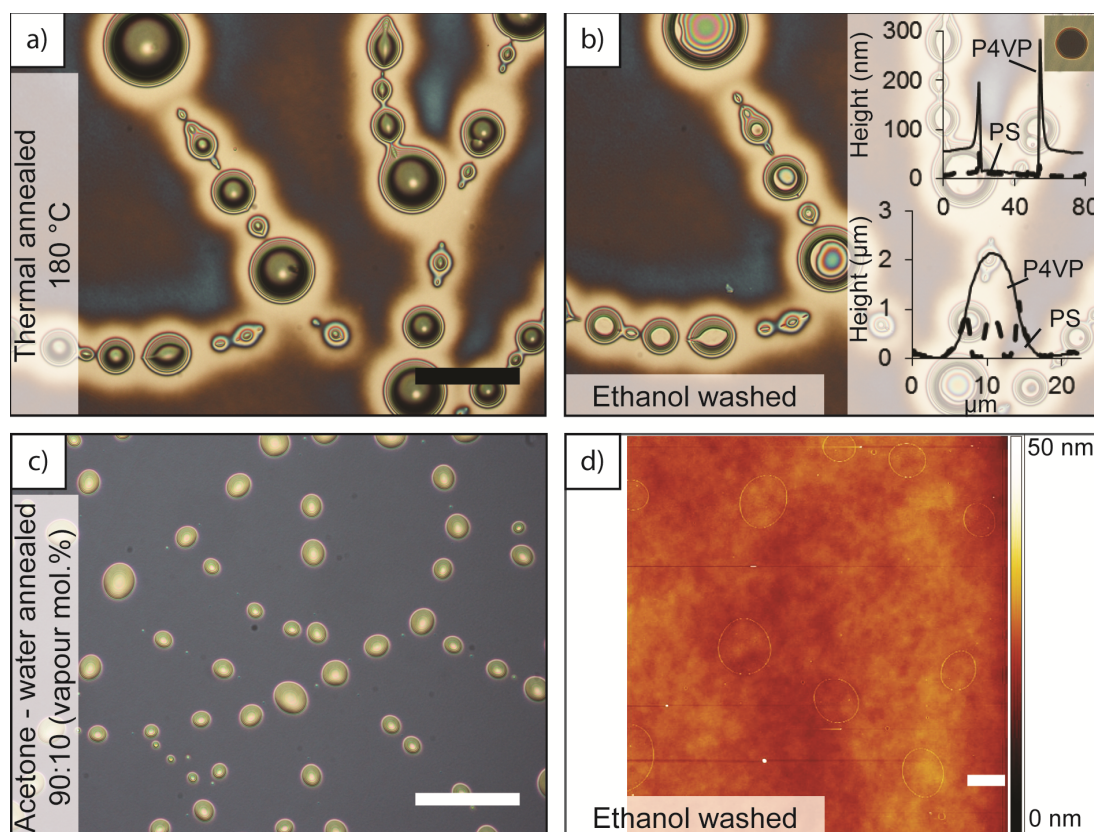
Figure 5.6: Optical micrograph of P4VP (43 ± 1 nm)/PS (96 ± 1 nm) bilayer (a) thermally annealed at 180 °C for 17 h (scale bar = 50 μm). (b) Same area as in (a), after selective dissolution of the P4VP. Inset: AFM cross sections of the rim surrounding a hole in the P4VP layer and a P4VP droplet, dashed lines are the PS film exposed by dissolving the P4VP. (c) Bilayer annealed in acetone-water (90:10) mixture for 17 h at 23 ± 1°C (scale bar = 50 μm). (d) AFM micrograph of the same area as in (c) after selective dissolution of the P4VP with ethanol (scale bar = 10 μm).

5.4   Discussion

The presented dewetting studies demonstrate that a solvent mixture can be tailored to control the dewetting of polymer bilayers. The main conclusion is that the role of each of the three solvent vapours employed in the binary and ternary mixtures may be identified:

- ethanol is the good solvent for P4VP, and acts as the plasticizer, enabling the film to flow by lowering the T_g of the film below room temperature, and if the film is metastable, enables the dewetting to occur. In the absence of ethanol, acetone can take on this role, but to a lesser extent.

- water is a non-solvent for P4VP, and provides a strong driving force for dewetting, by inducing a collapse of the polymer chains into globule conformation.

Acetone can take on this role, but to a lesser extent, and the driving force is stronger the poorer the quality of the solvent for the polymer film.

- acetone is a poor solvent for P4VP and also acts as a lubricant as it preferentially adsorbs to the PS substrate, inducing a lubricated flow (interfacial slip) of the P4VP on the PS.

These conclusions are supported by the discussion points below.

5.4.1   Molecular recoiling and dewetting rates

In a thermally equilibrated polymer melt, the chains adopt a nearly ideal conformation where the radius of gyration R_g scales with N, the degree of polymerization as $R_g = aN^{0.5}$ with a as the monomer size.[32] Spin-casting induces out of equilibrium conformation of the chains, due to the fast solvent evaporation, leading to elastic stresses within the film.[9-10] These stresses are released when the film is heated above the T_g and the chains are permitted to re-arrange. When the magnitude of this force overcomes polymer-substrate attractive interactions and viscous shear forces within the melt, the film is seen to dewet.[1, 6, 33-34 5-6, 10-11, 33, 35-36]

By exposing the P4VP films to mixtures of good and poor solvents, an additional and stronger elastic force was induced, driving the film dewetting. In the experiments presented, polymer collapse predicted in mixtures of good and poor solvents by Monte-Carlo calculations by Magda et al.,[37] but rarely observed in experiments, and then mainly in dilute solution regimes,[36, 38-40] was induced. The collapse of the chains is attributed to the formation of the "onion-like" structure described in Chapter 4, where the good solvent preferentially solvates and plasticizes the chains, and the poor solvent forms an outer layer, which overall drives the collapse towards a globular conformation. This was demonstrated in the previous Chapter where this chain collapse induced by good-poor solvent mixtures resulted in elastic stresses that led to the fast dewetting of polystyrene films from a silicon substrate, a system that does not dewet during thermal annealing.

In this Chapter, the presence of water vapour, a non-solvent for P4VP, and acetone vapour, also a non-solvent, substantially increased the dewetting rate by inducing molecular recoiling and reducing the P4VP viscosity as a consequence of the collapsed and less entangled conformation of the P4VP chains. Both acetone and water acted as drivers for dewetting, as long as sufficient amounts of plasticizer (good solvent ethanol, or to a lesser extent acetone) were present, making the film

sufficiently mobile. The maximum dewetting rates were achieved usually with high content (49 -85 mol%) of dewetting drivers. In the acetone-water mixture, acetone acted as a poor plasticizer, as a driver with water, and as a lubricant, as discussed below.

The increase in the driving force for dewetting due to water and acetone was demonstrated not only through both a dramatic increase in dewetting rate, but also through an increase in the exponent x, approaching unity, of the hole growth profile $D \propto t^x$ (Figure 5.2), and a delay of the transition to slower dewetting. In the case of acetone, an additional specific increase in the dewetting rate was established, which is explained as inducing lubricated flow (or interfacial slip), as detailed below.

5.4.2   Interfacial slip

The dewetting dynamics of polymer melts from solid or highly viscous substrates is well understood.[30, 41-42] Upon thermal annealing, the P4VP/PS bilayer respected the expected trends (initial growth as $D \propto t^{2/3}$, regime dominated by interfacial slip, followed $D \propto t$ characteristic of viscous flow).[30, 41] The transition between these two regimes is clearly visible in Figure 5.3 (square symbols). The intermixing of the two liquid films and layer inversion did not alter the dewetting dynamics significantly, as previously observed.[18]

However, in the presence of solvent vapour in the annealing environment, and especially in the presence of acetone, the dewetting dynamics changed significantly. It is believed that the flow in the presence of acetone resembles the flow observed in rheological studies of polymer solutions, where the dispersed phase (polymer) is depleted from the solid boundary due to steric, hydrodynamic and chemical forces.[43] The enrichment in solvent near the wall means that the flow of the fluid is facilitated by the lubrication effect. Three important indicators that a lubricated interfacial flow is occurring due to acetone enrichment at the P4VP/PS interface are identified. The observable effects of this resemble the effect due to interfacial slip in polymer melts flowing over solid surfaces, and so the same terminology is used. The first indicator of slip in the presence of acetone is that the dewetting rate in the acetone-water mixture is 2 orders of magnitude higher than in the ethanol-water mixture, despite ethanol being a better solvent for P4VP. The second indicator is that, in all cases where acetone is present, either the dewetting dynamics follows a single straight line

with high exponent x (= 0.9 - 1.2) in the power law fit of the diameter vs time curve; or the transition between a high exponent in the power law fit (x = 0.9) and a low exponent (x = 0.3) occurs at larger hole diameters than in the absence of acetone. The third indicator is that in the acetone-water case viscous fingering in the hole rims occurs. Acetone adsorption at the PS interface can be expected, as acetone is a good solvent for PS, and so adsorption at the PS interface is favored. These indicators suggest that acetone adsorbs at the P4VP/PS interface, and lubricates the flow, which effectively allows the P4VP to slip more readily on the PS. The higher the acetone content, the larger the slip.

In the only mixture where acetone is missing, the ethanol-water vapour environment, the transition from a slip-dominated dewetting regime to a viscous regime is also visible (Figure 4(b)). As discussed earlier, increasing the concentration of water increased the hole diameter at which the transition between slip-dominated flow to viscous flow occurred. Water does not have a strong affinity for PS, but its effect on the collapse of the P4VP chains, as described above, is sufficient to decreases the entanglement and adhesion of P4VP with the bottom PS chains, and this facilitates the flow dramatically.

5.4.3   Annealing in a ternary mixture of ethanol-acetone-water

Further evidence of the effect of water vapour in the environment surrounding a solvated P4VP chain is provided in Figure 5.2(d), where the addition of water to a 50:50 (w/w) ethanol –acetone liquid mixture resulted in: an increase in the average dewetting rate, a transition from a two-regime growth profile to a single regime with constant dewetting rate, as well as narrowing of the rims surrounding the holes in the P4VP film and higher aspect ratio droplets (Figure 5.5). In this case, the separate roles of the three solvents are observable: ethanol swells P4VP, acting as the plasticizer; water and acetone both act as drivers for dewetting, water being a stronger driver; and acetone preferentially adsorbs to the PS interface, facilitating slip. Annealing in this three-solvent mixture serves to illustrate the importance of controlling the ambient humidity conditions during film preparation and solvent annealing as the addition of even small amounts of water leads to a distinct variation in film dewetting.

5.4.4   Spreading parameter and surface energy

The droplet contact angle presented in Figure 5.4(b) and Table 5.2, and the reversibility of P4VP droplet wetting on the PS substrate illustrated in Figure 5.5 are indicative of the dependency of spreading parameter for P4VP on PS on the surrounding solvent environment. Specifically, the spreading parameter decreased dramatically when water was added to the annealing environment (contact angle increase from 6 to 24 degrees), and the effect could be reversed by removing water. Again, this effect is interpreted as a result of the reorganization of the polymer chains within the plasticized film into a more collapsed globule conformation, due to the presence of the strong non-solvent water replacing the better solvents ethanol and acetone.

5.4.5   Suppression of layer inversion and multilayer dewetting

Figure 5.6 shows that the use of a solvent vapour annealing environment, where the solvents do not sufficiently plasticize the PS film, prevents layer inversion and multilayer co-dewetting. During thermal annealing a substantial intermixing of the two films, approximately half of the height of P4VP droplets (approx. 1 μm) was observed (Figure 5.6(b)). This deformation was reduced to around 50 nm after annealing in a saturated acetone – water environment for the same extended period of time (17 h). As P4VP films of this thickness completely dewetted within 10 minutes of vapour annealing, the effect of layer inversion is negligible.

While dewetting of multiple polymer layers at the same time may be desirable for some applications where access to three different surface chemistries is beneficial, it is possible to suppress this phenomenon as demonstrated here. The use of toluene-ethanol mixtures to induce dewetting of PS films from silicon substrates was the subject of the previous Chapter. The same solvent mixture could be used to induce dewetting of a P4VP film from a PS coated silicon substrate. By removing toluene, and using only poor and non-solvents for PS in the annealing mixture, the ability of PS to dewet from the silicon substrate was suppressed (Figure 5.6(c)).

5.4.6   Alternative materials, architectures and applications

Solvent mixture annealing of polymer films provides a route towards the production of patterns and architectures in a simple and scalable manner. Chemical heterogeneity on a surface may be obtained by simply altering the solvents used for dewetting. For example, annealing in a saturated environment of a FC-72 – ethanol mixture, where these immiscible solvents were not mixed in the liquid phase, may dewet a highly hydrophobic PTFE coating. As shown in Figure 5.7, the dewetting of PTFE leads to the formation of holes in the PTFE film and ultimately the self-assembly of PTFE droplets on the substrate. The hydrophobic nature of PTFE is demonstrated by the preferential adsorption of water on the PS substrate instead of the PTFE bumps (Figure 5.7(b)).
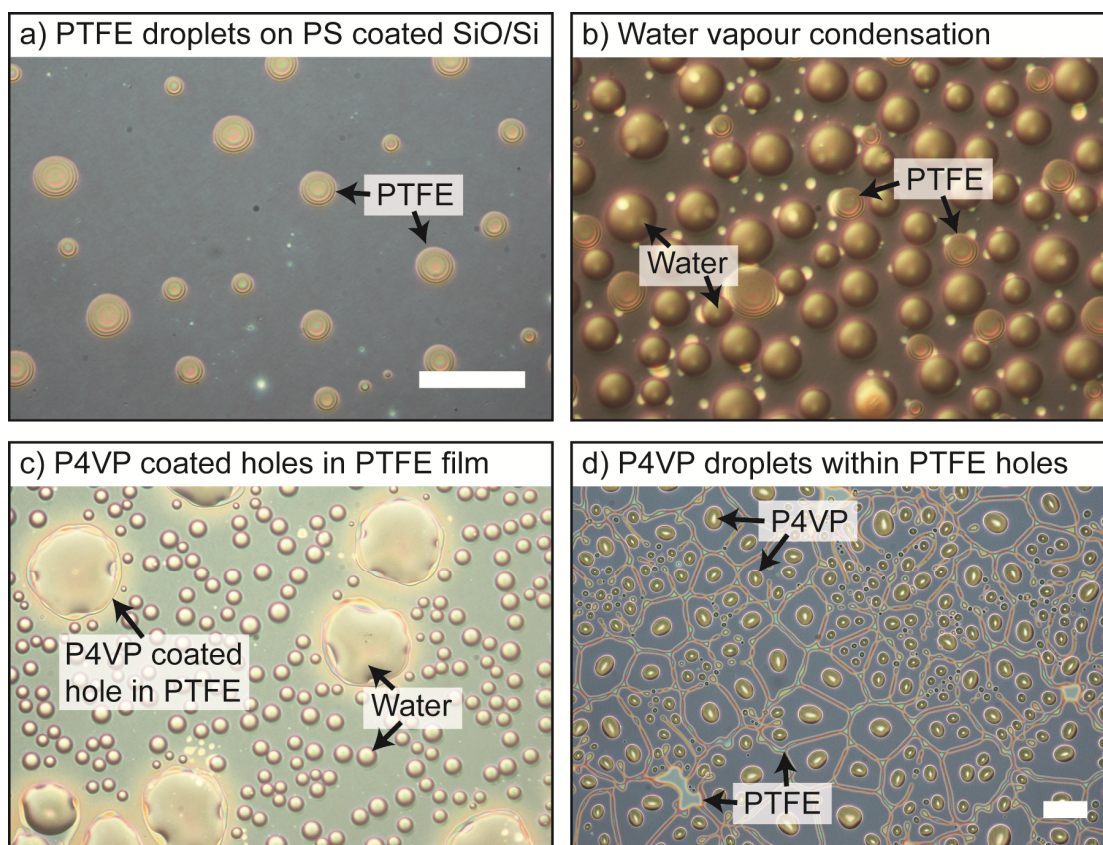
Figure 5.7: (a) PTFE droplets on PS film after annealing a PTFE (120 nm) /PS (100 nm) bilayer on SiO/Si in FC-72 – ethanol mixed vapour environment. (b) Water vapour displaying preferential adsorption on a PS surface with PTFE bumps. (c) P4VP coated holes in a PTFE film, initiated by FC-72 – ethanol mixture annealing, coated on a PS film on SiO/Si with preferential adsorption of water vapour (d) Dewetting P4VP within PTFE holes in a similar sample to (c) by annealing in the saturated vapours of a 90:10 (mol./mol.)(vap.) acetone-water mixture. Scale bars = 50 μm.

The production of polymeric wells, from the nano to the micro scale, by controlling the end point of PTFE film dewetting, provides an interesting system for study. By taking advantage of the non-wetting nature of the PTFE film, it is possible to alter the chemistry within the holes by casting other polymers from solution. A high wettability contrast is shown in Figure 5.7(c), where P4VP was spin coated from an ethanol solution onto the dewetted PTFE film with holes exposing the PS substrate.

The wettability contrast between the three polymers in this system, P4VP within the dewetted holes on PTFE on a PS substrate, can be further utilised to create even more complex structures. By annealing this system in the saturated vapours of a 90:10 acetone-water mixture, the P4VP film dewets from the PTFE rims surrounding its enclosure and from the PS substrate resulting in a P4VP droplets resting within the well structures (Figure 5.7(d)). Surfaces with such complex combinations of chemistry and topography, including the multilayer-dewetting system described earlier provide opportunities for the development of many technologies.

5.5   Conclusions

In this Chapter, the effect of the composition of solvent vapour environments on the dewetting of polymer films bilayers is demonstrated. The effect of solvent vapour annealing with binary and ternary mixtures of ethanol, acetone and water on the dewetting rate and morphologies of P4VP film cast on PS films was investigated. Tuning of the composition of the vapour mixtures provided control over the average dewetting rate and dewetting dynamics of the P4VP film. By vapour mole fraction, acetone – water (90:10), ethanol – water (51:49) and ethanol-acetone (15:85) were found to be the binary compositions that led to the highest dewetting rates. The role of each solvent in the mixture was identified clearly: ethanol (the good solvent for P4VP) acts to solubilise the polymer chains, and acetone and water (poor and non-solvent for P4VP) act to collapse them, inducing the molecular recoiling which drives dewetting. Furthermore, acetone in the annealing mixture induced significant interfacial slip due to the affinity of acetone for the underlying PS film.

Building on these experiments and the work presented in the Chapter 4, evidence was provided for molecular recoiling as the primary mechanism driving film dewetting. Films that were annealed in the solvent mixtures containing water, displayed a contact angle of both the rims and droplets that was approximately 4 times greater than the films annealed without water present. This is attributed to the transition of the polymer chains from an extended to a globular conformation in an acetone-water and ethanol-water mixtures, due to the strong preferential adsorption of the higher quality solvent. This behavior, predicted by Shultz and Flory,[44] and explored by numerical simulations by Magda *et al.*[37] for dilute polymer solutions, is obvious in polymer melts. The correct choice of solvent in the annealing environment for polymer bilayers mitigates the ability of the substrate polymer to flow thereby reducing layer inversion as well as inhibiting dewetting of the bottom film from the solid substrate.

Annealing polymer films in the vapour of solvent mixtures controls dewetting, including rates and aspect ratio of dewetted droplets, without the need for substrate modification.

5.6   References

1.   Reiter, G. Dewetting of highly elastic thin polymer films. *Phys. Rev. Lett.* **2001,** *87* (18), 186101.

2.   Reiter, G.; de Gennes, P. G. Spin-cast, thin, glassy polymer films: Highly metastable forms of matter. *Eur. Phys. J. E* **2001,** *6* (1), 25-28.

3.   Bollinne, C.; Cuenot, S.; Nysten, B.; Jonas, A. M. Spinodal-like dewetting of thermodynamically-stable thin polymer films. *Eur. Phys. J. E* **2003,** *12* (3), 389-396.

4.   Yang, M.; Hou, S.; Chang, Y.; Yang, A. M. Molecular recoiling in polymer thin film dewetting. *Phys. Rev. Lett.* **2006,** *96* (6), 066105.

5.   Reiter, G.; Hamieh, M.; Damman, P.; Sclavons, S.; Gabriele, S.; Vilmin, T.; Raphaël, E. Residual stresses in thin polymer films cause rupture and dominate early stages of dewetting. *Nat. Mater.* **2005,** *4* (10), 754-758.

6.   Damman, P.; Gabriele, S.; Coppée, S.; Desprez, S.; Villers, D.; Vilmin, T.; Raphaël, E.; Hamieh, M.; Al Akhrass, S.; Reiter, G. Relaxation of residual stress and reentanglement of polymers in spin-coated films. *Phys. Rev. Lett.* **2007,** *99* (3), 036101.

7.   Thomas, K. R.; Steiner, U. Direct stress measurements in thin polymer films. *Soft Matter* **2011,** *7*, 7839.

8.   Ediger, M. D.; Forrest, J. A. Dynamics near Free Surfaces and the Glass Transition in Thin Polymer Films: A View to the Future. *Macromolecules* **2014,** *47* (2), 471-478.

9.   Barbero, D. R.; Steiner, U. Nonequilibrium Polymer Rheology in Spin-Cast Films. *Phys. Rev. Lett.* **2009,** *102* (24), 248303.

10.   Thomas, K. R.; Chenneviere, A.; Reiter, G.; Steiner, U. Nonequilibrium behavior of thin polymer films. *Phys. Rev. E* **2011,** *83* (2), 021804.

11.   Clough, A.; Chowdhury, M.; Jahanshahi, K.; Reiter, G.; Tsui, O. K. C. Swelling with a Near-Θ Solvent as a Means to Modify the Properties of Polymer Thin Films. *Macromolecules* **2012,** *45* (15), 6196-6200.

12.   Raegen, A.; Chowdhury, M.; Calers, C.; Schmatulla, A.; Steiner, U.; Reiter, G. Aging of thin polymer films cast from a near-theta solvent. *Phys. Rev. Lett.* **2010,** *105* (22), 227801.

13.   Lee, S. H.; Yoo, P. J.; Kwon, S. J.; Lee, H. H. Solvent-driven dewetting and rim instability. *J. Chem. Phys.* **2004,** *121* (9), 4346-4351.

14.   Xu, L.; Shi, T.; An, L. Nonsolvent-Induced Dewetting of Thin Polymer Films. *Langmuir* **2007,** *23* (18), 9282-9286.

15.   Xu, L.; Shi, T.; An, L. The dewetting dynamics of the polymer thin film by solvent annealing. *J. Chem. Phys.* **2008,** *129* (4), 044904.

16.   Burtovyy, R.; Luzinov, I. Reversibility of pH-Induced Dewetting of Poly(vinyl pyridine) Thin Films on Silicon Oxide Substrate. *Langmuir* **2008,** *24* (11), 5903-5910.

17.   Xu, L.; Sharma, A.; Joo, S. W. Dewetting of stable thin polymer films induced by a poor solvent: role of polar interactions. *Macromolecules* **2012,** *45* (16), 6628-6633.

18.   Thickett, S. C.; Harris, A.; Neto, C. Interplay between Dewetting and Layer Inversion in Poly (4-vinylpyridine)/Polystyrene Bilayers. *Langmuir* **2010,** *26* (20), 15989-15999.

19.   Thickett, S. C.; Neto, C.; Harris, A. T. Biomimetic surface coatings for atmospheric water capture prepared by dewetting of polymer films. *Adv. Mater.* **2011,** *23* (32), 3718-3722.

20.   Lambooy, P.; Phelan, K.; Haugg, O.; Krausch, G. Dewetting at the liquid-liquid interface. *Phys. Rev. Lett.* **1996,** *76* (7), 1110.

21.   Wang, C.; Krausch, G.; Geoghegan, M. Dewetting at a polymer-polymer interface: film thickness dependence. *Langmuir* **2001,** *17* (20), 6269-6274.

22. Kang, H.; Lee, S. H.; Kim, S.; Char, K. Dewetting and layer inversion of inverted PVP/PS bilayer films. *Macromolecules* **2003,** *36* (23), 8579-8583.

23. Steiner, U.; Klein, J.; Fetters, L. J. Surface phase inversion in finite-sized binary mixtures. *Phys. Rev. Lett.* **1994,** *72* (10), 1498-1501.

24. Yoon, B. K.; Huh, J.; Kim, H. C.; Hong, J. M.; Park, C. Ordered patterns of microimprinted bilayer polymer films with controlled dewetting and layer inversion. *Macromolecules* **2006,** *39* (3), 901-903.

25. Barton, A. F. *Handbook of polymer-liquid interaction parameters and solubility parameters*; CRC press, 1990.

26. Hansen, C. M. *Hansen solubility parameters: a user's handbook*; CRC press, 2007.

27. Instruments, D. Solid surface energy data (SFE) for common polymers. **2006**.

28. Brandrup, J.; Immergut, E. H.; Grulke, E. A.; Abe, A.; Bloch, D. R. *Polymer handbook*; Wiley New York, 1999; Vol. 89.

29. Sauer, B. B.; Dee, G. T. Surface tension and melt cohesive energy density of polymer melts including high melting and high glass transition polymers. *Macromolecules* **2002,** *35* (18), 7024-7030.

30. Brochard-Wyart, F.; de Gennes, P. G.; Hervert, H.; Redon, C. Wetting and slippage of polymer melts on semi-ideal surfaces. *Langmuir* **1994,** *10* (5), 1566-1572.

31. Bäumchen, O.; Jacobs, K. Slip effects in polymer thin films. *J. Phys.: Condens. Matter* **2010,** *22* (3), 033102.

32. de Gennes, P. G. *Scaling concepts in polymer physics*; Cornell University Press, 1979.

33. Gabriele, S.; Sclavons, S.; Reiter, G.; Damman, P. Disentanglement time of polymers determines the onset of rim instabilities in dewetting. *Phys. Rev. Lett.* **2006,** *96* (15), 156105.

34. Reiter, G.; Hamieh, M.; Damman, P.; Sclavons, S.; Gabriele, S.; Vilmin, T.; Raphaël, E. Residual stresses in thin polymer films cause rupture and dominate early stages of dewetting. *Nat, Mater.* **2005,** *4* (10), 754-758.

35. Vilmin, T.; Raphael, E. Dewetting of thin polymer films. *Eur. Phys. J. E* **2006,** *21*, 161-174.

36. Grosberg, A. Y.; Khokhlov, A. *Statistical Physics of Macromolecules*; American Institute of Physics: New York, 1994. p 1-144.

37. Magda, J.; Fredrickson, G.; Larson, R.; Helfand, E. Dimensions of a polymer chain in a mixed solvent. *Macromolecules* **1988,** *21* (3), 726-732.

38.   Baysal, B. M.; Karasz, F. E. Coil - Globule Collapse in Flexible Macromolecules. *Macromol. Theory Simul.* **2003,** *12* (9), 627-646.

39.   Nakata, M. Coil-globule transition of poly (methyl methacrylate) in a mixed solvent. *Phys. Rev. E* **1995,** *51* (6), 5770.

40.   Auroy, P.; Auvray, L. Collapse-stretching transition for polymer brushes: preferential solvation. *Macromolecules* **1992,** *25* (16), 4134-4141.

41.   Jacobs, K.; Seemann, R.; Schatz, G.; Herminghaus, S. Growth of Holes in Liquid Films with Partial Slippage. *Langmuir* **1998,** *14*, 4961-4963.

42.   Reiter, G.; Sharma, A. Auto-optimization of Dewetting Rates by Rim Instabilities in Slipping Polymer Films. *Phys. Rev. Lett.* **2001,** *87* (16), 166103.

43.   Barnes, H. A. A review of the slip (wall depletion) of polymer solutions, emulsions and particle suspensions in viscometers: its cause, character, and cure. *J. Nonnewton. Fluid Mech.* **1995,** *56* (3), 221-251.

44.   Shultz, A.; Flory, P. Polymer chain dimensions in mixed - solvent media. *J. Polym. Sci.* **1955,** *15* (79), 231-242.

CHAPTER 6

Patterned Polymer Coatings for
Water Harvesting

6.1   Introduction

The World Economic Forum, in its latest annual risk report, has listed water crises as the leading global potential risk in terms of impact and eighth in terms of likelihood.[1] In a recent study on monthly global water scarcity, Mekonnen and Hoekstra concluded that two thirds of the global population (4 billion people) live under severe water scarcity for at least one month of the year. Furthermore, half a billion people face year-round severe water scarcity. [2] Harvesting fresh water from atmospheric humidity and fog is a method that has been previously proposed[3] and could be utilised as a source of freshwater for regions around the world without ready access to surface and groundwater resources.

The fog harvesting adaptation of the Namib Desert *Physosterna cribripes* beetle, previously misidentified as the *stenocara gracipiles*,[4-5] is a chemically and topographically micro-patterned surface structure on its *elytra* which facilitates the collection of drinking water from the fog-laden winds in its otherwise arid surroundings.[4, 6] Initial experimental simulation of a biomimetically patterned surface was conducted by Parker and Lawrence by embedding hydrophilic glass beads within a hydrophobic wax.[6] Since 2001 the concept of a chemically and topographically patterned surface for water collection has been repeatedly studied; with the use of different materials, including the introduction of surface roughening to promote superhydrophobicity,[7] alternative pattern geometries and different material fabrication processes.[8-14] Most recently, compound surfaces utilising the wettability adaptations of multiple plant and animal species have been produced and shown to be extremely effective at condensing and collecting water from a humid environment.[15] In this Chapter, chemically and topographically patterned surfaces, prepared by polymer film dewetting, are used for atmospheric water harvesting. Previous collaborative work between the Neto group and the Laboratory for Sustainable Technology on this front was published in 2011.[16]

The solvent vapour annealing techniques developed in the previous Chapters, which initiate the dewetting process and maximize the dewetting rate of polymer films, were used to produce patterned surface coatings with physical and chemical topography on multiple length scales. The water harvesting performance of these

coatings prepared on copper substrates was compared against flat, hydrophobic polystyrene using the apparatus described in Chapter 3.

6.2   Materials and Methods

Polystyrene films (PS, M_w = 350 kg mol^{-1}) that were approximately 110 nm in thickness were prepared by dip coating from solution (2% wt. in toluene, extracted at 120 mm min^{-1}) onto flat copper sheets and the outer surface of copper tubes, 10 mm in diameter. Poly (4-vinylpyridine) films (P4VP, M_w = 60 kg mol^{-1}) of varying thicknesses, 5 - 900 nm, were subsequently cast onto this substrate from solution (0.5 – 7.5% wt. in ethanol). To induce dewetting, the bilayer films were placed in a saturated vapor environment of a mixture of acetone and water in a 9:1 vapour mole ratio. *In situ* observation of the dewetting of P4VP60k on the PS350k coated copper sheets was conducted by optical microscopy with the custom-designed Teflon cell shown in Figure 2.9(a).

Prior to film preparation, the copper samples were thoroughly cleaned with metal polish and wiped with petroleum spirit. This was followed by sonication in ethanol and blow-drying with pure nitrogen. Spectroscopic ellipsometry was used to establish film thickness; with measurements over three points on each sample. Atomic force microscopy was used to analyse the distribution and contact angle of the isolated P4VP bumps on the substrate at the end of dewetting.

The condensation studies, carried out by Mr Jun Hong, a summer intern under my supervision, were conducted by cooling the coated copper sheets on a temperature controlled Peltier plate (TE technology Inc. CP-031 with controller TC 48-20) in a controlled humidity environment under the optical microscope. The growth and coalescence of water droplets on the surfaces was captured in a series of time lapse micrographs and the droplet diameters were analysed using the manufacturer's software. Contact angle goniometry was used to characterise the wettability and the roll-off angle of the patterned surface coatings on the copper substrate.

Water collection was conducted in a custom-built humidity chamber containing four copper tubes (inset of Figure 3.2(b)). The outer surface of these copper tubes

was coated with the patterned polymers, prepared by solvent vapour induced dewetting, as well as plain polystyrene as a reference. The coatings were uniformly cooled by flowing ethanol from a temperature-controlled reservoir through the tubes, facilitating the condensation of water on the coated surface. Water droplets that rolled off the tubes were collected in plastic trays situated directly below. The mass of collected water was measured at multiple intervals throughout the experimental period following the onset of steady state condensation. The steady state water collection efficiency (units of mL m^{-2} h^{-1}) of each coating was directly compared and presented herein.

6.3   Results and Discussion

6.3.1   Polymer film dewetting

Chemically and topographically patterned surfaces were prepared from copper substrates coated with polymer bilayer films. The top layer of the film was poly (4-vinylpyridine) (P4VP), a hydrophilic polymer, which was cast on a hydrophobic polystyrene (PS) film. Annealing the polymer coated copper substrates in a saturated vapour environment of a liquid mixture of acetone and water (90:10 mol./mol.) induced dewetting which was characterized by the nucleation of holes in the P4VP film, followed by the growth and coalescence of these holes and ultimately the breakdown of the P4VP hexagonal network leading to isolated bumps on the PS substrate. Varying the thickness of the spin-cast P4VP film by 2 orders of magnitude led to a variation in the size and distribution of the produced dewetted bumps.

Figure 6.1 illustrates the dewetting process of P4VP films of different initial thicknesses to produce isolated P4VP droplets of different diameter and distribution; (a) micro patterns (b) macro patterns and (c) nano patterns. The distribution, diameter and contact angle of the isolated P4VP bumps is summarized in Table 6.1. As the initial P4VP film thickness was increased, the diameter of the P4VP bumps increased and the nucleation density of holes in the P4VP film were found to decrease, leading to greater spacing between the final isolated bumps, with the macro-pattern consisting, on average, of 5 bumps mm^{-2} (Table 6.1). The P4VP bumps on the nano patterned surface were too small to be distinguished by optical

microscopy. Therefore atomic force microscopy was used to visualise the pattern structure (Figure 6.1(c)) and Figure 6.2.
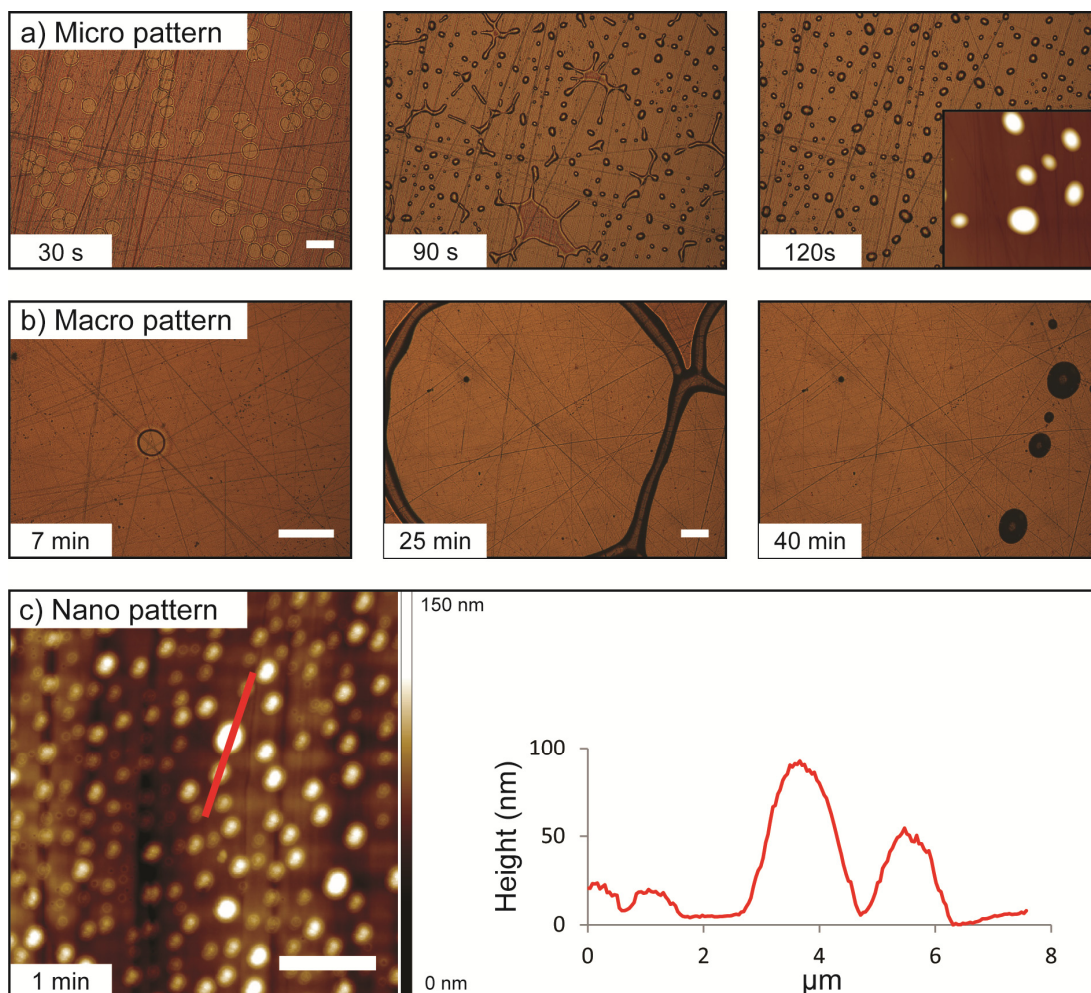

Figure 6.1: Time lapse series of optical micrographs of a P4VP film dewetting from a PS coated (110 nm) copper substrate while annealing in an acetone-water (90:10 mol./mol. (vap)) mixture to produce a (a) micro patterned surface coating (scale bar = 50 μm). Inset: AFM micrograph (100 x 100 μm^2) of P4VP bumps on PS background. Colour scale = 2.5 μm (b) Macro patterned surface coating (scale bar = 200 μm) and (c) AFM micrograph of the nano patterned surface coating (scale bar = 5 μm) with a cross sectional profile showing the height of the P4VP bumps on the PS substrate.

The contact angle of the droplets was measured using AFM at the contact line with the PS substrate. As shown in Chapter 5, an average droplet contact angle of 25° for bilayer P4VP/PS films annealed in the saturated vapours of an acetone-water (90:10 mol./mol.) mixture was expected. The contact angle of P4VP bumps on the macro and micro patterned surfaces were similar to this value; however the contact angle of bumps on the nano-pattern were significantly lower than expected. This

behaviour is attributed to the onset of intermixing and partial layer inversion of the P4VP/PS bilayer film,[17-19] the effect of which is negligible in the patterns with larger sized bumps.

Table 6.1: Average distribution, diameter and contact angle of P4VP bumps on a PS coated copper substrate after annealing in a 70:30 (w/w) acetone-water mixture.

Pattern	P4VP film thickness (nm)	Distribution (mm^{-2})	Average diameter (μm)	Average height [a] (nm)	Contact angle (°)	P4VP surface area coverage (%)
Nano	7.3 ± 0.2	136 000 ± 11 000	0.9 ± 0.1	44 ± 10	10 ± 1	8.7 ± 1.5
Micro	86.2 ± 0.2	793 ± 102	11.9 ± 0.1	1300 ± 100	24 ± 1	8.8 ± 1.1
Macro	821.4 ± 8.6	5 ± 1	82 ± 9	9000 ± 2000	26 ± 3	2.6 ± 0.7

[a] The P4VP bumps were assumed to be spherical caps and therefore the average P4VP bump height, h_{bump}, was calculated from the contact angle of the P4VP bumps on PS, $\theta_{P4VP/PS}$ and the average radius of the bumps, r_{bump} by the relationship: $h = r_{bump} \tan(\theta_{P4VP/PS})$.

As shown in Figure 6.2 and highlighted by the cross sectional profile of a single P4VP bump in the inset to this Figure, the nano scale bumps present an edge all around the base at a height of approximately 20 nm, which, from previous work by Thickett, Harris and Neto, is believed to be the intermixing and creeping of PS onto the P4VP bump due to the higher surface energy of P4VP with respect to PS.[18] The effect of this creeping behaviour of the PS film is to reduce the contact angle of the droplets at the contact line with the substrate.
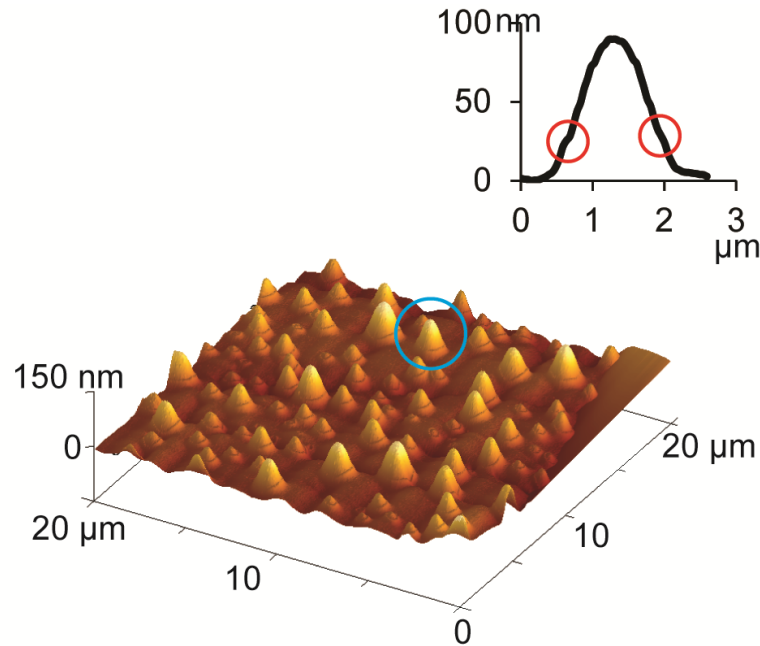
Figure 6.2: AFM micrograph of a nano-pattern of P4VP bumps on PS. This image illustrates layer inversion of the PS film onto the P4VP bumps. Inset: cross sectional profile of the indicated bump. The red circles mark the presence of the PS edge on the P4VP bump.

6.3.2   Surface wettability

The wettability of the surface coatings was characterised using contact angle goniometry and the results are presented in Table 6.2. The contact angle of a 5 µL sessile water droplet on the patterned surface increased as a function of pattern size. The contact angle of the three patterns was similar, increasing from 81° for the nano pattern to 85° for the micro pattern and 88° for the macro pattern. This wettability behaviour can be explained by reference to the Cassie-Baxter relationship for heterogeneous surfaces[20]

$$\cos \theta_e^{CB} = f_1 \cos \theta_1 + f_2 \cos \theta_2 \tag{6.1}$$

where the contact angle of each region of fraction f_i of the total surface area within the droplet footprint or, as more recently suggested, localised to the contact liquid-substrate contact line,[21] is averaged to provide the expected contact angle of a water droplet on this surface. The projected surface area coverage, neglecting bump surface area, of hydrophilic P4VP in the nano and micro patterned surfaces is approximately 9% and for the macro patterned surface the area coverage is reduced to 2.6%. Using Equation 6.1 to calculate the contact angle of water on these surfaces

yields 88° for the nano and micro patterns and 91° on the macro pattern. These values overestimate the hydrophobicity of the surface from experimental measurements. As the water droplets are much larger in size than single P4VP droplets, the contact line is expected to lie along multiple hydrophilic domains, which would decrease the contact angle of the droplets accounting for the discrepancy between the measured and calculated values. Furthermore, the calculation doesn't account for the increase in hydrophilic surface area related to the curvature of the P4VP bumps.

Table 6.2: Wettability of the patterned coatings and the hydrophobic polystyrene reference coating on a copper substrate

Pattern	Sessile contact angle (°)[a]	Advancing contact angle (hysteresis (°))[b]	V_{crit} for droplet sliding at 45° (µL) (hysteresis (°))
Nano	81 ± 1	90 ± 1 (28)	15.0 (25)
Micro	85 ± 2	91 ± 1 (26)	15.0 (25)
Macro	88 ± 3	95 ± 2 (36)	12.5 (27)
Flat PS	92 ± 1	102 ± 3 (18)	7.5 (19)
Flat P4VP	45 ± 1	71 ± 3 (61)	-

[a]Sessile drop contact contact angle of water on the surfaces was measured using a 5 µL water droplet.
[a]Advancing and receding contact angles obtained by volume addition-subtraction method by sequentially adding and removing 10 µL to a 5 µL at 0.5 µL s^{-1}.

The contact angle hysteresis, the resistance to droplet sliding due to surface interactions,[22] was measured using the two methods discussed in Section 2.4: a volume addition- subtraction method on a horizontal surface was used to provide information on the advancing and receding contact angles, and secondly, by the shape of a water droplet with the minimum critical volume to slide down a surface inclined at 45° (Table 6.2). The results for the two types of measurement align well except for results from the macro-pattern. Due to the contact angle hysteresis of 36° on the macro pattern, this surface was expected to have the highest critical volume, $V_{crit,}$ for droplet sliding on the inclined surface. In fact, the critical volume for droplet sliding, V_{crit} =12.5µL on the macro pattern was lower than V_{crit} = 15.0 µL on the other patterns but greater than 7.5 µL on the flat polystyrene surface. This high value for the contact angle hysteresis of water droplets on the macro patterned surface was attributed to the large size and sparse distribution of the P4VP bumps on the PS

background. A receding droplet experiences significant distortion of the contact line due to the chemical contrast between the hydrophilic bumps and the hydrophobic background. The significant distance between each bump resulted in very obvious 'stick-slip' motion, which was largely absent on the patterned surfaces with numerous hydrophilic bumps. During droplet sliding, the mass and momentum of the droplet is able to overcome the adhesive forces of the sparsely distributed hydrophilic bumps on the macro patterned surface. On the other hand, the large density of bumps on the nano and micro patterned surfaces results in numerous pinning points and a larger droplet mass is required to initiate sliding.

6.3.3 Condensation on surface coatings

Water vapour condensation experiments were conducted in a custom designed humidifying chamber on the patterned and plain PS and P4VP coated copper sheet with *in situ* optical microscopy. Figure 6.3 summarises the results by showing a series of optical micrographs of water condensation on the patterned and plain surface coatings over time. Figure 6.3(a) illustrates the condensation of water vapour on polystyrene coated copper, the reference system, highlighting the characteristic formation of water droplets with a uniformly circular geometry and a semi-spherical appearance that minimises surface area. In comparison, water droplets nucleating and growing on a hydrophilic P4VP surface are irregular in shape as they readily spread on the higher energy surface, eventually forming thermally insulating films of water on the surface (Figure 6.3(b)). On both of these surfaces, the water droplets grow in size and coalesce with adjacent droplets over the course of the experiment. The centre of mass of the large droplets that result from coalescence events is located approximately at the centre of mass of the original 'parent' droplets, highlighted in red (Figure 6.3(a)), prior to coalescence. According to Beysens, the condensation rate plateaus beyond a surface area coverage of 55% due to competition between droplet growth decreasing the free surface area and droplet coalescence increasing the free surface area available for the nucleation of new families of droplets.[23]

In Figure 6.3(d) and (e), the P4VP bumps are labelled in the first micrograph of the series to distinguish them from the water droplets and a selection of bumps is highlighted in blue throughout the series. The relative position of the bumps remains constant throughout the series. Figure 6.3(c) and (d), show the condensation

behaviour of water on the nano and micro patterns respectively, illustrating the hydrophilic nature of these surfaces (higher nucleation density of water droplets) and the size of the growing water droplets relative to the dimensions of the hydrophilic P4VP bumps. Water condensation on these two patterned surfaces preferentially occurs on the hydrophilic bumps, with coalescence occurring when adjacent droplets are large enough to span the hydrophobic region between them. This leads to water droplets becoming 'pinned' to the bumps, resulting in the contact line becoming deformed as indicated in Figure 6.3(c) and (d).
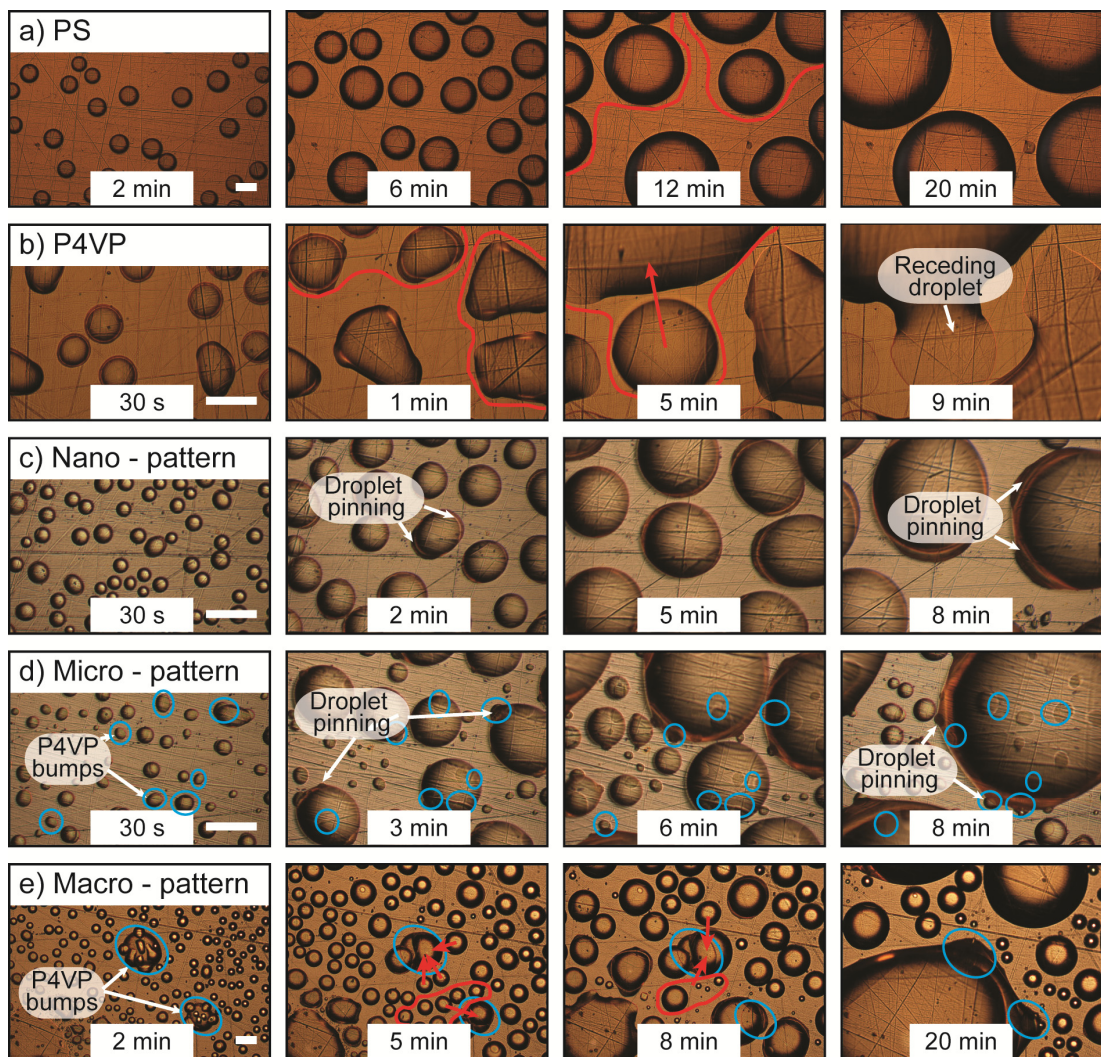
Figure 6.3: OM time lapse of water condensation at T_{amb} = 20.3 ± 0.5°C, 85.3 ± 3.6%RH and surface subcooling ΔT = 3.0 ± 0.5°C on (a) polystyrene (b) poly(4vinylpyridine), (c) nano patterned (d) micro patterned and (e) macro patterned surface coatings on flat copper substrates. Scale bars = 50 μm. A selection of P4VP bumps, where visible, is highlighted in blue. Droplets encircled in red lines coalesce together over the period of the experiment; with the red arrows indicating the direction of motion of the centre of mass of these droplets during coalescence.

The behaviour of water droplets condensing on the macro-patterned surface (Figure 6.3(e)) displays the characteristics of condensation on the hydrophilic P4VP coating as well as the polystyrene coating due to the relatively small, 3%, hydrophilic surface area coverage of the P4VP bumps. At 2 min, small, uniformly circular water droplets nucleate on the hydrophobic PS, and irregularly shaped droplets can be clearly seen to condense on the hydrophilic P4VP bumps. The P4VP bumps are large enough to support the nucleation of multiple water droplets which are visible in the micrographs until 8 min into the experiment. In contrast to droplet coalescence on the plain PS and P4VP surfaces, water droplets that coalesce on the patterned surfaces have a preferred direction of motion towards the water droplets on the hydrophilic P4VP bumps, indicated by red arrows on the micrograph series. This directional coalescence behaviour enhances the condensation rate by providing free surface area for further droplet nucleation,[24-26] in contrast to the flat polystyrene surface where the nucleation of new droplet 'families' slows down over time. Furthermore, the preferential nature of the coalescence is expected to enhance the rate at which water droplets approach V_{crit} to slide off the P4VP bumps.

The water condensation behaviour on each patterned surface was qualitatively analysed at 85.3 ± 3.6 %RH, for subcooling temperature ΔT, the difference in temperature between the ambient and the surface, between 3 – 10 °C. The values of ΔT were chosen to illustrate the effect of surface wettability on the condensation rate. It was hypothesised that the influence of surface wettability on condensation rate would diminish as ΔT was increased at a constant ambient humidity level. As shown in Figure 2.10, a sensor placed 10 mm vertically above the coated copper sample measured the ambient temperature and relative humidity and the surface temperature was measured by a thermocouple located on the upper surface of the thermoelectric Peltier plate. The results for the condensation behaviour of water vapour on the patterned and plain surface coatings subcooled by 2 – 5 °C are presented in Figure 6.4. The results are reported in percentage area coverage (Figure 6.4(a)), and the calculated volume (Figure 6.4(b)), of water condensed on each surface. The condensation behaviour of water vapour on the macro patterned surface was not analysed as the large size of the bumps prevented accurate analysis of the water droplets forming on the bump surface due to the depth of field provided by the microscope lens at the required magnification for image analysis.
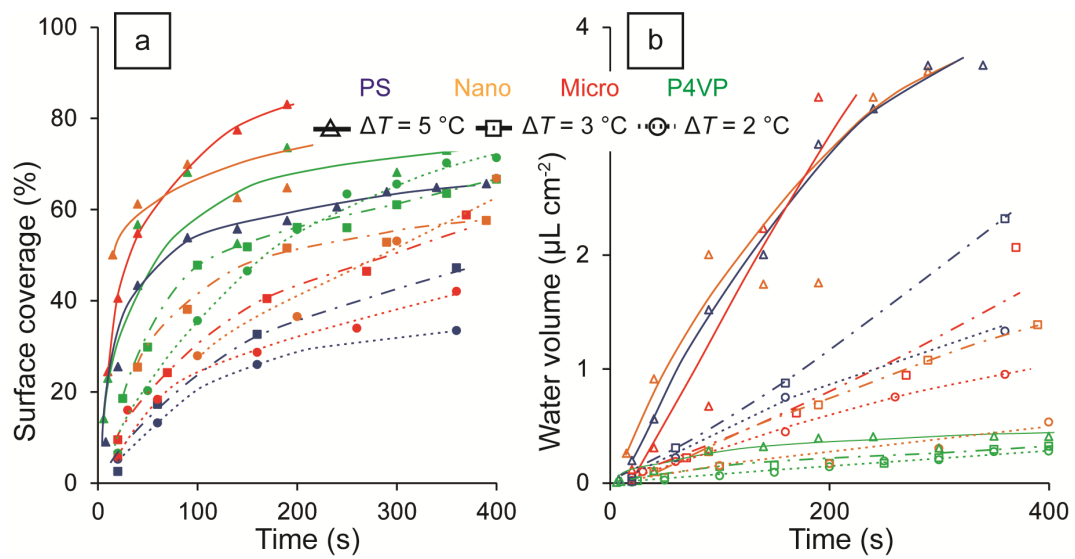
Figure 6.4: (a) Percentage surface area coverage of condensed water over time and (b) volume of water condensed over time, normalised against the coated surface area, on the PS (blue), Nano patterned (orange), micro patterned (red) and P4VP (green) coated copper sheets at $T_{amb} = 18.4 \pm 2.0°C$ and $85.3 \pm 3.6\%RH$ for surface subcooled by: $\Delta T = 5.0 \pm 0.5°C$, $\Delta T = 3.0 \pm 0.5°C$ (dot-dash lines), $\Delta T = 2.0 \pm 0.5 °C$ (dotted lines). The fluctuations in the amount of water condensed on the surfaces at $\Delta T = 5 °C$ is attributed to the coalescence of large (by area) droplets that enter and exit the image frame. Smooth curves have been superimposed onto the plots to guide the eye along the trends.

From the surface area coverage plot, Figure 6.4(a), it is clear that the rate of water condensation onto the surface is related to the surface wettability. At all subcooling temperatures the flat P4VP films (shown in green) have a higher proportion of the surface covered in water than the flat PS film coatings (blue). This can be attributed to the high nucleation rate and spreading of water droplets during growth and coalescence on the hydrophilic surface. The condensation rates on the nano and micro patterned surfaces, orange and red lines in Figure 6.4(a) respectively, were in between those of the flat P4VP and PS for experiments when the surfaces were subcooled by 2 °C and 3 °C, with the nano pattern exhibiting a faster condensation rate, as expected due to the higher wettability of this surface, demonstrated by the contact angle data in Table 6.2. At $\Delta T = 5 °C$, the condensation rate, based on the surface area coverage with water, becomes indistinguishable between the P4VP coating and the two patterned surfaces, and in fact, the initial condensation rate, up to 50 s into the experiment, for all surface coatings is very similar. This indicates that as ΔT is increased, the effect on surface wettability in promoting condensation is reduced and all surfaces nucleate water droplets at similar rates, irrespective of surface wettability.

The volume of water condensed on each surface, plotted in Figure 6.4(b), was calculated using Equation 2.13, from the wettability information obtained by contact angle goniometry (Table 6.2) and an estimation of droplet radii from the surface area of the condensed water droplets by image analysis. As expected, the rate of increase in water volume on all of the surfaces increased as the level of subcooling was increased from 2 °C to 5 °C. However, due to the low contact angle of water on the P4VP coated copper, the volume of water condensed on the surface is lower at all subcooling temperatures than on the patterned and PS surface coatings. At $\Delta T = 2$ °C, there is a clear difference between the rate of increase in water volume on the PS coating (blue, dotted line), which had the highest rate, the micro pattern (red, dotted line) and the nano pattern (yellow, dotted line), with the slowest rate of water volume collection. This trend is attributed to two effects:

- The high contact angle of water on the PS surfaces results in a higher volume for a given surface area coverage by a water droplet

-The high nucleation rate of droplets on the patterned surfaces, due to the spacing of the hydrophilic bumps, resulted in many droplets that are smaller in size at equivalent times to the low number of droplets that nucleate and grow on the PS surface.

As the subcooling is increased, the difference in the rate of water condensation on the patterned surfaces and PS, in terms of volume, diminishes. At $\Delta T = 3$ °C (dash- dotted lines), the two patterned surfaces have very similar condensation rates, which are lower than the rate of condensation on PS, and at $\Delta T = 5$ °C, the rate of increase in the volume of condensed water vapour on the two patterned surfaces and PS is similar and considered within the experimental error introduced due to rapid condensation and the movement of water droplets into and out of the frames being analysed due to coalescence.

Water condensation measurements provide insight into the preliminary stages of water harvesting, namely droplet nucleation and early growth and coalescence. However, within the time frames of these experiments, water droplets do not approach the critical volumes necessary to slide off the surfaces (Table 6.2). Furthermore, the method by which the droplet volume is calculated results in an underestimation of the volume of water droplets that are partially present within the image frame, as the visible droplet area is converted into an equivalent radius from which the volume is calculated. This underestimation of droplet volume is greater for

droplets with a lower contact angle. Due to these sources of error, the trends in condensation rate have been qualitatively analysed and it is possible to conclude that at low subcooling, surface wettability affects the rate of condensation, with a patterned surface with hydrophilic domains or a uniformly hydrophilic surface condensing more water in terms of surface area coverage. However, when the condensation rate is considered in terms of water volume, then the condensation rate on the hydrophobic polystyrene coating is consistently higher at all subcooling temperatures. Finally, water vapour preferentially condenses on the hydrophilic bumps on the patterned surfaces and it was observed that either the spacing, or the size of the bumps, influences the nucleation density of water on these surfaces, with the micro patterned surface which has larger bumps and a lower distribution density, condensing more water by volume than the nano patterned surface coating.

6.3.4   Water harvesting efficiency of patterned coatings

By combining the condensation rate measurements from Figure 6.4 and the observations of the nucleation and growth behaviour of water droplets on the macro patterned surface (Figure 6.3(e)), it was predicted that the sparse distribution (5 mm^{-2}) of the large hydrophilic bumps, coupled with the movement of water droplets towards the bumps during coalescence, would result in a high water collection efficiency at low subcooling temperatures on this surface. This hypothesis was tested by simultaneously comparing the steady state water collection rate over a period of 6 h of the three patterned coatings and the plain PS coating in the custom built water collection apparatus described in Chapter 3, at ΔT = 3 - 10 °C and 95 %RH. The results of these experiments are illustrated in Figure 6.5.

At ΔT = 3 °C (Figure 6.5, blue bars), the patterned surfaces were observed to be more efficient at water collection than the flat hydrophobic PS coated surface, with the macro pattern harvesting the most water (14.5 ± 1.1 mL m^{-2} h^{-1}). The nano and micro patterns performed similarly, collecting 11.3 ± 1.1 mL m^{-2} h^{-1} and 12.6 ± 1.1 mL m^{-2} h^{-1} respectively and the PS coating produced a water collection rate of 9.2 ± 1.1 mL m^{-2} h^{-1}. When the subcooling was increased to ΔT = 5 °C (red bars), the PS coating was observed to be the most efficient at water harvesting, collecting 38.1 ± 2.7 mL m^{-2} h^{-1} compared with a collection rate of 32.5 ± 2.7 mL m^{-2} h^{-1} by the macro pattern coating. Finally, the four surface coatings were subcooled by 10 °C

(green bars), whereby the water collection rate of all of the surface coatings approximately increased by an order of two over the collection rate at $\Delta T = 5$ °C. However at these condensation conditions, the difference in water harvesting between the four coatings over the course of the experiment was within the error margin of the experimental apparatus (± 8.5 °C).
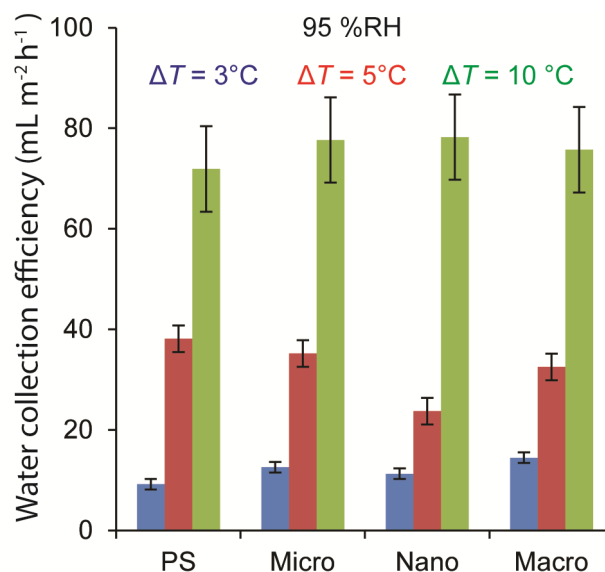

Figure 6.5: Water collection efficiency of the PS, nano patterned, micro patterned and macro patterned surface coatings on copper tubes at 95 ± 3.6%RH, $T_{amb} = 22.1 \pm 1.0$ °C and $\Delta T = 3$ °C (blue), $\Delta T = 5$ °C (red) and $\Delta T = 10$ °C (green) for a collection time of approximately 6 h.

6.3.5   Deterioration of the coating

The micro and macro patterned surface coatings on copper tubes were inspected by optical microscopy before and after long periods of water collection (20 h). The macro patterns were observed to physically disintegrate and artefacts, attributed to swelling, emerged on the P4VP bumps (Figure 6.6(b)). The wettability contrast between the P4VP bumps and the PS background, described in Section 6.3.3, is shown Figure 6.6(a) and (d). At the conclusion of the water collection experiments lasting approximately 20 h, water droplets condensing on the PS background were observed to have lost the typical uniformly circular geometry; instead they spread on the surface with irregular contact lines, typical of water condensing on a hydrophilic surface. This change in the surface wettability is illustrated in Figure 6.6(c) and (f) and is attributed to the swelling of the P4VP

bumps by the condensing water droplets, which induced thin residues of the hydrophilic polymer to leach onto the PS background during coalescence and while sliding off the surface.
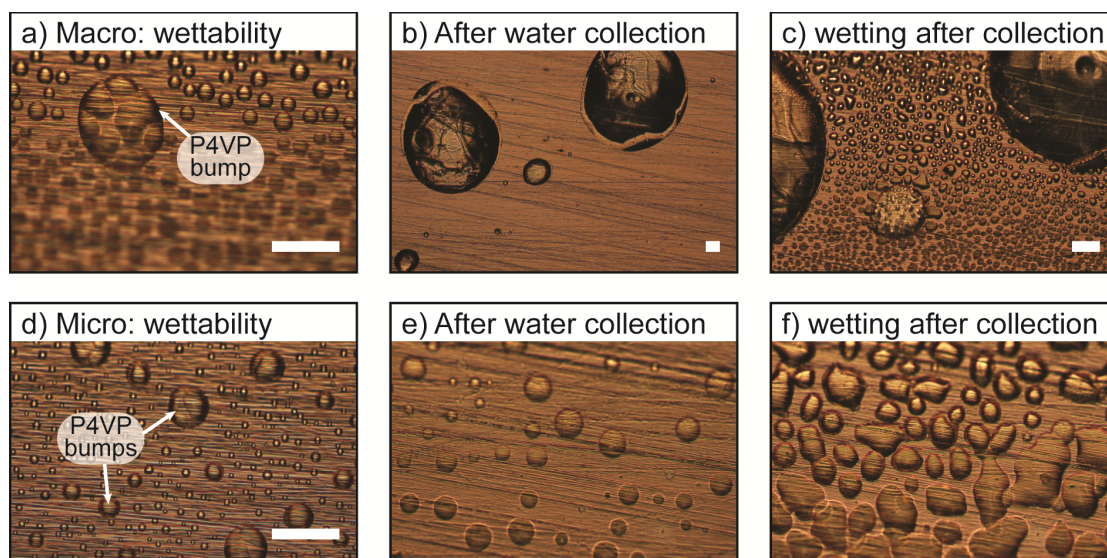

Figure 6.6: Optical micrographs of the patterned coatings on the copper tubes showing physical and chemical deterioration of (a-c) macro and (d-f) micro patterned surfaces following condensation activity. Scale bars = 50 μm

6.4 Other Surface Coatings for Water Harvesting

Other surfaces and surface preparation methods were briefly pursued for the purposes of understanding the fundamental principles behind the effects of wettability contrast and topography on water harvesting efficiency, but were not further developed. These interesting materials and techniques are worthwhile of future investigation and are presented in the optical micrographs in Figure 6.7(a-c), with the first column illustrating the surface structure and the second column demonstrating the behaviour of condensing water droplets on the surface. A coating composed of a phase separated blend of P4VP/PS spin cast from a common solvent (chloroform) onto a silicon substrate demonstrates the separation of the effects of surface topography from the wettability contrast provided by the two polymers, as the isolated P4VP domains are only slightly depressed, approximately 70 nm by the AFM cross section in Figure 6.7(a), below the level of the surrounding PS matrix.

The nucleation of water droplets clearly occurs on the flat hydrophilic P4VP patches, as shown in the second column of part (a).
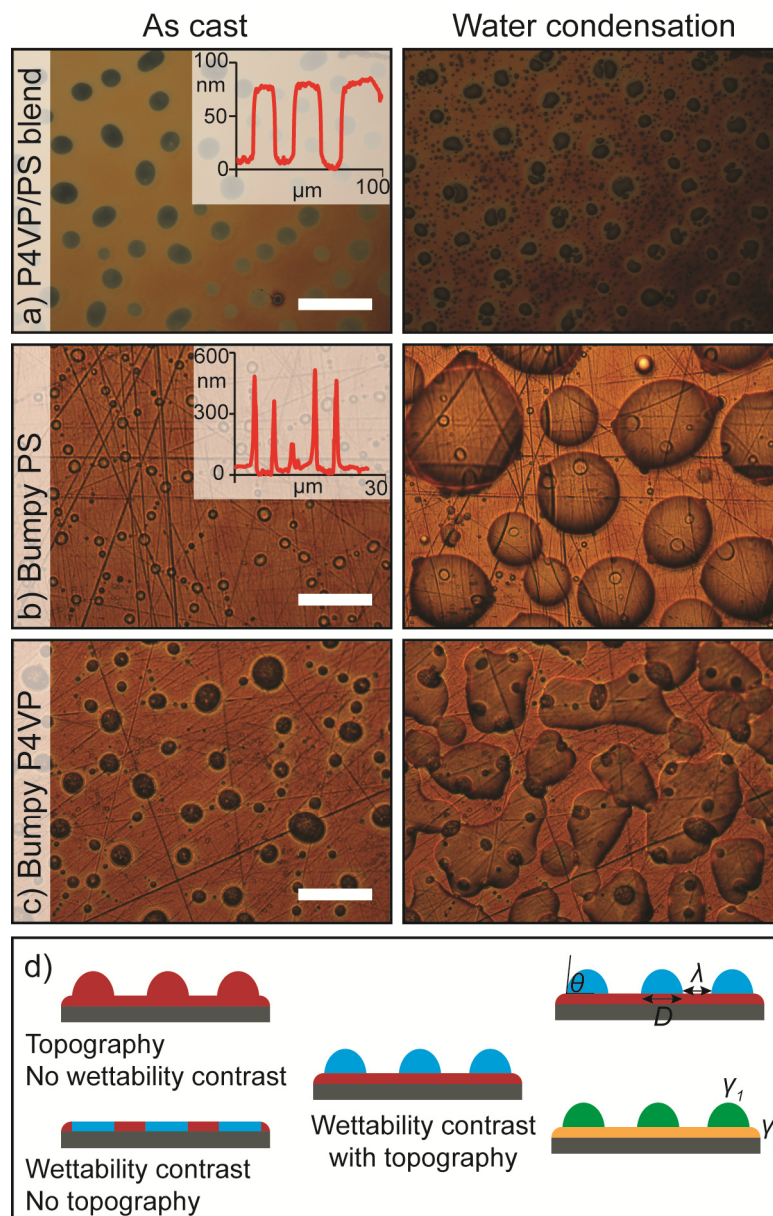
Figure 6.7: Optical micrographs of (a) P4VP/PS blend cast on a silicon substrate demonstrating phase separation of the two polymers and preferential condensation of water within the P4VP domains. (b) Topographically patterned polystyrene coating on copper and water condensation on the surface demonstrating pinning behaviour. (c) Topographically patterned P4VP on copper (d) Schematic drawings of the combinations of topography, chemistry and geometry of patterned surface coatings to optimise water harvesting. Scale bars = 50 μm.

The bumpy P4VP and PS surfaces, Figure 6.7(c) and (d) were prepared in order to demonstrate the water collection performance of topographically patterned

surfaces without chemical heterogeneity. The bumpy P4VP surface was prepared in two steps: i) dewetting PS films on the copper substrate using the annealing procedure presented in Chapter 4, to produce isolated PS bumps; ii) dip coating this dewetted layer with a film of P4VP. The water droplets condensing on this surface have an irregular contact line; from direct inspection of the condensation process (data not shown), it could be seen that the water droplets nucleated first on the bumps. The water droplets are flatter in shape than on the PS surface, and spread to a low contact angle, typical of water droplets on a hydrophilic surface (Figure 6.7(b)). The bumpy PS surface was prepared by the same method as the bumpy P4VP, however a further dip coating step was integrated to coat the P4VP layer with a PS film. Unfortunately, following this final step, the bumps were observed to become concave (inset AFM cross section to Figure 6.7(b)), which was attributed to the final dip coating procedure 'washing out' the initial PS bumps, further research in this direction was therefore suspended.

The schematic illustrations in Figure 6.7(d) demonstrate the concept behind the surfaces presented in this Section as well as suggestions for future parametric studies of surfaces designed for atmospheric water harvesting. The combination of chemical contrast (surface energy γ), topography (diameter D and contact angle θ) and pattern geometry (separation between features λ) can be optimised to maximise the water harvesting capability of a polymeric coating. Furthermore, the surface wettability may be tuned and tailored for the condensation of other solvents for the potential application of volatile solvent recycling.

6.5   Conclusions

Patterned surface coatings on nano, micro and macro scales were prepared by solvent vapour annealing, in an acetone-water mixture, P4VP/PS bilayer films that were coated on copper substrates, which led to the P4VP film dewetting and forming P4VP bumps on the PS substrate. Different pattern sizes were obtained by varying the P4VP film thickness, with average bump diameters varying between $0.9 - 82$ μm, and an average bump density on the PS background of $5 - 136\,000$ mm^{-2}.

The surface wettability was characterised by contact angle goniometry and a direct correlation was found between the proportion of hydrophobic surface area on the patterned surfaces and the contact angle of a sessile water droplet, in line with the Cassie Baxter theory for heterogeneous surfaces. The contact angle hysteresis increased as the hydrophilic area fraction increased, due to the adsorption of the water droplets to the hydrophilic domains. The macro patterned surface coating was found to have the lowest critical volume for detachment (12.5 µL) of the three patterns tested, measured for water droplets sliding down a 45° incline; this was attributed to the low surface coverage of hydrophilic bumps resulting in fewer pinning points for water droplets.

The water condensation and collection rates for the patterned surfaces was analysed and compared against the performance of a flat hydrophobic PS coating. Condensation rate analysis by optical microscopy in a humidified environment revealed the importance of surface wettability as the subcooling, ΔT, was decreased. The patterned surfaces, with hydrophilic domains, displayed faster condensation rates, measured in terms of surface area coverage, than the flat hydrophobic PS surfaces. As the temperature differential was increased, the benefit of surface hydrophilicity was less important as the condensation rates became increasingly similar on all of the surfaces, as expected.[23] A similar trend was observed when the volume of water condensing on the surfaces was calculated. In this case, the patterned surfaces and the PS surface condensed water at similar rates at $\Delta T = 5$ °C.

When ΔT was decreased, the PS surface displayed the fastest condensation rate, by volume, followed by the micro patterned surface. The enhanced condensation rate of the micro patterned surface, compared with the nano patterned surface was attributed to the size and distribution of the P4VP bumps. The high nucleation density of water droplets on the nano patterned surface was observed to negatively impact the droplet growth rate over time. The flat P4VP film had the slowest condensation rate by volume, due to the low contact angle of water, making the condensation almost film wise, where film wise condensation insulates the substrate from the atmosphere and reduces the surface area available for new condensation. Although, practical limitations of the experimental set up prevented analysis of the condensation rates on the macro pattern, observations of water condensing on the surface revealed droplet coalescence with a preferred direction

towards the hydrophilic bumps, increasing the available surrounding surface area for new water droplets to nucleate and leading to enhanced droplet growth on the bumps.

The water collection performance of the three patterned surface coatings and a plain PS surface coating was simultaneously compared in a condensation chamber where ambient humidity and surface subcooling were controlled. At low surface subcooling, $\Delta T = 3$ °C, and 95 %RH, the macro patterned surface resulted in a water collection rate of 14.5 mL m^{-2} h^{-1}, the highest of the four surfaces tested, with the PS coating collecting the least amount of water over the duration of the experiment. However, at $\Delta T = 5$ °C, the PS coating outperformed all the patterned coatings, collecting 38.1 mL m^{-2} h^{-1} and at $\Delta T = 10$ °C the water collection rate of all of the surfaces increased significantly, however it was not possible to identify a significant difference in the water collection performance between the four surface coatings.

The results of this study are in agreeance with the experiments in the field of condensation heat exchange which find that dropwise condensation, experienced on a hydrophobic substrate, leads to higher condensation and heat transfer rates due to the smaller value of $V_{crit.}$ for droplet sliding off the surface, than experienced during film wise condensation on hydrophilic substrates.[27] As expected, the experiments presented in this Chapter demonstrate that, although water condensation is slower at low values of ΔT and relative humidity on all surfaces, the effect is particularly strong on purely hydrophobic surfaces due to the lower droplet nucleation rate, which is also described theoretically by Equation 1.5.[23, 28] Under these conditions, a chemically and topographically patterned surface coating with hydrophilic bumps at least 80 μm in diameter, 9 μm in height and with bump separation on the millimetre scale is shown to have the highest water collection efficiency. It is suggested that patterned surfaces, manufactured by polymer film dewetting, could be tailored to selectively adsorb and collect a variety of solvents from the vapour phase at atmospheric temperature and pressure and with low energy demands for surface cooling.

Finally, the robustness of the patterned surface coatings was analysed after extended periods of water collection. The macro and micro patterned surfaces coatings appeared to mechanically degrade and the chemical contrast between the hydrophobic background and hydrophilic bumps decreased. This degradation was attributed to the swelling of the P4VP bumps by water on the surface leading to disintegration of the bumps and leaching of the P4VP onto the hydrophobic regions.

The combination of P4VP and PS has been used to prove the concept of water collection on patterned surfaces, however the degradation of the P4VP bumps suggests that an alternative hydrophilic material be used or a treatment method, such as cross linking, be developed to stabilise the bumps on the hydrophobic background. There remain extensive opportunities to optimise the wettability contrast, pattern geometry and understand the fundamental role of surface topography and chemistry on the water condensation and collection process, however the concept of water collection by chemically and topographically patterned surface, prepared by a simple, low cost and reliable solvent annealing method, has been proven successful.

6.6   References

1.   World Economic Forum. *Global Risks 2015*: Geneva, Switzerland 2015.

2.   Mekonnen, M. M.; Hoekstra, A. Y. Four billion people facing severe water scarcity. *Sci. Adv.* **2016,** *2* (2), e1500323.

3.   Beysens, D.; Milimouk, I. The case for alternative fresh water sources. *Pour les resources alternatives en eau, Secheresse* **2000,** *11* (4), 1-16.

4.   Malik, F. T.; Clement, R. M.; Gethin, D. T.; Krawszik, W.; Parker, A. R. Nature's moisture harvesters: a comparative review. *Bioinspir. Biomim.* **2014,** *9* (3), 031002.

5.   Nørgaard, T.; Dacke, M. Fog-basking behaviour and water collection efficiency in Namib Desert Darkling beetles. *Front. Zool.* **2010,** *7* (1), 1-8.

6.   Parker, A. R.; Lawrence, C. R. Water capture by a desert beetle. *Nature* **2001,** *414* (6859), 33-34.

7.   Quéré, D. Wetting and Roughness. *Annu. Rev. Mater. Res.* **2008,** *38* (1), 71-99.

8.   Zhai, L.; Berg, M. C.; Cebeci, F. C.; Kim, Y.; Milwid, J. M.; Rubner, M. F.; Cohen, R. E. Patterned superhydrophobic surfaces: toward a synthetic mimic of the Namib Desert beetle. *Nano Lett.* **2006,** *6* (6), 1213-1217.

9.   Garrod, R.; Harris, L.; Schofield, W.; McGettrick, J.; Ward, L.; Teare, D.; Badyal, J. Mimicking a stenocara beetle's back for microcondensation using plasmachemical patterned superhydrophobic-superhydrophilic surfaces. *Langmuir* **2007,** *23* (2), 689-693.

10.   Hou, Y.; Yu, M.; Chen, X.; Wang, Z.; Yao, S. Recurrent Filmwise and Dropwise Condensation on a Beetle Mimetic Surface. *ACS Nano* **2014,** *9* (1), 71-81.

11.   Lee, S.; Lee, J.; Park, C.; Lee, C.; Kim, K.; Tahk, D.; Kwak, M. Continuous fabrication of bio-inspired water collecting surface via roll-type photolithography. *Int. J. Precis. Eng. Man.* **2014,** *1* (2), 119-124.

12.   Zhang, L.; Wu, J.; Hedhili, M. N.; Yang, X.; Wang, P. Inkjet printing for direct micropatterning of a superhydrophobic surface: toward biomimetic fog harvesting surfaces. *J. Mater. Chem. A* **2015,** *3* (6), 2844-2852.

13.   Dorrer, C.; Rühe, J. Mimicking the Stenocara Beetle - Dewetting of Drops from a Patterned Superhydrophobic Surface. *Langmuir* **2008,** *24* (12), 6154-6158.

14.   Lee, A.; Moon, M. W.; Lim, H.; Kim, W. D.; Kim, H. Y. Water harvest via dewing. *Langmuir* **2012,** *28* (27), 10183-10191.

15.   Park, K. C.; Kim, P.; Grinthal, A.; He, N.; Fox, D.; Weaver, J. C.; Aizenberg, J. Condensation on slippery asymmetric bumps. *Nature* **2016,** *531* (7592), 78-82.

16.   Thickett, S. C.; Neto, C.; Harris, A. T. Biomimetic surface coatings for atmospheric water capture prepared by dewetting of polymer films. *Adv. Mater.* **2011,** *23* (32), 3718-3722.

17.   Kang, H.; Lee, S. H.; Kim, S.; Char, K. Dewetting and Layer Inversion of Inverted PVP/PS Bilayer Films. *Macromolecules* **2003,** *36* (23), 8579-8583.

18.   Thickett, S. C.; Harris, A.; Neto, C. Interplay between Dewetting and Layer Inversion in Poly (4-vinylpyridine)/Polystyrene Bilayers. *Langmuir* **2010,** *26* (20), 15989-15999.

19.   Yoon, B. K.; Huh, J.; Kim, H. C.; Hong, J. M.; Park, C. Ordered patterns of microimprinted bilayer polymer films with controlled dewetting and layer inversion. *Macromolecules* **2006,** *39* (3), 901-903.

20.   Cassie, A. B. D.; Baxter, S. Wettability of porous surfaces. *J. Chem. Soc., Faraday Trans.* **1944,** *40* (0), 546-551.

21.   McHale, G. Cassie and Wenzel: Were They Really So Wrong? *Langmuir* **2007,** *23* (15), 8200-8205.

22.   Furmidge, C. Studies at phase interfaces. I. The sliding of liquid drops on solid surfaces and a theory for spray retention. *J. Colloid Sci.* **1962,** *17* (4), 309-324.

23.   Beysens, D. The formation of dew. *Atmos. Res.* **1995,** *39* (1), 215-237.

24.   Bai, H.; Ju, J.; Sun, R.; Chen, Y.; Zheng, Y.; Jiang, L. Controlled Fabrication and Water Collection Ability of Bioinspired Artificial Spider Silks. *Adv. Mater.* **2011,** *23* (32), 3708-3711.

25.   Zheng, Y.; Bai, H.; Huang, Z.; Tian, X.; Nie, F. Q.; Zhao, Y.; Zhai, J.; Jiang, L. Directional water collection on wetted spider silk. *Nature* **2010,** *463* (7281), 640-643.

26.   Ju, J.; Zheng, Y.; Jiang, L. Bioinspired one-dimensional materials for directional liquid transport. *Acc. Chem. Res.* **2014,** *47* (8), 2342-2352.

27.   Leach, R. N.; Stevens, F.; Langford, S. C.; Dickinson, J. T. Dropwise Condensation: Experiments and Simulations of Nucleation and Growth of Water Drops in a Cooling System. *Langmuir* **2006,** *22* (21), 8864-8872.

28.   Sigsbee, R. Vapor to condensed-phase heterogeneous nucleation. *Nucleation. Zettlemoyer AC. New York, Marcel Dekker* **1969**, 151-224.

CHAPTER 7

Conclusions and Outlook

7.1   Conclusions and Outlook

This Thesis describes a novel strategy to prepare patterned surface coatings, with controlled surface architecture and chemistry, by dewetting polymer films from a solid or 'soft' polymer substrate. The solvent annealing method presented provides a simple, inexpensive and scalable route towards the production of patterned coatings on both flat and three-dimensional substrates. The ability to control the rate of dewetting and the surface architecture provides a significant step towards the adoption of polymer film dewetting as a mainstream material fabrication process, which is demonstrated by the use of patterned surface coatings on copper tubes, prepared by dip coating and subsequent solvent vapour annealing, for atmospheric water harvesting.

Chapter 3 describes the design and development, construction and characterisation of a purpose-built apparatus for water harvesting measurements. The design is composed of a central condensation chamber which is controlled for temperature and humidity. Within the chamber, four parallel polymer coated copper tubes are internally cooled below the ambient environment (subcooled) by a flow of ethanol from a temperature-controlled circulating refrigerator. The apparatus is designed to allow direct observation and the simultaneous comparison of the water collection performance of four surface coatings within the same ambient environment. The apparatus may also be used for measurement and calculation of the heat transfer coefficient of these coatings, but heat transfer experiments were beyond the scope of this Thesis. This Chapter also contains information on the setup and issues related to the safe operation of the apparatus. Coating and dewetting of the polymer films on the copper tubes to produce patterned surface coatings and the discussion on the experimental work utilising this apparatus is the subject of Chapter 6.

Chapter 4 describes a novel solvent vapour annealing technique where PS films, coated on a SiO/Si substrate, were exposed to a saturated vapour environment of a mixture of toluene and ethanol, a good and a poor solvent for PS, respectively. Systematically increasing the concentration of ethanol in the mixture revealed a drastic increase in the rate of hole growth in the PS film as well as a change in morphology of the holes. Optical microscopy was used to follow the *in situ* growth

of the holes in the PS film, from which the hole growth rate, rim width, droplet diameter and droplet distribution were extrapolated. Furthermore, the receding contact angle of the rims surrounding the holes in the PS film and the equilibrium contact angle of the PS droplets at the conclusion of dewetting were measured from cross sectional profiles obtained by atomic force microscopy. The main conclusion of this work was that annealing PS films in a vapour mixture of a good and poor solvent resulted in much stronger elastic recoiling forces, a driving force for film dewetting, than when the films were thermally annealed or annealed in pure toluene, a good solvent for PS.

Morphologically, the rims surrounding the holes became unstable on the addition of more than 1% wt. ethanol to the annealing environment, leading to undulations in the transverse direction which resulted in extensive fingering and radial droplet shedding within the holes. The onset of droplet shedding coincided with a transition from an increasing dewetting rate regime to a second regime characterized by linear hole growth at the maximum dewetting rate. Due to this trend, the droplet shedding mechanism has been considered to lead to the 'auto-optimisation' of film dewetting. It is suggested that future morphological studies may utilise high-resolution measurement techniques, such as confocal microscopy on dewetting films doped with fluorescent molecular probes, to study the flow behavior of the polymer in the rim region surrounding the growing holes as well as the bulk film.

Adding up to 15% wt. ethanol to the toluene saturated vapor environment increased the rate of PS film dewetting by up to two orders of magnitude compared to annealing in a pure toluene environment. Furthermore, the contact angle of isolated PS droplets and the receding contact angle of the rims on the silicon substrate increased approximately by a factor of 6 over the films annealed in pure toluene. These observations were attributed to the reorganization of the polymer chains within the PS film, which was plasticized due to the presence of toluene, and to enhanced slip at the PS-substrate interface due to polar interactions between ethanol and the hydroxide groups on the silicon oxide substrate.

Due to the mixed solvent vapour environment surrounding the PS film, an 'onion-like' structure of solvent layering exists around the polymer chains: an inner core of the preferentially adsorbed toluene molecules, which swell the PS chains, surrounded by an outer shell of ethanol which drives chain compaction towards a

globule conformation. This conformational change of the polymer chains, theoretically predicted by Shultz and Flory and demonstrated by Monte-Carlo simulations in work by Magda *et al.* for infinitely dilute polymer solutions has been demonstrated in polymer melts in this Thesis, whereby it enhances the elastic driving forces for film dewetting. Rapid film dewetting occurs when this enhanced driving force is coupled with lower film viscosity, due to the compact conformation of the polymer chains, and slip at the interface, as a result of the polar interactions between the ethanol and the silicon oxide substrate. The specific effects, on film dewetting, of slip at the interface and lower film viscosity due to chain compaction and disentanglement, could not be separated by the experiments conducted in this Thesis. However, it may be possible to separately identify these effects through rheology or crazing experiments[1] in the presence of solvent vapours. The enhanced driving forces for film dewetting by exposing a polymer film to a solvent vapour mixture environment was further demonstrated in this Chapter in two ways: firstly by dewetting PS films up to 520 nm in thickness by annealing in toluene-ethanol saturated vapour environments (Figure 7.1(a)), and secondly by completely dewetting PS films which had been aged at the T_g of PS (105 °C) for 72 h prior to exposing to the saturated solvent vapour mixture.
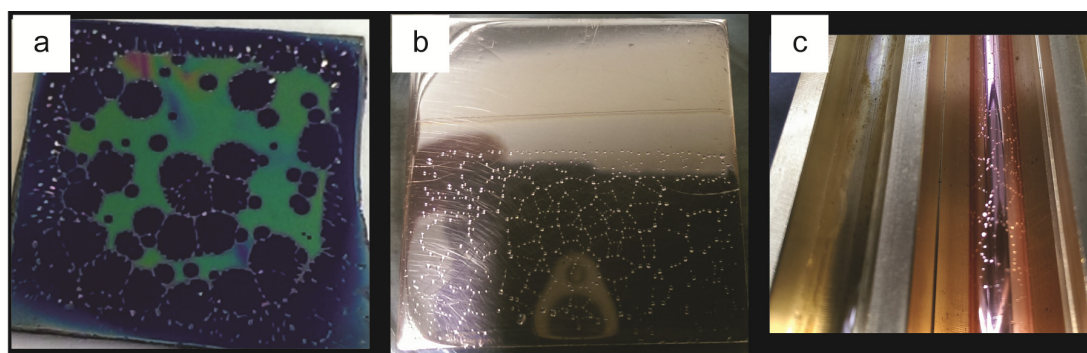

Figure 7.1: Photographs of dewetting P4VP/PS bilayers, showing hexagonal networks of isolated P4VP bumps on PS coated substrates. (a) Silicon wafer (10 x 10 mm^2), (b) copper sheet (40 x 40 mm^2) and (c) a copper tube, 10 mm in diameter.

The findings presented here are fundamentally significant, as the ability to control the rate of a dewetting experiment, as well the aspect ratio of the droplets and the behavior of the rims surrounding dewetted holes simply by tuning the composition of a solvent mixture composition opens up avenues for the observation

and understanding of the underlying molecular scale interactions that result in this phenomenon.   Practically, this annealing technique provides the researcher the freedom to dewet polymer systems that are stable on the substrate when thermally annealing, simply by the choice of an appropriate solvent mixture.

The solvent vapour annealing technique developed for dewetting PS from an underlying silicon substrate was extended to dewet P4VP/PS bilayer films to produce chemically and topographically patterned polymeric surface coatings. The use of binary and ternary solvent vapour mixtures of ethanol, acetone and water as vapour annealing environments for the bilayer films, leading to P4VP dewetting from the underlying PS film, was discussed in Chapter 5.   In this Chapter, the role of each solvent leading to P4VP film dewetting was deduced: ethanol, a good solvent for P4VP, swelled and plasticized the film, acetone and water, poor solvents for P4VP, enhanced the elastic stresses in the polymer chains due to the collapse of the polymer chains. The enhanced dewetting rate observed during annealing in mixtures containing acetone could also, in part, be attributed to interfacial slip due to the affinity of acetone to the PS substrate.

Thermally annealing P4VP/PS bilayer films in order to induce selective dewetting of the P4VP layer has previously been shown to lead to layer inversion. Another phenomenon, termed 'co-dewetting', whereby both layers in a bilayer film dewetted from their respective substrates was described in Chapter 5. For the practical purposes of this Thesis, both of these phenomena were undesirable as they affected the wettability contrast provided by the patterned surfaces produced by dewetting a hydrophilic P4VP film from an underlying hydrophobic PS film. The onset of these phenomena was attributed to the swelling and plasticization of the PS layer during thermal annealing or while solvent annealing in the presence of a good solvent for PS. It was demonstrated in this Chapter, that the choice of solvents not only enhanced the dewetting rate of the P4VP film but also mitigated the onset of layer inversion and co-dewetting by maintaining the PS film as a solid substrate.

Finally, to demonstrate the flexibility of the developed solvent vapour annealing technique and the ability to produce unique and complex surface architectures by polymer film dewetting, a PTFE/PS bilayer film was dewetted by annealing in an appropriate choice of solvents. The behavior of water condensing on the surface patterned with PTFE bumps on PS illustrated the wettability contrast between these two hydrophobic polymers. Furthermore, the non-wetting nature of

PTFE was utilized to spin coat P4VP from ethanol on a partially dewetted PTFE/PS bilayer (holes within the PTFE film revealing the underlying PS film). The outcome was a surface with extreme wettability contrast between the PTFE matrix and the P4VP cast within the holes. Finally, the P4VP film was solvent vapour annealed in an acetone-water mixture and dewetted, firstly from the PTFE matrix surrounding the hole and then from the underlying PS film to produce P4VP droplets within the PS 'wells' in the PTFE matrix.

Chapter 6 describes the practical application of the novel solvent vapour annealing technique described in the previous two Chapters to dewetting P4VP/PS bilayer films on two and three dimensional copper substrates (Figure 7.1(b) and (c)). By dewetting P4VP films ranging in thickness from a few nanometers up to hundreds of microns, P4VP bumps with a range of diameters over 2 orders of magnitude were prepared on the underlying PS film as cast on the copper substrates. The contrast in surface wettability presented by the hydrophilic bumps on the hydrophobic background was qualitatively demonstrated by observing the condensation of water vapour on the subcooled coated substrates within a controlled humidity environment. The observations from this study revealed the strong dependency of water condensation rate on the surface wettability at low levels of subcooling below ambient temperatures, with the condensation rate, in terms of wetted surface area, becoming independent of surface wettability at high levels of substrate subcooling, i.e. water droplets nucleated and grew at similar rates on both the hydrophobic polystyrene coatings and coatings with a surface area containing hydrophilic P4VP domains as well as completely hydrophilic P4VP coatings.

Water collection studies were carried out using the purpose built apparatus described in Chapter 3. The water harvesting performances of nano, micro and macro scale patterned coatings was directly compared against a flat PS coating at 95 %RH and subcooling temperatures varying between 3 – 10 °C. At low subcooling (3 °C), the macro patterned surface collected the most water (87 mL m^{-2}) over a period of 6 h, with the hydrophobic PS coating collecting the least. As the subcooling was increased to 5 °C and then 10 °C; the water collection of all of the surfaces increased, however the PS coating collected the most water in both instances as predicted from the condensation observations. These results illustrated that the concept of biomimetic water harvesting, inspired by the adaptations of the Namib Desert beetle, is particularly useful for the passive, condensation and collection of water vapour.

A parametric study of the relative importance of surface wettability and topography as well as the effects of bump spacing, size and aspect ratio are proposed as further work in this field. The preparation techniques for polymeric surfaces that could be used for these studies were presented but due to time constraints the experiments were not conducted. While the benefits of utilizing patterned surfaces for water collection have been demonstrated, and polymer film dewetting has been shown to be an efficient and cost effective route towards manufacturing these surfaces, there exist some drawbacks to this technology. Firstly, polymer films are delicate and may be susceptible to delaminating from the underlying substrate when exposed to solvents, ultra-violet radiation and mechanical abrasion. The deterioration of the P4VP bumps on the patterned surfaces following extended periods of water collection was discussed in Chapter 6. Polymeric coatings may be made more robust by using alternative preparation techniques such as chemical vapour deposition[2] where the polymer may graft directly onto the substrate or form insoluble crosslinked networks. Alternative polymer systems, which are more durable to UV and solvent exposure, can be identified and finally, the mechanical strength of the coatings may be increased by utilizing nanoparticle – polymer composite films. Improving the mechanical durability of the surfaces would also allow for the removal of biofilms and other contaminants that are expected to form on the surfaces during water collection.

In this Thesis, a novel, simple, scalable and inexpensive method to produce patterned polymeric surface coatings by polymer film dewetting, with patterns produced on the nano to the macro scales, has been presented. A mechanism is proposed, which describes the dependence of dynamics and hole and rim morphology of a dewetting polymer film annealed in a saturated solvent vapour mixture, on the solubility of the polymer in each solvent. The ability to simply tune the vapour environment surrounding a polymer system to induce and control dewetting from solid and 'soft' substrates allows the researcher to produce patterned surfaces displaying a range of complex physical and chemical architectures, from a variety of polymers. This simple, cost effective and scalable technique provides a step towards the use of polymer film dewetting to produce patterned surface coatings for technological and industrial application. By comparison; commonly used etching techniques which provide superior control over the location and geometry of chemical heterogeneities on a surface, are limited to lab-scale research due to the

prohibitive costs of scaling up the technology. Similarly, printing techniques which offer a viable alternative pathway towards the large scale production of patterned polymer materials are currently limited to producing two-dimensional architectures at the micro scale. It is suggested that in the future, a hybrid process combining printing with the solvent vapour annealing technique presented in this Thesis may be the solution to producing patterned polymeric materials with control over the pattern distribution and geometry.

7.2   References

1.   McGraw, J. D.; Fowler, P. D.; Ferrari, M. L.; Dalnoki-Veress, K. Relaxation of non-equilibrium entanglement networks in thin polymer films. *Eur. Phys. J. E* **2013,** *36* (1), 1-8.
2.   Alf, M. E.; Asatekin, A.; Barr, M. C.; Baxamusa, S. H.; Chelawat, H.; Ozaydin - Ince, G.; Petruczok, C. D.; Sreenivasan, R.; Tenhaeff, W. E.; Trujillo, N. J. Chemical vapor deposition of conformal, functional, and responsive polymer films. *Adv. Mater.* **2010,** *22* (18), 1993-2027.

Appendix A

Solvent mixture vapour fractions

Assuming that the solvent mixtures were an ideal solution, the partial pressure ($x_i p_i$) of each solvent component in the vapour phase could be deduced from Raoult's Law:

$$P_{total} = x_{toluene} p_{toluene} + x_{ethanol} p_{ethanol}$$

where P_{total} is the total pressure of the solvents, x_i is the mole fraction of each component in the liquid mixture and p_i is the saturation pressure of each component at the experimental temperature. Table 1 provides the calculated partial pressure and vapour phase mole fractions for the mixtures used in the experiments discussed in Chapter 4, using both Raoult's law and experimental data from the literature.[1] The weight composition of the toluene-ethanol solvent mixtures in the liquid phase is referred to in Chapter 4.

Table 1: Calculation of vapour phase mole fraction derived from the mass fraction of each component in the liquid phase using Raoult's Law and saturated vapour pressure of toluene and ethanol at 25°C, and literature data for 35°C.[1]

Toluene weight fraction in the liquid	Toluene mole fraction (ethanol balance)		
	Liquid	Vapour - from Raoult's law	Vapour mole fraction from ref. [1]
0.3	0.18	0.09	0.23
0.4	0.25	0.14	0.27
0.6	0.43	0.27	0.33
0.8	0.67	0.49	0.37
0.85	0.74	0.58	0.39
0.9	0.82	0.69	0.40
0.95	0.9	0.82	0.46
0.99	0.98	0.96	0.74
1	1	1	1

The plot of mole fraction of each solvent in the vapour phase in binary solvent mixtures of ethanol, acetone and water is provided in Figure 2 and is used in Chapter 5 when discussing these mixtures. Furthermore, tabulated data for the mole fraction

of each solvent in the ternary mixture composed of these three solvents is provided in
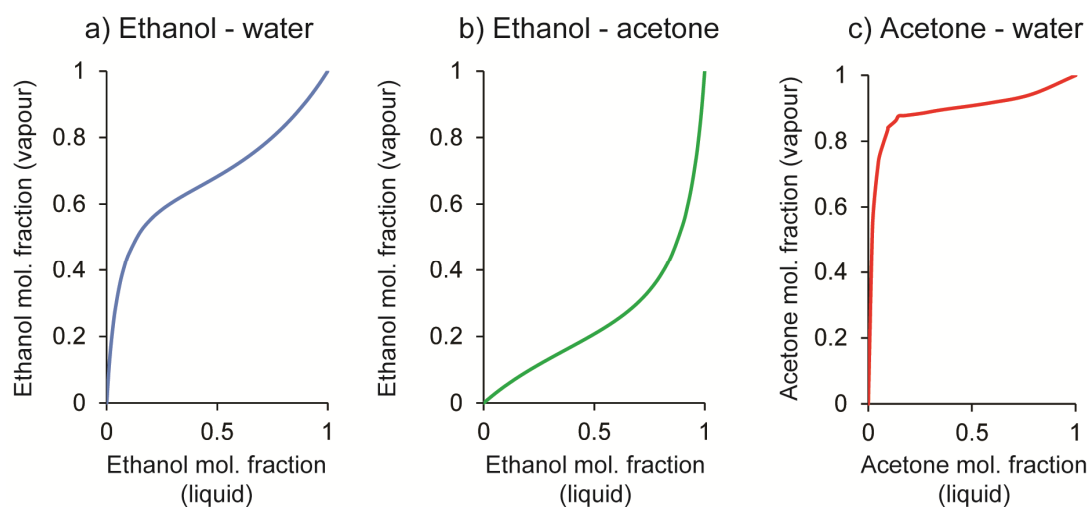Table 2.

Figure 1: Mole fractions of the liquid and vapour phases for binary mixtures at 25 °C[2-4] of (a) ethanol
- water (b) ethanol – acetone, and (c) acetone - water.

Table 2: Conversion between composition in the liquid phase to vapor phase for a ternary mixture of
ethanol - acetone - water at 25°C calculated by the UNIFAC method.[4-5]

Liquid phase (water mass fraction)[a]	Liquid phase (mole fraction)			Vapour phase (mole fraction)		
	Acetone	Ethanol	Water	Acetone	Ethanol	Water
0.0	0.44	0.56	0	0.77	0.23	0
0.1	0.34	0.42	0.24	0.74	0.18	0.08
0.2	0.26	0.33	0.42	0.68	0.19	0.13
0.3	0.20	0.25	0.55	0.68	0.16	0.16
0.4	0.15	0.19	0.66	0.66	0.16	0.18
0.5	0.11	0.14	0.74	0.62	0.16	0.22
0.6	0.08	0.11	0.81	0.68	0.12	0.2
0.7	0.06	0.07	0.87	0.54	0.19	0.27
0.8	0.04	0.04	0.92	0.63	0.1	0.27
0.9	0.02	0.02	0.96	0	0	1

[a] Mass fraction of water added to a 1:1 (w/w) liquid mixture of ethanol and acetone. A 1:1

(w/w) ethanol-acetone mixture without water corresponds to the first row of data in the table.

References

1.   Kretschmer, C. B.; Wiebe, R. Liquid-Vapor Equilibrium of Ethanol--Toluene Solutions. *J. Am. Chem. Soc.* **1949,** *71* (5), 1793-1797.
2.   Flick, E. W. *Industrial solvents handbook*; Noyes Publications, 1985.
3.   Chemical Engineering and Materials Research Information Center. Binary Vapor-Liquid Equilibrium Data. 2016.
4.   Beare, W.; McVicar, G.; Ferguson, J. The determination of vapor and liquid compositions in binary systems. *The Journal of Physical Chemistry* **1930,** *34* (6), 1310-1318.
5.   D'Avila, S.; Cotrim, M. Prediction of isothermal vapour liquid equilibrium data of nonideal ternary mixtures from binary data system. Acetone-ethanol-water. *Revista Brasileira de Tecnologia* **1973,** *4*, 191-197.

Appendix B

Hansen and Hildebrand solubility parameters

Hansen identified the individual contributions of the dispersion δ_D, polar δ_P and hydrogen-bond δ_H energy towards the cohesive energy density described by the Hildebrand solubility parameter, δ:[1]

$$\delta^2 = \delta_D^2 + \delta_P^2 + \delta_H^2 \tag{1}$$

As an example, in the case of ethanol the Hansen solubility parameters are $\delta_D = 15.8$ MPa$^{1/2}$, $\delta_P = 8.8$ MPa$^{1/2}$ and $\delta_H = 19.4$ MPa$^{1/2}$, the Hildebrand solubility parameter can be calculated from

$$\delta_{etOh} = \sqrt{\delta_D^2 + \delta_P^2 + \delta_H^2} \approx 26.5 \text{ MPa}^{1/2} \tag{2}$$

The Flory-Huggins interaction parameter can be calculated from the Hildebrand solubility parameters of the polymer and the solvent, and provides a qualitative estimation of polymer solubility.

$$\chi_{Polymer-Solvent} = \frac{V_{seg}(\delta_{Polymer} - \delta_{Solvent})^2}{RT} \tag{3}$$

Where V_{seg} is the volume of the polymer segment, R is the gas constant and T, the temperature. The more similar the value of the cohesive energy difference of the polymer and the solvent, the higher the quality of the solvent for the polymer.

Where Hansen solubility data is available, it is recommended to use the relative energy difference

Empirical data for PS and P4VP surface tension

A model was developed by Sauer and Dee to convert pressure – volume – temperature (PVT) data for polymers into the cohesive energy density (CED) from which it is possible to calculate the surface tension.

Table 1: Cohesive energy density (CED) data and surface tension information used for spreading parameter, interaction parameter and surface tension calculations obtained from experimental work by Sauer and Dee. [2]

Polymer	CED (temp) (MPa (°C))	Polynomial Fits of Surface Tension Data		
		A_0 (mN m^{-1})^a	Slope (mN m^{-1} °C^{-1})	Temp range (°C)
PS	230 (200)	41.5	-0.065	130 - 220
P4VP	600 (250)	74.1	-0.128	250-260

$^a\gamma = A_0$ + slope x T, where temperature is in °C.

References

1.   Hansen, C. M. *Hansen solubility parameters: a user's handbook*; CRC press, 2007.
2.   Sauer, B. B.; Dee, G. T. Surface tension and melt cohesive energy density of polymer melts including high melting and high glass transition polymers. *Macromolecules* 2002, *35* (18), 7024-7030.